

Springer Theses

Recognizing Outstanding Ph.D. Research

Vivien Yeh

Study of Bacteriorhodopsin in a Controlled Lipid Environment

 Springer

Springer Theses

Recognizing Outstanding Ph.D. Research

Aims and Scope

The series “Springer Theses” brings together a selection of the very best Ph.D. theses from around the world and across the physical sciences. Nominated and endorsed by two recognized specialists, each published volume has been selected for its scientific excellence and the high impact of its contents for the pertinent field of research. For greater accessibility to non-specialists, the published versions include an extended introduction, as well as a foreword by the student’s supervisor explaining the special relevance of the work for the field. As a whole, the series will provide a valuable resource both for newcomers to the research fields described, and for other scientists seeking detailed background information on special questions. Finally, it provides an accredited documentation of the valuable contributions made by today’s younger generation of scientists.

Theses are accepted into the series by invited nomination only and must fulfill all of the following criteria

- They must be written in good English.
- The topic should fall within the confines of Chemistry, Physics, Earth Sciences, Engineering and related interdisciplinary fields such as Materials, Nanoscience, Chemical Engineering, Complex Systems and Biophysics.
- The work reported in the thesis must represent a significant scientific advance.
- If the thesis includes previously published material, permission to reproduce this must be gained from the respective copyright holder.
- They must have been examined and passed during the 12 months prior to nomination.
- Each thesis should include a foreword by the supervisor outlining the significance of its content.
- The theses should have a clearly defined structure including an introduction accessible to scientists not expert in that particular field.

More information about this series at <http://www.springer.com/series/8790>

Vivien Yeh

Study of Bacteriorhodopsin in a Controlled Lipid Environment

Doctoral Thesis accepted by
National Taiwan University, Taipei, Taiwan

Author

Dr. Vivien Yeh
Department of Chemistry
National Taiwan University
Taipei, Taiwan

Supervisors

Prof. Jerry C. C. Chan
Department of Chemistry
National Taiwan University
Taipei, Taiwan

Dr. Tsyr-Yan Yu
Institute of Atomic and Molecular Sciences
Academia Sinica
Taipei, Taiwan

ISSN 2190-5053

Springer Theses

ISBN 978-981-13-1237-3

<https://doi.org/10.1007/978-981-13-1238-0>

ISSN 2190-5061 (electronic)

ISBN 978-981-13-1238-0 (eBook)

Library of Congress Control Number: 2018945869

© Springer Nature Singapore Pte Ltd. 2019

This work is subject to copyright. All rights are reserved by the Publisher, whether the whole or part of the material is concerned, specifically the rights of translation, reprinting, reuse of illustrations, recitation, broadcasting, reproduction on microfilms or in any other physical way, and transmission or information storage and retrieval, electronic adaptation, computer software, or by similar or dissimilar methodology now known or hereafter developed.

The use of general descriptive names, registered names, trademarks, service marks, etc. in this publication does not imply, even in the absence of a specific statement, that such names are exempt from the relevant protective laws and regulations and therefore free for general use.

The publisher, the authors and the editors are safe to assume that the advice and information in this book are believed to be true and accurate at the date of publication. Neither the publisher nor the authors or the editors give a warranty, express or implied, with respect to the material contained herein or for any errors or omissions that may have been made. The publisher remains neutral with regard to jurisdictional claims in published maps and institutional affiliations.

Printed on acid-free paper

This Springer imprint is published by the registered company Springer Nature Singapore Pte Ltd. The registered company address is: 152 Beach Road, #21-01/04 Gateway East, Singapore 189721, Singapore

Supervisor's Foreword

Due to its hydrophobicity and difficult sample preparation, the study of membrane protein has been a challenge. The recent development of a membrane mimic, lipid nanodisc, can provide the membrane protein a lipid bilayer environment, aiding the structural and functional studies of many membrane proteins *in vitro*. The advantages of nanodisc not only provide a near-native membrane environment that is suitable for biophysical studies, but also offer a well-controlled lipid bilayer system with size homogeneity. This work utilizes this property of nanodisc to perform systematic studies of the effect of lipid composition and of the size of nanodisc on the function of an integral membrane protein, bacteriorhodopsin, by monitoring the photocycle kinetics of the proton-pumping protein.

The effect of lipid composition of nanodisc was investigated by assembling nanodisc composed of different ratios of zwitterionic and negatively charged lipid molecules, where the surface charge was qualitatively analysed using ionic exchange chromatography. Photocycle kinetics was investigated using transient absorption spectroscopy monitoring at different wavelengths corresponding to the absorption wavelength of different intermediate states. It was demonstrated that the charge of the lipid hydrophilic head could significantly alter the photocycle kinetics, including the photocycle recovery time, intermediate lifetime, and photocycle pathway. The phenomenon was further studied using transient photocurrent measurement, where the result suggested that lipid plays a role in the translocation of proton by the protein during the photocycle.

The size of the nanodisc is monitored by the size of the membrane scaffold protein, which would wrap around the disc-shaped lipid layer core of the lipid nanodisc. By adjusting the length of the membrane scaffold protein, one can alter the size of the assembled nanodisc. *E. coli*-expressed bacteriorhodopsin was used to study the effect of size. It was found that the size of the nanodisc is not a major influencing factor on the photocycle of the *E. coli*-expressed bacteriorhodopsin in comparison with the lipid composition.

The last part of this thesis included a highly efficient method to extract bacteriorhodopsin from the native purple membrane of *Halobacterium salinarum*, and directly assemble into nanodisc, preserving the essential native lipid molecules and

protein quaternary structure. The method employs modified membrane protein with covalently linked C and N termini and was systematically optimized to obtain up to 38% of transfer efficiency from the native purple membrane to the native membrane nanodisc. The conformation of bacteriorhodopsin was verified using visible-wavelength circular dichroism, and the nanodisc formation was studied using high-resolution Zernike phase TEM without staining. The lipid composition was investigated using LC-ESI-MS and ^{31}P NMR, that the majority of the essential phospholipid was successfully transferred. Lastly, we demonstrated the function preservation of bacteriorhodopsin using transient absorption spectroscopy, observing proton-pumping intermediate state, M, and retinal relaxation intermediate state, O. This efficient method of direct extraction of membrane protein would provide new platform to study membrane protein in a native-like environment while allowing biophysical characterization, which could show a higher biological relevance and improved sample preparation.

Taipei, Taiwan
April 2018

Dr. Tsyr-Yan Yu

Abstract

The structure and function of membrane protein often show dependency to the membrane environment. Monodisperse lipid nanodisc has been a useful tool for mimicking membrane environment for the biophysical characterization of membrane proteins. Nanodisc is a high-density lipoprotein with a disc-shaped core of lipid molecules, wrapped by two copies of membrane scaffold protein, providing membrane protein a near-native lipid bilayer environment while suitable for spectroscopic studies. By incorporating monomeric bacteriorhodopsin (bR) into nanodisc, we demonstrate how to manually manipulate the function of membrane protein by altering the property of the nanodisc, such as lipid composition and the size of nanodisc. Embedding in nanodisc composed of different ratios of synthetic zwitterionic lipid to negatively charged lipid, the photocycle kinetics of bacteriorhodopsin was found to alter as the lipid composition changed. Full-wavelength transient absorption spectroscopy revealed that as the content of PG decreased, the duration of the photocycle of bR increased drastically and the photocycle pathway was altered. Further measurement using transient photocurrent indicated that lipid molecule not only affects the photocycle kinetics but also plays a role in the release of proton from the protein to the bulk solution during proton translocation. To study the effect of the size of nanodisc, *E. coli*-expressed bR was incorporated into nanodisc of two different sizes. The photocycle kinetics of bR embedded in nanodisc was compared to bR in detergent micelle and was shown to have significant different photocycle kinetics. However, the sizes of nanodisc were found to exhibit no significant effect on the function of bR embedded.

While demonstrating how the synthetic membrane environment can influence the function of membrane protein, we further improved the native environment by using a novel one-step method to incorporate trimeric bR into lipid nanodisc prepared from the native purple membrane of *Halobacterium salinarum*, without adding any synthetic lipid or lipid extracts. The method was demonstrated to produce homogenous sample with sufficiently high yield suitable for biophysical studies. The trimeric conformation of bR was verified using visible-wavelength circular dichroism, and Zernike phase TEM image showed a circular disc-like morphology. The lipid composition of the native purple membrane nanodisc was

investigated with ^{31}P NMR and liquid chromatography–mass spectrometry, where the essential lipids are shown to be maintained. Lastly, the preservation of photocycle activity was confirmed using transient absorption spectroscopy. We demonstrated the feasibility of transferring membrane protein into nanodisc directly from the native membrane, surrounded by native lipid molecules to preserve the biological structure.

Publications

The content of Chap. 3 was published in the following journal

Lee, T. Y.#; Yeh, V.#; Chuang, J.; Chan, J. C. C.; Chu, L. K.*; Yu, T. Y.* (2015) Tuning the Photocycle Kinetics of Bacteriorhodopsin in Lipid Nanodiscs, *Biophys. J.*, 109, 1899.

Yeh, V.#; Hsin, Y.#; Lee, T. Y.; Chan, J. C. C.; Yu, T. Y.*; Chu, L. K.* (2016) Lipids Influence the Proton Pump Activity of Photosynthetic Protein Embedded in Nanodiscs, *RSC Adv.*, 6, 88300.

The content of Chap. 5 was published in the following journal

Yeh, V.; Lee, T. Y.; Chen, C. W.; Kuo, P. C.; Shiue, J.; Chu, L.-K.*; Yu, T. Y. * (2018) Highly Efficient Transfer of 7TM Membrane Protein from Native Membrane to Covalently Circularized Nanodisc. *Sci. Rep.*, 8 (1), 13501.

#equal contribution

*corresponding author(s)

Acknowledgements

First and for most, I could not have achieved what I have without the brilliant guidance of my supervisors. I would like to take this opportunity to show my gratitude to Dr. Tysr Yan Yu, as without his support and teaching this thesis would simply not have been possible. Not only did he introduce me to the wonderful and vastly intriguing world of membrane proteins, but also mentored me to become a scientist that I am proud to be. Thank you for providing invaluable help throughout my struggles, as well as giving me the gifts of advice and counsel. I would also like to thank Prof. Jerry Chan, for offering me this Ph.D. position, as well as believing in me when I was lost. His passion in education and in research has taught me how to become a better scientist, while his patience and his kindness have motivated me to become a better person. Thank you so very much for guiding me to grow and mature, both as a scientist and as an adult.

Thanks to our amazing collaborators, Prof. L. K. Chu of NTHU, and his students, in particular Ian Lee, Yin Hsin and Yu-Min Kao, thank you for all of your wisdom, your effort and your hard work. To my laboratory members in IAMS: Tina Yusuf, Julien Massiot, Wayne Chang, Jocelyn Yen, Peter Chang, Gerard Liu, Julie Chang, Frans Ricardo and PeiHao Wu, thank you for being great colleagues and giving me a nice working experience. And to my laboratory members in NTU Chemistry: Dr. James Luo, Jenny Yang, Brook Tsai, Joyce Yu, Ben Wu, Khalil Du, Fred Yang, Judy Hou, Sol Chang, Ewan Cheng, Queena Chao, Ruby Chien, Joy Chang, Angel Huang, Eric Tsao, Lily Lin, Adward Guo and Joey Ho, thank you all for your friendship and thank you for enduring my odd cultural quirks. My time here in Taipei has been an unforgettable experience.

Finally, I would like to thank my parents who have given me support when I needed it most, and thank you for always providing me a home to go back to. To my brother who, despite living so far away, always managed to motivate me to keep moving forward. Lastly, I literally would not have been able to finish my degree

without the love, encouragement, understanding and forgiveness of James Nunn. Thank you for all the proof reading (including this one) and all the support you have given me. Thank you for not giving up when I almost did. I do not know what I have done to deserve you, but I sure am glad you stuck around.

Contents

1	Introduction	1
1.1	Membrane Protein	1
1.1.1	Membrane Protein Structures	3
1.1.2	Membrane Protein Characterization	6
1.2	Membrane Mimics	8
1.2.1	Detergent Micelle	8
1.2.2	Amphipols	12
1.2.3	Lipid Bicelle	13
1.2.4	Liposome	14
1.2.5	Styrene-Malic Acid Copolymers	14
1.3	Nanodisc	16
1.4	Bacteriorhodopsin	18
1.4.1	Halobacterium Salinarum	20
1.4.2	Haloarcula Marismortui	23
1.5	Motivation of Thesis	25
	References	27
2	Experimental Background	37
2.1	Chromatography Methods	37
2.1.1	Size Exclusion Chromatography	37
2.1.2	Ionic Exchange Chromatography	41
2.2	Circular Dichroism Spectroscopy	43
2.3	Transient Absorption Spectroscopy	45
2.3.1	Principles	45
2.3.2	Experimental Setup	46
2.4	Transient Photocurrent Measurement	48
2.4.1	Principles	48
2.4.2	Experimental Setup	49
2.5	Solution State NMR	50

2.6	Nanodisc Assembly and Optimization	54
2.6.1	MSP Expression and Purification	54
2.6.2	Circularization of cMSP	56
2.6.3	Lipid and MSP Optimization	57
2.7	PM Preparation	59
2.7.1	<i>H. salinarum</i> Culture	59
2.7.2	PM Isolation	59
2.8	HmbRI Preparation	61
2.8.1	Site Directed Mutagenesis	61
2.8.2	HmbRID94N Culture and Purification	61
2.8.3	Isotopic Labeling Expression	63
	References	64
3	Effect of Lipid Composition of Nanodisc	67
3.1	Introduction	67
3.2	Experimental Details	69
3.2.1	Sample Preparation	69
3.2.2	Sample Characterization	70
3.3	Results and Discussion	73
3.3.1	Sizes, Oligomeric State and Surface Charge	73
3.3.2	Steady State Absorption and CD Spectroscopy	76
3.3.3	Time Resolved Difference Spectra	80
3.3.4	Transient Photocurrent Measurements	86
3.4	Conclusion	88
	References	89
4	Effect of Size of Nanodisc	93
4.1	Introduction	93
4.2	Experimental Details	95
4.2.1	Sample Preparation	95
4.2.2	Sample Characterization	97
4.3	Results and Discussion	98
4.3.1	HmbRID94N Purification Using Triton X-100	98
4.3.2	HmbRID94N Characterization in Triton X-100	100
4.3.3	HmbRID94N in C7-DHPC	101
4.3.4	HmbRID94N in Nanodisc	104
4.4	Conclusion	110
	References	111
5	Native Membrane Nanodisc	113
5.1	Introduction	113
5.2	Experimental Details	115
5.2.1	Sample Preparation	115
5.2.2	Sample Characterization	116

5.3 Results and Discussion	117
5.3.1 PMND Assembly and Optimization	117
5.3.2 PMND Characterization	123
5.4 Conclusion	130
References	132
6 Conclusions and Outlook	135
Appendix: I—Preliminary Results of HsbR in DMPC Nanodisc of Different Sizes	139

Abbreviations

bR	Bacteriorhodopsin
BPG	Archaeal cardiolipin; sn-2,3-di-O-phytanyl-1-phosphoglycerol-3-phospho-sn-2,3-di-O-phytanylglycerol
C7-DHPC	1,2-Diheptanoyl-sn-glycero-3-phosphocholine
CD	Circular dichroism
c Δ H5	Circular MSP1D1 Δ H5 with joint C and N termini
cE3D1	Circular MSP1E3D1 with joint C and N termini
CHAPSO	3-([3-Cholamidopropyl]dimethylammonio)-2-hydroxy-1-propanesulphonate
cMSP	Membrane scaffold protein with chemically joint C and N termini
CMC	Critical micelle concentration
DDM	n-Dodecyl β -D-maltoside
DMPC	1,2-Dimyristoyl-sn-glycero-3-phosphocholine
DMPG	1,2-Dimyristoyl-sn-glycero-3-phospho-[1'-rac-glycerol]
DOPC	1,2-Dioleoyl-sn-glycero-3-phosphocholine
DOPG	1,2-Dioleoyl-sn-glycero-3-phospho-[1'-rac-glycerol]
DOTAP	1,2-Dioleoyl-3-trimethylammonium-propane
E3D1_srt	MSP1E3D1 with sortase A recognition site on the N terminal
EM	Electron microscopy
ESI	Electrospray ionization
GB1	Protein G B1 domain
GB1 Δ H5_srt	MSP1D1 Δ H5 with soluble protein GB1 fused on the N terminal and sortase A recognition site on the C terminal
GlyC	Archaeal glyco-cardiolipin; 3-HSO3-Galp- β 1,6Manp- α 1,2Glc- α 1,1- [sn-2,3-di-O-phytanylglycerol]-6- [phospho-sn-2,3-di-O- phytanylglycerol]
HmbRI	Bacteriorhodopsin I from <i>Haloarcula marismortui</i>
HmbRID94N	Mutated HmbRI with aspartic acid at position 94 substituted with asparagine

HmbRII	Bacteriorhodopsin II from <i>Haloarcula marismortui</i>
HsbR	Bacteriorhodopsin from <i>Halobacterium salinarum</i>
LC-MS	Lipid chromatography–mass spectrometry
m/z	Mass-to-charge ratio
MALDI	Matrix-assisted laser desorption/ionization
mbR	Monomeric bacteriorhodopsin
MSP	Membrane scaffold protein
MSP1D1	Membrane scaffold protein with ten helices
MSP1E3D1	MSP1D1 with three additional helices
MSP1D1 Δ H5	MSP1D1 with helix five removed
MW	Molecular weight
nbR	Nanodisc with bacteriorhodopsin incorporated
Ni-NTA	Nickel-coordinated nitrilotriacetic acid
NMR	Nuclear magnetic resonance
PG	Phosphatidylglycerol
PGP-Me	Phosphatidylglycerophosphate methyl ester
PGS	Phosphatidylglycerosulphate
PM	Purple membrane
PMND	Native purple membrane nanodisc
POPC	1-Palmitoyl-2-oleoyl-sn-glycero-3-phosphocholine
POPG	1-Palmitoyl-2-oleoyl-sn-glycero-3-phospho-[1'-rac-glycerol]
SDS	Sodium dodecyl sulphate
SDS-PAGE	Sodium dodecyl sulphate-polyacrylamide gel electrophoresis
SEC	Size exclusion chromatography
SMA	Styrene maleic acid copolymer
SMA _{nh}	Styrene maleic anhydride
SMALPs	Styrene maleic acid copolymer lipid particles
SQ	Squalene
S-TGD-1	Glycolipid; 3-HSO ₃ -Galp- β 1,6- Manp- α 1,2-Glcp- α 1,1-sn-2,3-diphytanylglycerol
TEM	Transmission electron microscopy
TX-100	Triton X-100

Chapter 1

Introduction



1.1 Membrane Protein

Biological membranes separate cells from the surrounding environment as well as enclosing compartments to maintain specific chemical or biochemical conditions. These membranes often consist of phospholipid bilayers and have certain distinctive tasks that are essential for fundamental biological functions. Membrane proteins are a category of protein found to interact or embed onto the biomembrane, which carry specific functions that govern the behaviour of the biomembrane [1]. Membrane proteins can have a variety of functions. Some play similar roles to soluble proteins, such as enzymes, carriers or parts of ensemble units. Others might be more unique to the properties of the membrane, for example, transporters and channels, which allow ions or small molecules to permeate the membrane barriers under selective conditions. Membrane proteins functioning as receptors are important during signal transduction pathways, triggering the biochemical chain of events and allowing the cell to interact with the surrounding environments and prompt the correct responses. Genomic sequence analysis estimates that as much as 30% of the protein expressed in *Homo sapiens*, *Escherichia coli* and *Saccharomyces cerevisiae* is integral membrane protein [2–6]. With their essential physiological roles and the fact membrane protein is located on the surface of the membrane, they are the target of almost 60% of medical drugs [7–9]. With such interest in the functional understanding and pharmaceutical application, experimentally solving the detailed three-dimensional structures of membrane proteins has become a focus in many research programs.

The first structure of membrane protein was revealed in 1975 [10]. A two dimensional crystal of purple membrane (PM) from *Halobacterium salinarum* containing bacteriorhodopsin (bR) was characterized by Henderson and Unwin using electron microscopy, and provided a three dimensional map at 7 Å resolution. Their results, shown in Fig. 1.1, showed seven cylindrical rods of density and they concluded that the rods were transmembrane α helices. Henderson was later awarded Nobel Prize in Chemistry 2017 for his contribution towards development

of cryo-electron microscopy for the high-resolution structure determination of biomolecules in solution. In 1985, Deisenhofer and Michel reported the atomic resolution structure of the photosynthetic reaction center from *Rhodospseudomonas viridis* [11], after being able to obtain better crystals by adjusting the detergents and micelle modulating additives [12]. Their research broadened the understanding of the mechanism of photosynthesis in bacteria, but more importantly their results suggested the possibilities of crystalizing membrane protein to allow atomic resolution X-ray crystallography. Together with Huber, the three shared the Nobel Prize in Chemistry 1988 for their achievements.

With further successes and breakthroughs, the progress of structural determination of membrane protein accelerated and the total number of unique structures of membrane protein solved increased exponentially every year, as shown in Fig. 1.2. The progression resembles the trend of soluble proteins, though with a small shift towards the lower numbers [13]. However, despite the progress in science and advances in technology, characterization of membrane protein remained a tremendous challenge mostly due to difficulties in sample preparation. Moreover, due to the nature of membrane protein functions in relation to its natural environments, characterization under native or near native environments such as lipid bilayers or membrane mimics are essential for a better understanding of the membrane protein's structure or function. Such membrane mimics will be introduced and further discussed in Sect. 1.2.

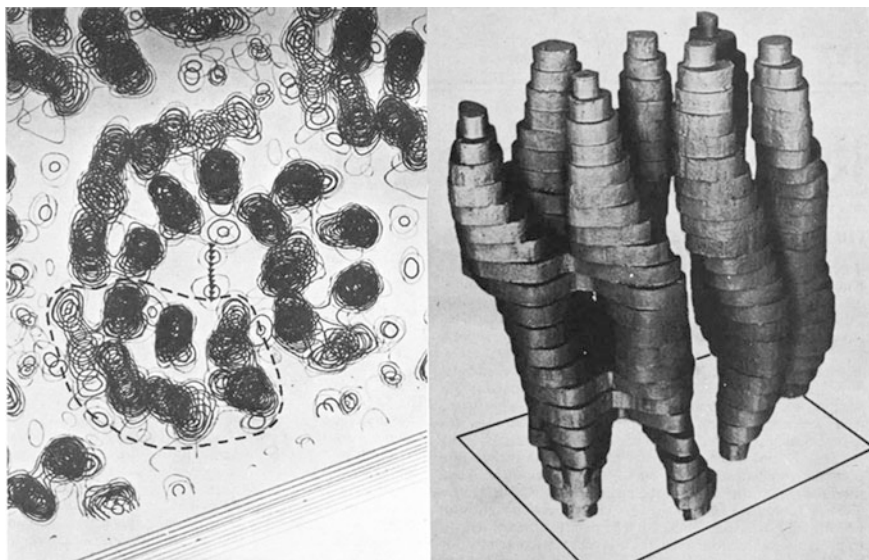


Fig. 1.1 Part of the 3D potential map (left) and 3D reconstruction model of a single bacteriorhodopsin in purple membrane (right), derived by Henderson and Unwin in 1975 using electron microscopy studying the 2D crystals. Reproduced and adapted with permission from Ref. [10], copyright 1975 Nature Publishing Group

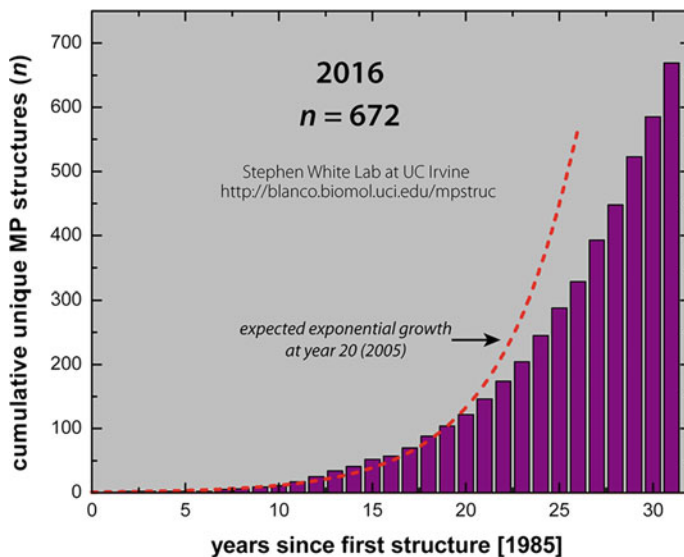


Fig. 1.2 Progress in membrane protein structure determination, where only unique structures are included in the statistic. Data published at <http://blanco.biomol.uci.edu/mpstruc/> (Accessed 14 June 2017)

1.1.1 Membrane Protein Structures

Membrane protein can be categorized into integral membrane protein and peripheral membrane protein. Integral membrane proteins are proteins that are permanently embedded on the membrane, and can be sub-categorized either as transmembrane proteins or those which reside on only one side of the membrane through an anchor.

Transmembrane proteins span across the membrane and often function as channels, transporters or receptors. They are inserted into the membrane and are exposed to mostly nonpolar environments, so that the side chains of the amino acids embedded in the membrane are usually hydrophobic. The carbonyl and amide groups on the backbones of the protein will therefore form hydrogen bonding networks with each other within the hydrophobic core of the membrane to achieve structural stabilization. To satisfy the requirements to minimize energy costs, the formation of α helical or β barrel secondary structures, shown in Fig. 1.3, is thus strongly favored for integral membrane proteins.

Transmembrane proteins with α helical structures are more abundant due to the fact that α helices form local hydrogen bonds. This property increases the flexibility of the transmembrane protein to undergo conformational changes, suggesting that α helical transmembrane proteins are more versatile in terms of structures and functions. Indeed, it is estimated that 27% of the total human proteome is α helical transmembrane proteins [14], with all plasma-membrane proteins being α helical.

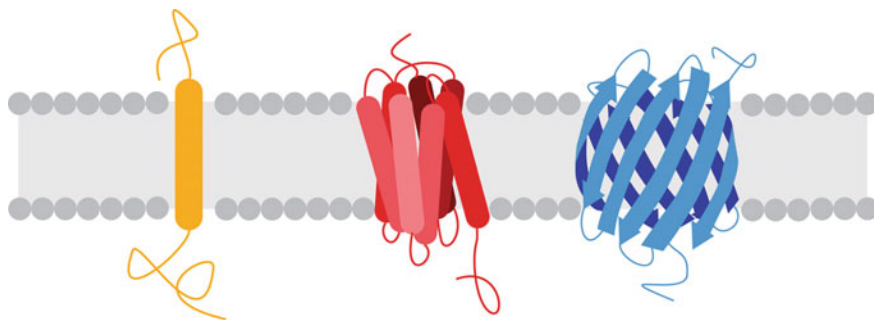


Fig. 1.3 Schematic representation diagram of the different types of integral transmembrane protein: bitopic transmembrane α helix (left), α helices bundle (middle) and β barrels (right)

They function as receptors, channels, transporters, electron transporters and redox facilitators [15]. Most notably, G-protein couple receptor (GPCR), the largest family of membrane protein in the human genome [16], shares a common structure of seven transmembrane helices [11, 16–21]. Alpha helices are mostly perpendicular or close to perpendicular to the membrane plane, where the different helices are connected between the ends [22]. They are also easier to be identified from sequence analysis, as the transmembrane segments require mostly hydrophobic side chains. Alpha helical bundle transmembrane proteins, unlike the bitopic single-pass α helical protein, often have the active site within the transmembrane bundles. Alpha helix bundled membrane proteins have remarkable diversity within their topology and quaternary structures. Shown in Fig. 1.4 are three very different arrangements. Monomeric bacteriorhodopsin shown in Fig. 1.4a is a classic seven-helix transmembrane protein (more details discussed in Sect. 1.4), where each of the transmembrane helices lie almost perpendicular to the membrane plane. The Cl^- channels on the other hand, shown in Fig. 1.4b, is a homodimer with each monomer having a Cl^- specific channel [23]. The subunit contains 18 α helices with most of the helices far from perpendicular to the membrane plane as well as helices that do not span the membrane completely. Shown in Fig. 1.4c is the Ca^+ -ATPase, which is formed with a central part and a peripheral part, which transfers Ca ions after a muscle has contracted and undergoes significant conformational changes during its ATP-driven pumping cycle [24, 25].

Alpha helical proteins with single transmembrane domains are characterized as single-pass transmembrane proteins, where type 1 membrane proteins (TM1) have their N-terminus on the cytoplasm side. Single-pass transmembrane proteins are involved in signaling pathways [26–28], and are suggested to compromise 6% of the proteins-coding genes in humans [29]. The transmembrane helices of such proteins were initially considered only as a hydrophobic anchor connecting two extra-membranous parts of the protein [30], however modern studies showed protein-protein interaction involving the single-pass transmembrane helix, where the proteins dimerize or oligomerize through their transmembrane domains [31, 32].

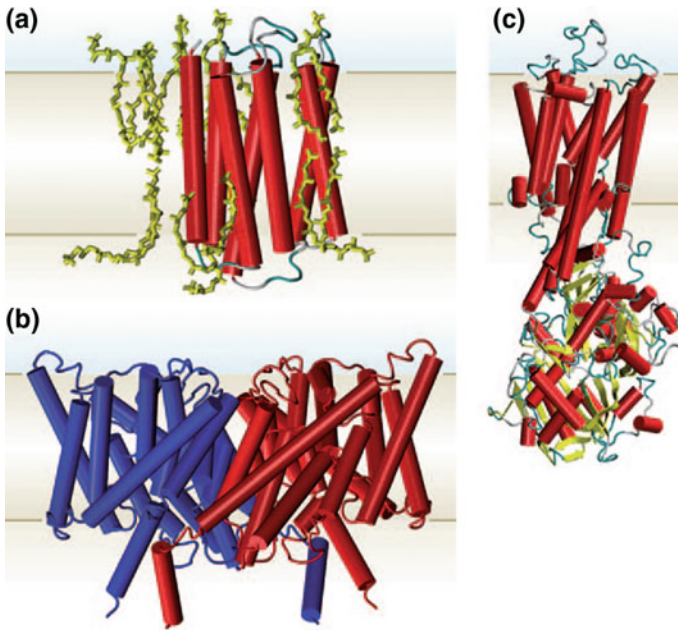


Fig. 1.4 Schematic of three different structures of α helical bundles, reproduced with permission from Ref. [182], copyright 2006 Nature Publishing Group. **a** Monomeric bacteriorhodopsin and co-crystallizing membrane phospholipid shown in yellow. **b** Homodimeric ClC Cl⁻/H⁺ antiporter from *E. coli*, with one subunit shown in red and another in blue. **c** Bovine Ca²⁺-ATPase, which has a central membrane embedding part and a peripheral part, experiences dynamic changes during functional cycles

While abundant α helices bundles are found in all biological membranes, the integral transmembrane proteins with β barrel structures are only found on the outer membranes of Gram-negative bacteria, mitochondria and chloroplasts [33]. Defined by “long-range” hydrogen bonds between the β strands, unlike the local hydrogen bonds of an α helix, The β barrel structure leaves only restricted mobility allowing little conformation changes. They are harder to be recognized in the sequence compared to the α helical transmembrane proteins, since not all residues in the β strands are required to be hydrophobic, making the hydrophobicity of membrane-spanning β strands similar to those of soluble proteins. Transmembrane β barrel can form with any even number of β strands, from 8 to 22, and can exist as monomers [34, 35], dimers [36] or trimers [37]. Beta barrel transmembrane proteins serve a variety of different functions, such a non-specific [34] or specific pores [38], active transporters [35] and enzymes such as proteases or lipases [36].

Other than integral membrane protein, another class of membrane protein is the peripheral membrane protein. Peripheral membrane proteins are defined as proteins that can associate onto the membrane non-permanently as well as exist in the aqueous environments away from the membrane [39, 40]. This covers a wide range

of protein folds, structures, and functions. Peripheral membrane proteins can attach onto the membrane via different interactions, including nonspecific electrostatic [41], hydrophobic patch [42], covalently bound lipid anchor [43], specific lipid-binding domains [44] and protein-protein interactions [45]. Peripheral membrane proteins are not exclusive to only one type of membrane binding method. While peripheral membrane proteins can exist in aqueous environments unlike integral transmembrane proteins, the interactions with biological membrane and mechanism remain a great interest in research due to their importance as well as their complexity.

1.1.2 Membrane Protein Characterization

Membrane proteins structures have been solved with various methods, but the main bottleneck of membrane protein studies remains to be sample preparation. Characterization of solubilized membrane protein can be studied using numerous methods prior to detailed structure determination. It is often the case in membrane protein research to have thorough preliminary characterization to check for sample homogeneity, structural and folding integrity, activity and stability. Size exclusion chromatography (SEC) [46, 47], analytical ultracentrifugation (AUC) [48] and light scattering (LS) [49] methods have been popular in assessing the homogeneity and the oligomerization of the solubilized membrane protein. Circular dichroism spectroscopy (CD) [50], infrared spectroscopy (IR) [51] and Raman spectroscopy [52] has been demonstrated to provide information of secondary structure, while isothermal titration calorimetry (ITC) [53] and fluorescence experiments have been used for ligand binding measurements which can determine the activities of some membrane proteins.

X-ray crystallography was used to determine the first structure of a soluble protein in the 1960s and the first atomic resolution membrane protein in 1985 [11]. Although some membrane proteins exist in large quantities in their native membrane, others can only be expressed with low production yield, causing a big problem for crystallography studies [54]. Protein must be extracted from the membrane using detergents before the membrane protein can be crystalized. However the type of detergent applied can significantly influence the success and the quality of the crystals. With most membrane protein studies, protein construct, buffer conditions and detergent used to extract or solubilize membrane protein must be carefully screened and optimized prior to structure determination or functional observations [55]. Membrane protein crystals are also often fragile to handle and suffer easily from radiation damage [56]. But with high throughput optimization and increased knowledge in handling membrane protein, x-ray crystallography can provide a strong structural understanding of the membrane proteins [57–59].

Electron microscopy (EM) can reconstruct three-dimensional structures of biological samples by obtaining a set of 2D projections. Due to the need to reduce radiation damage to biological specimens, high resolution information can only be

determined by averaging many different images of identical molecules under the same orientation. Cryo-electron microscopy (cryo-EM) is a particularly powerful method in the study of protein or membrane protein. The biological sample is frozen rapidly where the water is frozen into a thin layer of amorphous ice, which not only increases the contrast of the images compared to the use of staining, but also can preserve the biological samples in their native conformation [60]. For cryo-EM, the sample is not required to be crystalline and only a small amount of material is required. However, though those qualities are well suited for membrane protein studies, it is not without its own challenges. For example, the presence of detergents is often necessary to solubilize membrane proteins, but detergent can reduce the resolution due to its chemical composition as well as causing problems during vitrification. Moreover, studies of membrane protein using single-particle electron microscopy requires extensive data analysis, including image sorting and classification of projections and determination of orientation with respect to each averaged view. Extensive structural calculations and molecular modeling would then be performed before comparison to experimental data to determine the necessity of further refinement. Another approach to electron microscopy, other than the single particle approach, is electron crystallography. Although a crystalline sample is required as in the case in x-ray crystallography, instead of 3D crystals electron crystallography uses crystals of a single layer thickness, referred to as 2D crystals [10, 61]. The two dimensional crystal appears similar to a membrane environment and is often achieved by reconstituting purified membrane protein into a lipid bilayer. It has been demonstrated that some membrane protein can undergo distortion or conformational changes when packed in a three dimensional lattice, causing some disadvantages for x-ray crystallography.

Solid-state nuclear magnetic resonance (NMR) has been used to study membrane protein since it can study insoluble macromolecules that cannot be crystallized [62, 63]. NMR probes the nuclear magnetic moments with a strong static magnetic field and a secondary field generated by an external radio frequency (ν). In the case of NMR studies, the sample can be isotopically labelled, for example with ^{13}C , ^{15}N or ^2H , in order to enhance the signal-to-noise ratio of the NMR signals. Structure determination by solid-state NMR is not influenced by the size of the protein but by sensitivity and spectral resolution. To improve resolution, magic angle spinning (MAS) [64] is often employed, where the sample container is rapidly spun at high speeds (up to 80 kHz) around a specific angle in relation to the static magnetic field. At this angle, anisotropic interactions such as dipolar coupling and chemical shift anisotropy (CSA) can be reduced or removed.

As with any method of characterizing membrane protein, sample preparation remains the biggest factor in obtaining high quality results as sample homogeneity has significant effect on the spectral resolution. Lyophilization has been used extensively, but it has been demonstrated to cause side-chain conformational inhomogeneity. Microcrystalline protein sample is also a popular method, as the qualities of the crystal are not required to be at the level which x-ray crystallography demands.

Solution-state NMR is a drastically different methodology to solid-state NMR. In solution, the molecules tumble rapidly which averages out anisotropic interactions. This suggests a size dependence of the molecule of interest since as tumbling rate of bigger molecule decreases, line broadening occurs due to increases of anisotropic interactions, thus leading to a significant decrease of resolution. Moreover, structural studies of membrane protein using NMR requires the sample to be monodisperse and stable for moderate amounts of time during data acquisition, as well as isotopic labels to enhance sensitivity. However, recent developments have enabled successful structure determination of integral membrane protein in small membrane mimetic such as detergent micelles, lipid bicelles and nanodisc. NMR is a powerful tool in structural determination of membrane protein due to its unique ability to probe local structures while able to resolve detailed three dimension structures through different correlation assignments, providing NMR great potential in the study of membrane protein.

1.2 Membrane Mimics

As mentioned in the previous section, the main challenge in membrane protein study is the sample preparation. Membrane proteins are naturally found embedded in native lipid bilayers. Often membrane proteins are not soluble in aqueous solutions suggesting a membrane environment must be provided in order to satisfy the high hydrophobicity of the membrane proteins before carrying out biophysical characterization. However, biological membranes are complex, heterogeneous, dynamical systems which prove to be difficult to work with. It is therefore desirable to transfer the membrane protein of interest to a controlled and simpler environment that can satisfy the hydrophobic nature of the membrane protein as well as providing a near-native environment to allow the relevant structures or functions of the target membrane proteins to be characterized. In this section a few commonly used membrane-mimicking systems are introduced, while lipid nanodisc, shown in Fig. 1.5f, will be discussed further in Sect. 1.3.

1.2.1 Detergent Micelle

Detergents have been widely used in the study of membrane protein due to their ability to extract membrane protein from the membrane while solubilizing the hydrophobic membrane proteins [65–68]. This property allows for purification of the membrane protein as well as improving quality of crystallization [69]. Typical detergent molecules contain a polar hydrophilic “head group” and a hydrophobic hydrocarbon chain “tail”. At low concentrations, the detergent appears to be monomeric molecules in solution. However, when the concentration is sufficiently high, detergent molecules in aqueous solution would spontaneously self-assemble

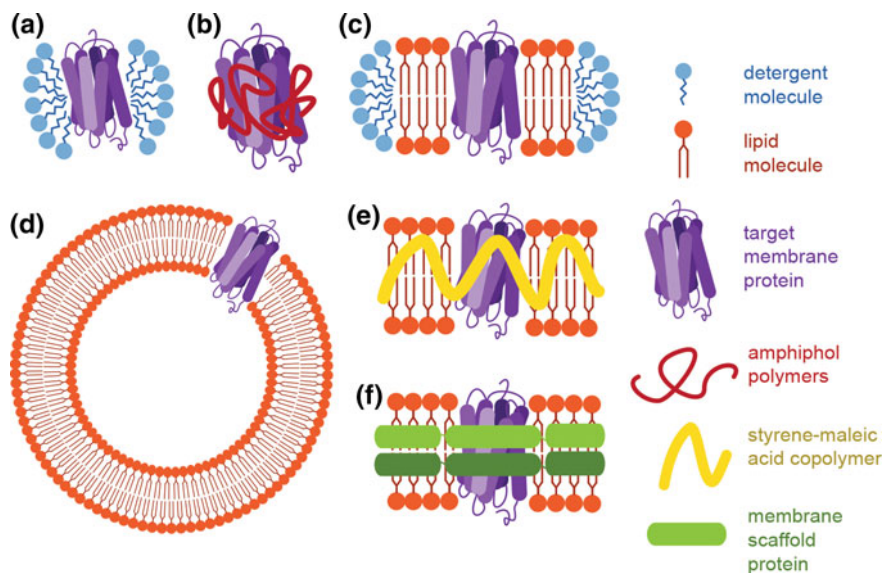


Fig. 1.5 Schematic diagram showing different types of common membrane mimics systems: **a** small detergent micelle surrounding the target membrane protein; **b** amphipols made up of amphiphatic polymers carrying hydrophobic chains, which wrap around the hydrophobic portion of the membrane protein; **c** small lipid bicelle composed of a mixture of detergent molecules and lipid molecules at specific ratios; **d** liposome consisting of phospholipid vesicle mimicking membrane bilayer structure; **e** SMALPs of small central core of lipid bilayer stabilized by amphiphatic polymer called styrene maleic acid copolymer and **f** lipid nanodisc of small central disc-shape core of lipid bilayer wrapped by two copies of amphiphatic helical proteins called membrane scaffold proteins

into spherical micelles, where the polar hydrophilic head would be solvent exposed while the hydrocarbon tails pack into a hydrophobic core. With this property, detergent molecules can imitate the membrane environment and protect the hydrophobic portion of the membrane protein, generating a soluble protein-detergent complex (PDC) shown in Fig. 1.5a. The lowest concentration for detergent micelle formation is called critical micelle concentration (CMC). Above the CMC, the monomeric detergent molecule concentration is independent of the overall detergent concentration, and the additional detergent molecules would be incorporated into the detergent micelle [67]. Common detergent and their CMC value can be found in Table 1.1.

Detergents can be classified according to their structures: ionic, non-ionic, bile acid salts and zwitterionic [70]. Ionic detergents contain a head group that carries an overall charge, either anionic or cationic. Ionic detergents such as the anionic sodium dodecyl sulfate (SDS), shown in Fig. 1.6a, can be harsh but effective in solubilization of membrane proteins, often causing denaturing of the membrane protein due to the fact it can disrupt the hydrophobic interaction within the protein. In some cases the membrane protein can be renatured or refolded after being

Table 1.1 Common detergents used in the study of membrane protein for structural analysis

Detergent	Molecular weight	CMC (mM)	Aggregation number
<i>Ionic</i>			
SDS	288	7–10	62
Sodium cholate	431	9–15	2–3
CTAB	364	0.9	61–169
<i>Non-ionic</i>			
TX-100	625	0.2–0.9	100–155
DDM	511	0.15	98
DM	483	~ 1.8	~ 69
OG	292	20–25	84
Digitonin	1229	<0.5	60
<i>Zwitterionic</i>			
CHAPS	615	6–10	10
CHAPSO	631	8	11
DPC	352	1.1–1.5	54
C7-DHPC	482	1.4	25
LDAO	229	1–2	74

transferred to another environment and the removal of SDS. Bile acid salts are also ionic, but unlike ionic detergents bile acid salts contain rigid steroidal groups. Bile acid salts such as sodium cholate, shown in Fig. 1.6b, have a polar and apolar face and behave as lipid emulsifiers. They are considered as relatively mild detergents and do not form traditional spherical shaped micelles. In both cases of ionic detergents, their aggregation is strongly affected by the ionic strength of their charged head groups.

Non-ionic detergents, on the other hand, are generally considered to be mild and relatively non-denaturing detergents, as they break only the lipid-protein and lipid-lipid interactions but not the protein-protein interactions as in the case the ionic detergents. This allows functional and structural studies of the membrane protein upon solubilization. Shown in Fig. 1.6c is Triton X-100, a compound containing a neutral head group followed by aromatic rings forming its hydrophobic parts. Due to its aromatic feature, Triton X-100 absorbs UV light and interferes with many spectroscopic methods monitoring protein concentration with 280 nm wavelength lights. Another example of a nonionic detergent is shown in Fig. 1.6d. *n*-Dodecyl β -D-maltoside (DDM) which is an alkylglucoside, has been demonstrated to successfully extract and isolate functional membrane protein from the membrane environments [71].

Zwitterionic detergents combine the properties of both ionic and nonionic detergents, thus their denaturing strength lie somewhere between the two types. Some examples of zwitterionic detergents include 3-([3-Cholamidopropyl] dimethylammonio)-2-hydroxy-1-propanesulfonate (CHAPSO) which is shown in Fig. 1.6e, Lauryldimethyl-amine-*N*-oxide (LDAO), which is considered a harsh

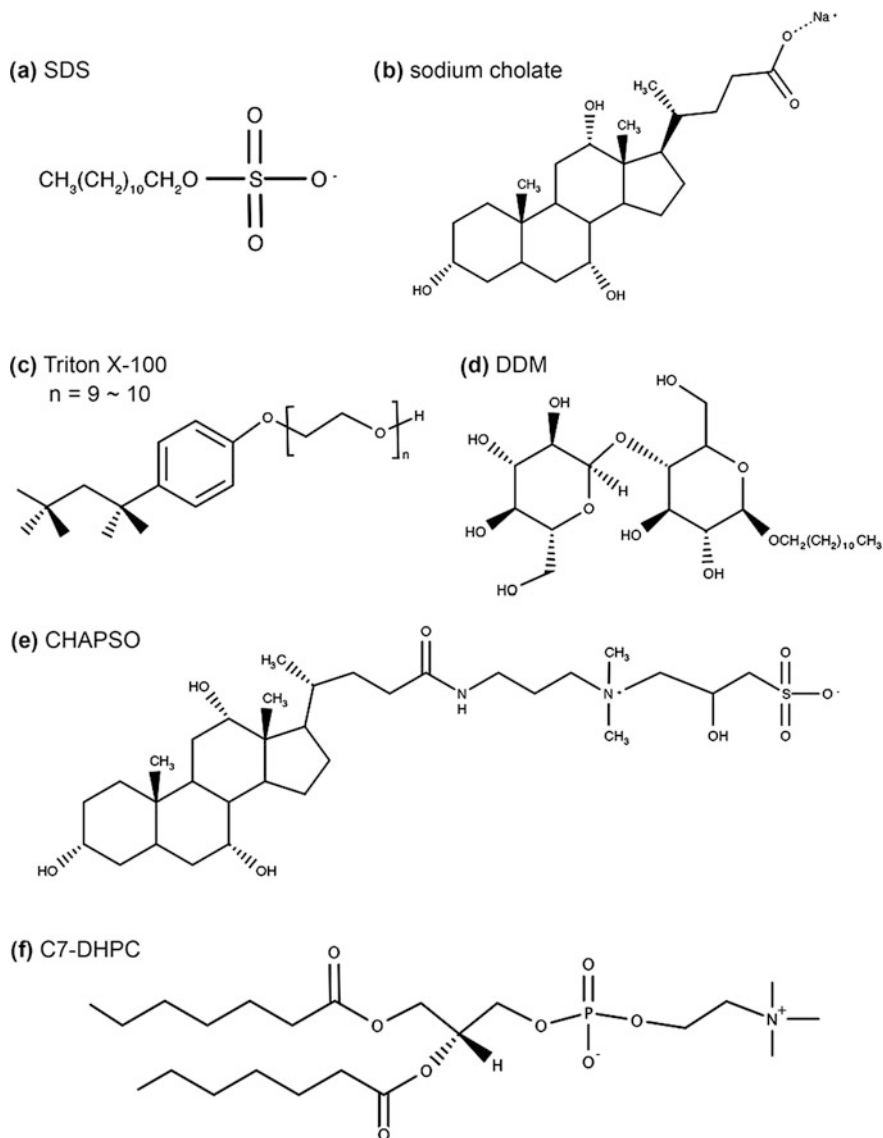


Fig. 1.6 Molecular structures of a few commonly used detergents in membrane proteins: **a** ionic detergent SDS, **b** bile acid salt sodium cholate, **c**, **d** non-ionic detergent Triton X-100 and DDM, and **e**, **f** zwitterionic detergent CHAPSO and C7-DHPC

detergent and n-dodecylphosphocholine (DPC), a zwitterionic detergent closely resembling a phospholipid with a phosphocholine head group directly bonded to a hydrocarbon chain. Another zwitterionic detergent is 1,2-diheptanoyl-sn-glycero-3-phosphocholine (C7-DHPC), shown in Fig. 1.6f,

which is a phosphocholine with short hydrophobic chains. For some membrane proteins zwitterionic detergents remain too harsh for functional studies, however zwitterionic detergents have been commonly used for crystallography.

The optimal choice of detergent for solubilizing a particular membrane protein can only be found through screening and trial-and-error [72–74]. The stability of the PDC, activity and structural integrity of the membrane protein in PDC remains complex and varies drastically between different membrane proteins. Moreover, membrane proteins are not guaranteed to be correctly folded even within mild detergents, and not all detergents are suitable for every characterization method. Size and structure of the detergent micelles and temperature stability must all be taken into account as well as its effects on the membrane protein. In some cases systems with mixed detergent micelle or a mixture of lipid and detergent can improve the quality of the design.

An excess of detergent might be used to ensure complete solubilization of membrane proteins, however such excess detergent can often complicate the system or disrupt further experimental studies. Detergents can be removed or exchanged from the system through various methods. Dilution of detergent to a concentration below its CMC would lead to the dissolution of detergent micelles, and the monomeric detergent molecule can then be removed via methods such as dialysis. However, for detergents with low CMC values, such as Triton X-100 and DDM where their CMC is about 0.2 mM, such procedure can be ineffective. Another method is using hydrophobic resins, or beads such as BioBeads (Bio-Rad), which interact with the hydrophobic detergent and absorb the detergent, thus removing the detergent from the system. This particular method is effective in removing detergents with low CMC, and the detergent coated beads can be separated from the sample using centrifugation or filtration. Chromatography methods such as ionic-exchange and gel filtration has been employed to remove or exchange detergent within the system. Because membrane protein can aggregate or become insoluble in the absence of detergents, buffer used for chromatography methods often contains a further detergent based on the chromatography methods. For example, if the membrane protein of interest contains polyhistidine tags, nickel column can provide an efficient way of transferring protein from one detergent environment to a different one. The protein bound to the column can be washed with the new detergent buffer prior to elution.

Detergent can be useful during extraction and purification of membrane proteins, but the conformation and structure of detergent micelle can deviate from the structure of the biomembrane, suggesting the use of detergent micelle for the study of membrane is not always ideal.

1.2.2 *Amphipols*

Amphipols are a family of amphipathic polymers that carry hydrophobic side chains and hydrophilic backbones, which can wrap around the hydrophobic portion

of the membrane protein and replace the detergent molecules, shown in Fig. 1.5b. The polymer can keep the membrane protein soluble while preventing the disruptive behaviour of detergent molecules [75, 76]. While in detergent systems free monomeric detergent can cause trouble during crystallization or viscosity increase, leading to poor resolution spectra or structure. By using amphipol one can significantly decrease the difficulties caused by excess free agents in solutions. The length and the charge of amphipol can be tailored to the membrane protein of interest. For a stable complex of amphipol and membrane proteins, the hydrophobic chain distribution of the polymer must be dense while being stable and flexible in aqueous solution. Amphipols have been demonstrated to have the ability of extracting membrane protein, but in most studies membrane protein was solubilized before transferring to the amphipol complex.

There is, however, concern over whether amphipol provides enough similarity to the lipid bilayer of biomembranes. Though amphipols have been demonstrated to extract lipid alongside membrane protein, it is difficult to assume the integrity of the lipid structure in the polymer-protein-lipid complex.

1.2.3 Lipid Bicelle

In the mixed detergent-lipid micelle systems, lipids remain the minor component while re-introducing some protein-lipid interaction. However, with certain mixtures of lipid and detergent, as the lipid to detergent ratio increases the two components can phase separate under specific conditions [77]. This leads to the formation of a small lipid bilayer disc with its edges enclosed and stabilized by detergent molecules, shown in Fig. 1.5c. Such a structure called bicelle [78], derived from bilayer mixed micelle, can offer a small planar phospholipid bilayer which resembles biomembranes, while optically transparent, making it suitable for many biophysical characterization such as NMR [79], crystallography [80] and optical spectroscopy [81]. Bicelles can be magnetically aligned, exploring the orientational orders in the system using both solution and solid-state NMR. Bicelle can adapt to a variety of different morphology other than the bilayer disc depending on the temperature, hydration, ratio of lipid to detergent and salt concentration [82]. It can also be designed to provide a small, isotropic bilayer environment that can tumble rapidly for well-resolved spectra. Due to its bilayer structure, bicelle systems have been demonstrated to have advantages over detergent micelle systems, particularly in solution state NMR [83–85].

On the other hand, bicelle formation requires specific detergents and lipid molecules at a particular ratio, limiting the choices of lipid composition in order to achieve stability. Moreover, bicelle requires high concentration of lipid to overcome the CMC of the detergent molecules, which can be problematic for studies that require adjustments of concentration.

1.2.4 Liposome

A liposome is a particle with a closed lipid bilayer, shown in Fig. 1.5d. Liposomes resemble the bilayer structure of biomembrane and thus can provide a better chance of maintaining membrane protein structural and functional integrity. The sizes of the liposome can range from a diameter of 10 μm (giant unilamellar vesicles, GUV), to 100 nm (large unilamellar vesicles, LUV) or 20 nm (small unilamellar vesicles SUV), depending on the preparation method. While large liposomes have low curvature and thus provide a more native-like local environment for embedded membrane protein, smaller liposomes can have a faster tumbling rate and higher concentration. Developed since the 1970s [86], various membrane proteins have been studied by reconstitution into liposome [87, 88].

Reconstitution of membrane protein into liposome can be challenging. There are different methods to achieve this, such as detergent mediated transfer and organic solvent-based transfer. Because membrane protein can often be denatured in the presence of organic solvent, detergent mediated transfer is often preferred. In such a procedure membrane proteins are first extracted and purified in the presence of detergent, before detergent solubilized lipids are added and mixed. Once the detergent is removed, using a variety of different methods mentioned in Sect. 1.2.1, liposome would form with membrane protein incorporated. Reconstitution efficiency of membrane protein into liposome can depend strongly on the initial detergent concentration, the properties of the target membrane protein, lipid composition and the rate at which detergent is removed [89].

It is difficult to verify whether the membrane proteins reconstituted into liposome evenly and with the correct orientation. Demonstrated in the studies of Ca^{2+} -ATPase [90] and BK potassium channel [88], the orientations of membrane protein inserted into membrane of liposome are not uniform. The size distribution of liposome is bigger compared to other membrane mimicking systems. Such inhomogeneous samples can cause problems for detailed biophysical studies and further complicate the findings.

1.2.5 Styrene-Malic Acid Copolymers

Recently it was discovered that an amphipathic organic polymer, styrene-malic acid (SMA) copolymer [91], has the ability to solubilize membrane to extract membrane protein and form polymer-protein-lipid molecules called SMA-lipid particles (SMALPs) [92], or Lipodisq particles [93], shown in Fig. 1.5e.

SMA copolymer is a hydrolyzed form of styrene malic anhydride (SMAhn) copolymer. SMAhn is synthesized by the radical polymerization of maleic anhydride and styrene monomers, shown in Fig. 1.7. The ratio between styrene and malic acid/anhydride monomers in the copolymer can be varied by monitoring the feed ratio of the polymerization process, but due to the difference in reactivity in the

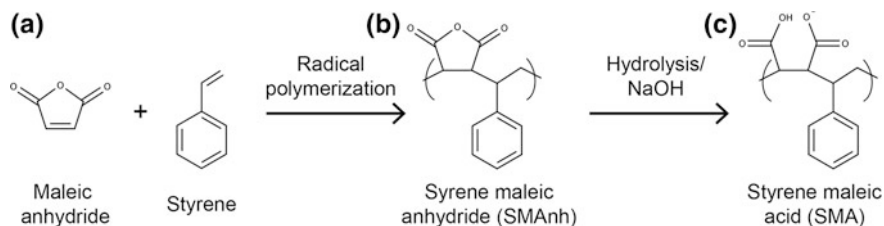


Fig. 1.7 Schematic diagram of the synthesis of SMA copolymer, from monomeric maleic anhydride and styrene (a) to SMAnh (b), which is converted to SMA (c) by hydrolysis

chain [94, 95] the reaction often does not produce regularly repeating blocks nor a random distribution. If the reaction was carried out in a batch-wise manner, the ratio of styrene and maleic anhydride would be the same as the feed ratio, but the sequence along the chain might vary significantly [96]. The distribution of the monomeric units can be improved by performing the polymerization in a continuous manner [96, 97]. However, even with continuous feed method, the resulting production is still inhomogeneous in both length of polymer chains and in composition. The copolymer has a wide distribution of molecular weights, and it is not clear how such heterogeneity affects the function of SMA copolymer as a membrane solubilization agent [98]. Only the hydrolyzed acid form of SMA is water-soluble and can solubilize membrane. The hydrolysis of SMAnh into SMA is by mixing SMAnh with water or with alkaline solution, and then the SMA copolymer can be further purified by repeatedly adjusting the pH of the solution to precipitate the SMA polymer then resolubilizing the precipitate [99].

SMA copolymers have been demonstrated to extract membrane lipid and membrane protein from the membrane without the use of detergent to form SMALPs [92], via electrostatic interaction followed by hydrophobic effect [100]. The formation of SMALPs from large membrane vesicles can be monitored by the cloudiness of the assembly mixture. SMALP contains a lipid bilayer wrapped by SMA copolymer, which covers the hydrophobic portion of the lipid bilayer thus stabilizing the complex. SMA copolymers could extract membrane protein from either synthetic liposomes [93] or from biological membrane [101–103], with the latter often referred to as native nanodisc. The sizes of SMALPs have been studied using EM [100, 104–106], SEC [100, 107], DLS [92, 93, 100] and SANS [104], and have been reported in the scale around 10 nm. SMALPs were shown to preserve the majority of the lipid composition as well as the membrane protein [101, 102, 108], and the protein activity and structure were characterized using a variety of different experimental methods [92, 93, 105, 107, 109, 110]. The interaction between SMA and lipids in SMALPs has been studied using FTIR, NMR and DSC [104], as well as EPR [93], and found SMALPs to behave similarly to nanodisc bound by membrane scaffold protein, which will be introduced in Sect. 1.3. Unlike the nanodisc bound by membrane scaffold protein, SMA only absorbs low amounts

of UV range signal [99], making the UV-detection based characterization such as CD and IR of incorporated membrane protein easier in comparison.

However, there are several limitations of using SMALPs. It is unknown if or how the heterogeneity of the polymer molecular weight, which can vary up to an order of magnitude between the smallest and the biggest polymer chains in a typical preparation, affect the membrane solubilization properties of SMA, or the sizes of SMALPs. While the reported sizes of SMALPs were in range of 10 nm with minor variation, the factor that determined the size of SMALPs has not been investigated. For these reasons, the number of SMA polymers per SMALPs is difficult to determine, or whether all of the polymers are involved in the solubilization of the lipid-polymer complex [98]. One particular disadvantage of SMALPs is the dependency on pH. SMA polymers are only soluble above pH 6.5 due to the pKa of carboxyl groups in the maleic acid units [91, 99, 111]. At lower pH, the hydrophobic effect dominates and causes GMA to adopt a globular conformation and precipitate as aggregates. Another constraint of SMALPs is the limitation on presence of divalent cations such as Mg^{2+} and Ca^{2+} , as SMA copolymers behaves as chelators [99]. Once the divalent cation concentration increases above 5 mM, SMALPs are disrupted and SMA copolymer will precipitate from the solution. Those properties can significantly limit the condition of which the membrane protein embedded on SMALPs can be studied.

1.3 Nanodisc

Nanodisc is a new membrane mimicking system used in the study of membrane protein. It is a nanoscale high-density lipoprotein containing a central disc-shaped core of phospholipid bilayer. Shown in Figs. 1.5e and 1.8, the lipid bilayer disc is

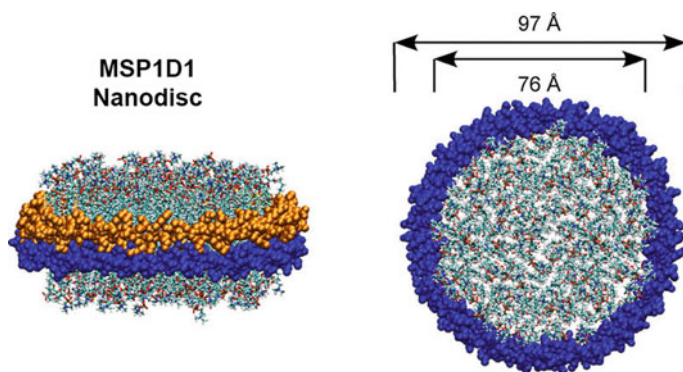


Fig. 1.8 Illustration of nanodisc structure composed of MSP (MSP1D1) and phospholipid from side view (left) and top view (right). The two MSP belts are shown in colored orange and blue. Adapted with permission from Ref. [183], copyright 2009 John Wiley and Sons

wrapped with two copies of an amphipathic α helical protein called membrane scaffold protein (MSP), which encloses the disc and stabilizes the membrane protein-lipid complex.

MSP was designed using the template of human apolipoprotein A (apo A-1). Apo A-1 is a plasma protein and it accounts for approximately 75% of the protein content of high-density lipoproteins (HDL) [112]. HDL particles can pick up and transport cholesterol through various pathways, mediating the efflux of cellular cholesterol [113]. Due to the importance of HDL functions, apolipoprotein has been extensively studied and shown to have amphipathic helices, allowing the association with lipid and cholesterol particles to form a water soluble complex. The lipid protein complex can be assembled using purified apolipoprotein and lipid particles, with the apolipoprotein arranged as amphipathic helical belts wrapped around the lipid supramolecules [114–116].

Using the disc model, of which two helical belts of apolipoprotein surround a disc shaped lipid bilayer [117], MSP was designed to self-assemble into small lipid bilayers stabilized by amphipathic helical proteins. Containing the protein sequence found in human apo A-1 but without the globular N-terminal domains [118], MSP readily assembles into discoidal particles with synthetic phospholipids upon detergent removal [119]. This provides a near-native like lipid environment with lipid-bilayer and, unlike lipid bicelle, is detergent-free. When the nanodisc assembles under the optimized lipid to MSP ratio, the discs produced were shown to be homogenous in size, and the size is governed by the length of the MSP used in the nanodisc assembly. Demonstrated by Denisov et al., the sizes of the nanodisc composed of POPC and with DPPC, calculated using HPLC data and with experimental fitting of SAXS data, appear to be the same thus confirming that the size of nanodisc is determined by the length of the MSP [120]. Moreover, they showed that the deletion of the first 22 amino acids from the first helical segment did not significantly change the number of lipid particles in the nanodisc, despite the first helix of the human apo A-1 being presumed to be an essential part in modelling of analogues discoidal particle [121].

The basis for the formation of nanodisc with target protein incorporated is that the membrane protein is completely solubilized in the compatible detergent in the nanodisc assembly mixture. As highlighted in the previous section, screening of such conditions is crucial and non-trivial in membrane protein research, as membrane protein can still form aggregates, time-dependent aggregates or concentration-dependent aggregates while solubilized. On the other hand, if the solubilization of the membrane protein of interest can be achieved, then upon detergent removal the protein can self-assemble with the lipid particles and MSP to form lipid nanodisc. Even though the exact mechanism of the self-assembly of nanodisc is yet to be demonstrated, it is believed that upon detergent removal the relevant lipid-lipid interaction and the lipid-protein interaction will take over and traps the membrane protein within the lipid bilayer disc. This suggests the possibility that the formation of the nanodisc can be affected by the rate of detergent removal, similar to the case in liposome.

With the ability to provide a monodisperse, well-controlled phospholipid bilayer environment, nanodisc quickly became popular in membrane protein research, particular in the fields of EM and NMR [122]. The high size homogeneity as well as ability to prevent aggregation significantly improved sample quality for EM characterization. Numerous EM studies of isolated and functional membrane protein complex using nanodisc have been done, as well as 3D structural reconstruction of membrane protein [123–125]. With its capacity to prevent aggregation at high concentration while maintaining membrane structure and stability, nanodisc became a powerful tool for studying membrane protein using solution state NMR. Although still bigger than detergent micelle, nanodisc can provide a stable membrane environment with a rich choice of lipid composition. Nanodisc has been successfully used for NMR experiments with membrane proteins such as outer mitochondrial VDAC [126, 127], potassium channel KvsA [128], voltage sensing domain of KvAP [129], bacterial outer membrane assembly factor BamA [130], and human CD4 [131]. Demonstrated by Hagn et al., the atomic-resolution structure of bacterial outer membrane OmpX in nanodisc showed a significant difference to the membrane protein compared to the same protein in DPC detergent micelle [132].

Nanodisc provides advantages for structural studies due to its ability to provide small, size homogenous lipid bilayer platform embedding membrane proteins. Another benefit of using nanodisc over systems like liposome or detergent micelles is that nanodisc has been shown to be able to distinguish between monomeric and oligomeric population. The size of the nanodisc can prohibit the self-aggregation dynamics by allowing only one target protein present per disc. This was demonstrated in the case of CYP3A4, a human hepatic drug metabolizing cytochrome P450, where the state of aggregation can have a significant effect on its function [133, 134]. Nanodisc provided a straightforward method to study the function of CYP in phospholipid bilayer in monomeric form and prevent further complication arising from heterogeneous sample preparation. GPCR rhodopsin has been reconstituted into nanodisc in monomeric and dimeric form in order to understand signal transduction and oligomeric states [135].

1.4 Bacteriorhodopsin

Bacteriorhodopsin (bR) was among one of the first membrane proteins to be extensively studied. Discussed in Sect. 1.1, it was the first membrane protein to have its structure revealed, from two dimensional crystal using electron microscopy [10]. Bacteriorhodopsin was also the first integral membrane protein studied by intensive mutagenesis [136], and the first to be fully unfolded and refolded in vitro [137, 138]. This is due to the fact that bacteriorhodopsin has relatively high stability, particularly for an integral membrane protein, and is not difficult to obtain in large quantities. Thus it has been used as a test target protein for the development of numerous experimental methods or sample preparations throughout the years. Indeed, it was

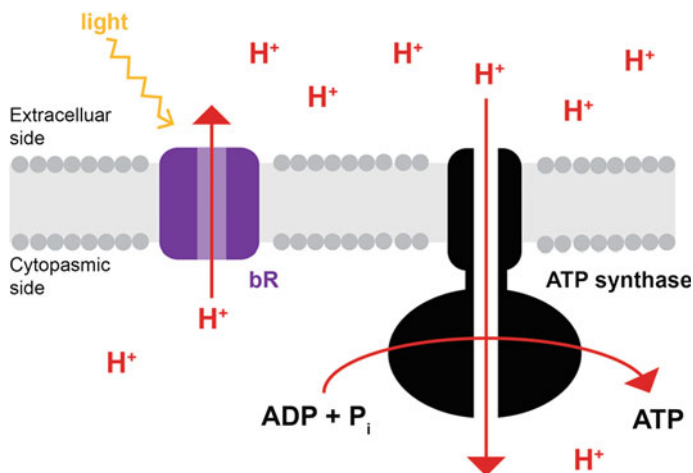


Fig. 1.9 Schematic of photosynthesis of *Halobacterium salinarium*, where bR works with ATP synthase on the inner cell membrane. The photon from the sun is absorbed to trigger proton translocation towards the extracellular side, then the proton would enter the membrane through ATP synthase, converting ADP to ATP

among the first membrane protein to be successfully incorporated into nanodisc, where the function of the protein was demonstrated to be preserved [139].

Bacteriorhodopsin is a light-driven proton pump [140]. Upon excitation of light, the protein would transfer protons from the cytoplasmic side to the extracellular side, inducing an electrochemical proton gradient across the cell membrane. The proton would then flow back into the cell through ATP synthase, another integral membrane protein, and be used in the production of adenosine 5'-triphosphate (ATP), shown in Fig. 1.9. ATP is the universal energy currency used in living cells. When ATP undergoes a reaction that cleaves one of the high-energy phosphoanhydride bonds to form ADP and a phosphate, the energy released from the reaction can power most biological processes such as synthesis, growth, maintenance and replication. Thus, coupling bacteriorhodopsin and ATP synthase allows the organism to convert light energy into chemical energy to survive harsh surroundings and nutrient starvation.

bR is an integral membrane protein of roughly 26 kDa [141]. It consists of seven transmembrane α helices, two β sheets [142] and a retinal chromophore molecule that is covalently linked onto the protein via a protonated Schiff base and a lysine residue [143]. This retinal is closely linked to the protein's proton pumping function, as the change of conformation of the retinal molecule would trigger the proton passing process.

1.4.1 *Halobacterium Salinarum*

Many of the studies on bacteriorhodopsin are from *Halobacterium salinarium*. Bacteriorhodopsin is the only protein constituent of the purple membrane of *H. salinarum* [144], a halophilic archaea. Bacteriorhodopsin of *H. salinarum* (HsbR) was first isolated in the form of purple membrane (PM) by Stoeckenius and Rowen in 1967 [145]. Oesterhelt and Stoeckenius later discovered the rhodopsin-like protein, similar to that of human rhodopsin, embedded on the purple membrane using absorption spectroscopy [144]. The proton pumping function of bR was determined in 1973, where they found upon illumination the absorption maxima of PM shifts from 560 to 415 nm and the shift was accompanied by a change in pH, suggesting an release and uptake of protons [146]. The protein was then extensively studied using various methods, for example Resonance Raman spectroscopy [147], Fourier transform infrared spectroscopy (FTIR) [148] and site-directed mutagenesis [149], leading to a detailed characterization of bR function and mechanism. Furthermore, bR was successfully crystallized as a 3D crystal, allowing higher resolution structural determination. Together with functional research, the behavior of bR has been well studied.

HsbR goes through a photocycle of several intermediate states, each with a different absorption wavelength, during the proton pumping process, shown in Fig. 1.10. Each intermediate state is closely related to the conformational change of the retinal and the hydrogen-bonding environment around the retinal pocket [150]. The retinal molecule is attached onto the protein through a protonate Schiff base via K216 of helix G, shown in Fig. 1.11a.

The protonated Schiff base of the retinal molecule forms a hydrogen bonding network with nearby D85 (from helix C), D212 (from helix G) and water molecule [151], thus making the photocycle reaction center. When the protein is exposed to

Fig. 1.10 Photocycle of bacteriorhodopsin in the purple membrane. The smaller number beside each intermediate states represents the absorption wavelength of the corresponding state

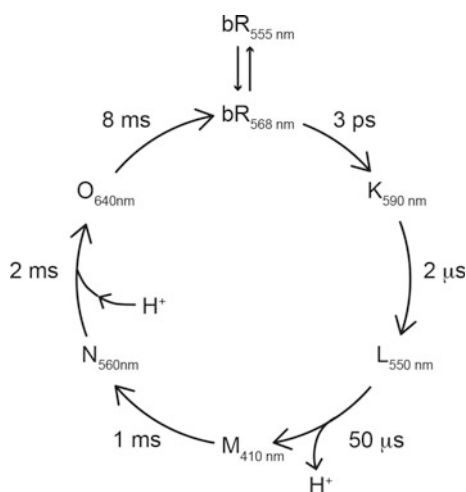
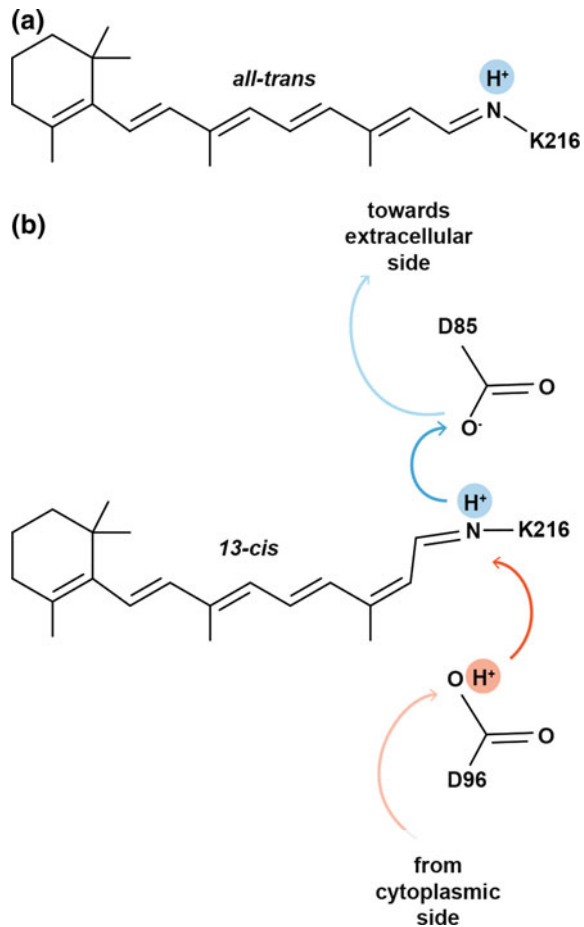


Fig. 1.11 Retinal conformational change causing proton translocation. **a** Retinal molecule is covalently linked to the protein via a protonated Schiff base to Lysine 216. **b** After absorption of light the retinal changes conformation from *all-trans* to *13-cis* and initiates proton translocation from the Schiff base



illumination, the retinal molecule changes conformation from *all-trans* to *13-cis*, and generates intermediate K [152]. The generation of intermediate K is a photochemical reaction, while the following intermediate states resulted from thermal reactions [153]. The isomerization leads to the proton on the Schiff base migrating towards D85, following the blue arrow in Fig. 1.11b, corresponding to the transition from intermediate L to intermediate M [154]. The generation of intermediate M coincides with the proton being released towards the extracellular side through a network of hydrogen bonds involving E194, E204 and D82 [155, 156]. The Schiff base is reprotonated from the proton donor D96, shown in the orange arrow in Fig. 1.11b, which leads to the decay of intermediate M and transitions into intermediate N [157]. The formation of intermediate O state corresponds to the re-isomerization of the retinal from *13-cis* to *all-trans* [158], as well as the reprotonation

of D96 with the proton collected from the cytoplasmic side through D36, D102, D104 and E161 [159]. The decay of intermediate O and return to the initial ground state is attributed to the passing of proton from D85 to E204 and the relaxation of the retinal [160].

On the purple membrane (PM), bR exists as a hexagonal lattice of trimers, shown in Fig. 1.12 [161–163]. The PM consists of 75% bR and 25% lipid by weight, with each bR surrounded by 10 lipids [162, 163], including glycolipids, phospholipids, squalene and traces of vitamins. Lipids and lipid-to-retinal molar ratios determined by Corcelli et al., using ^1H and ^{13}P NMR [163] are listed in Table 1.2, with their structures shown in Fig. 1.13. The lipid molecules found in PM not only make up the membrane composition, but also perform various functions such as maintaining bR's trimeric form [164, 165] and are involved in the process of proton transport [166]. The membrane of PM is also found to have a significant influence over the photocycle kinetics of bacteriorhodopsin [167], where the interactions between specific native PM lipids and bR were found to be crucial for maintaining the conventional bR photocycle activity [168, 169].

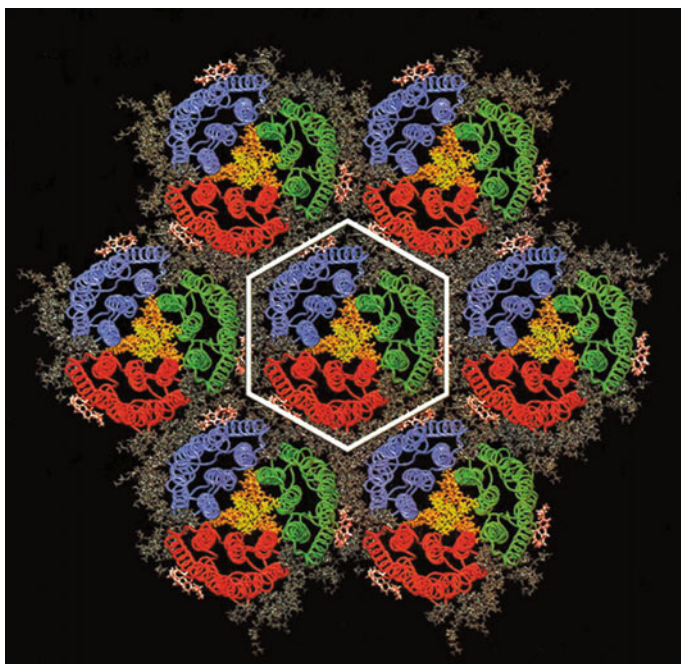


Fig. 1.12 Structure of bacteriorhodopsin on the purple membrane. bR exhibits a trimeric conformation, with the green, red and blue represents a different monomer. The different PM lipids are shown in different colors, where extratrimer PGP is shown in grey, intratrimer PGP in yellow, extratrimer squalene molecule in purple, intratrimer glycolipids in orange. Reprint with permission from Ref. [184], Copyright 2001 American Chemical Society

Table 1.2 Lipid to retinal molar ratios in the total lipid extract of PM, determined using ^{13}P and ^1H NMR, reported by Ref. [163]

Lipid	Lipid-to-retinal ratios
S-TGD-1	3
GlyC	1
PGP-ME	2.4
PG	1.2
PGS + BPG	0.37
SQ	2
Vitamin MK-8	Traces

1.4.2 *Haloarcula Marismortui*

After the discovery of HsbR, several other bR-like proton pump proteins from different halophiles were discovered [170–173]. In most cases, each organism was found to contain only one photo-active ion-pumping protein, related to its mechanism and environment [174]. An example of a protein containing more than one light-induced channels is unicellular green algae, containing two channel-rhodopsins, ChR1 and ChR2 [175]. The two different channelrhodopsin have different absorption wavelength and mediates photoaxis, movement responding to light. *Haloarcula marismortui* is another system that was found to contain two pumping channels [176], however both pumps are proton pumping bR rather than two different functional channels [177, 178]. Shown in Fig. 1.14, bacteriorhodopsin of *Haloarcula marismortui*, HmbRI and HmbRII, shares 50% amino acid sequence with HsbR [179]. The retinal pocket and proton translocation related residues were highly conserved, suggesting the same proton pumping function to HsbR using similar mechanisms [174]. Demonstrated by Tsai et al., HmbRI and HmbRII follow slightly altered photocycle pathways, shown in Fig. 1.15 [174]. The photocycle of HmbRI is similar to the conventional photocycle of HsbR with an additional new intermediate M', likely attributed to the retinal reisomerization prior to reprotonation. Whereas HmbRII has a small alteration in the photocycle pathway where no intermediate O population was found, which might originate from the negatively charged residues on the cytoplasmic side trapping the proton, and delay the protonation of proton donor D101 [174]. The study of the photocycle revealed that HmbRI has a faster photocycle, suggesting a higher efficiency in proton pumping, while HmbRII performs better under acidic conditions found in the Dead Sea, where *H. marismortui* thrived. The dual proton pumping mechanism provides flexibility to aid survival in harsh environments [174].

HmbRI and HmbRII can be expressed using *E. coli* and can be purified using Ni-NTA affinity methods [177]. This allows a high quantity of protein production for biophysical characterization and crystallization [180]. HmbRI with a single mutation at aspartic acid 94 to asparagine was reported to drastically increase the expression yield, and can be used as a fusion tag for the production of other membrane proteins [179]. HmbRID94N corresponds to HsbRD96N, which is a key residue involved in proton translocation described previously. The photochemistry

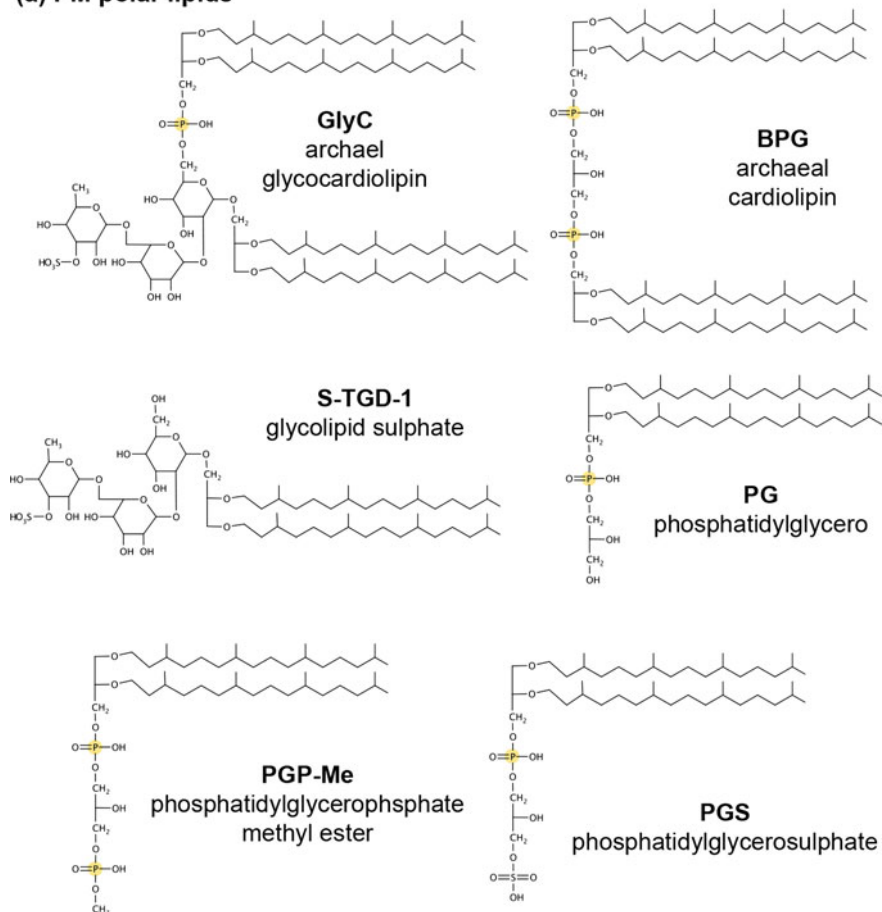
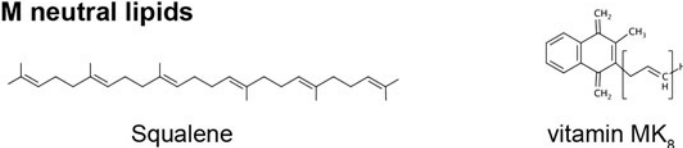
(a) PM polar lipids**(b) PM neutral lipids**

Fig. 1.13 Structure of the purple membrane **a** polar lipids and **b** neutral lipids, as reported in Ref. [163]. the phosphorus is highlighted in yellow

properties were demonstrated to be preserved in HmbRID94N [179], and the mutation was not expected to introduce structural changes in the protein ground state [153, 181]. Despite the *E. coli* expression and hence a lack of native lipids, HmbRID94N was found to be trimeric in the protein crystal [180].

	1								
HsbR	QA-----QIT	GRPEWIWLAL	GTALMGLGTL	YFLVKGMGVS	DPDAKRKYAI	TTLVPAIAFT	MYLSMLLYG		
HmbRI	MP-----A--	PGSEGIWLWL	GTAGMFLGML	YFIARGWGET	DGRRQKFYIA	TILITAIQFV	NYLAMALGFG		
HmbRII	MLPLQVSSLG	VEGEGIWAL	GTVGMLLGMV	YFMAKGDWVQ	DPEQEEFYVI	TILLAGIAAS	SYLSMFFGFG		
	71								
HsbR	LTMVPP--GGE	QNPIYWARYA	DWLFTTPLLL	LDLALLVDAD	QGTILALVGA	DGIMIGTGLV	GALTK-----		
HmbRI	LTFIEF--GGE	QHPIYWARYT	DWLFTTPLLL	YDLGLLAGAD	RNTIYSLVSL	DVLMIGTGVV	ATLSAGSGVL		
HmbRII	LTEVELVNGR	VIDVYWARYA	DWLFTTPLLL	LDIGLLAGAS	NRDMAEITIT	DAFMIVTGLA	ATLMK-----		
	141								
HsbR	-VYSYRFVWV	AISTAAMLYI	LVVLPFGPTS	KAESMRPEVA	STFKVLRNVT	VVLSANPVV	WLIQSEGAGI		
HmbRI	SAGAERLVWV	GISTAFLVLV	LYFLPSSLSG	RVANLPSDTR	STFKLRNLV	TVVWLVPVW	WLVGSEGLG		
HmbRII	-VPVARYAFV	TISTTAMLFV	LYLVVVVGE	AASDASEEAQ	STFNVLNRNI	LVAWAIYPVA	WLVGTEGLGL		
	211								
HsbR	VPLNIETLLF	MVLDSAKVVG	FGLILLRSRA	IFGEAEAPEP	SAGDGAATTS				
HmbRI	VGIGIETAGF	MVIDLVAKVG	FGIILLRSHG	VLDGAAETTG	TG--ATPAD				
HmbRII	VGLFGETLLE	MILDITAKIG	FGFILLRSRA	IVGGDSAPT	SA----EAAD				

Fig. 1.14 Sequence alignment of different bacteriorhodopsin HsbR, HmbRI and HmbRII, where the position of HmbRID94N is marked by an open circle, and the lysine bound retinal via Schiff base is marked with a filled star

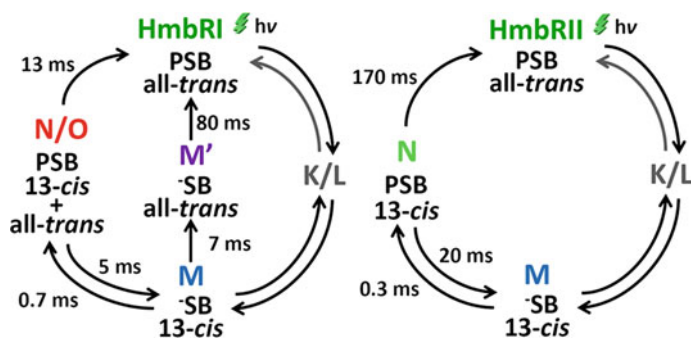


Fig. 1.15 Schematics of photocycle pathway of HmbRI (left) and HmbRII (right), adapted with permission from Ref. [174]. Copyright 2015 American Chemical Society

1.5 Motivation of Thesis

Nanodisc has shown to be a powerful tool in the research of membrane protein, both for detailed work on structural elucidation and also function related studies. However, much of the focus has been on the target membrane protein embedded in the nanodisc yet little on the properties of nanodisc itself. It is important to understand the influences of the properties of nanodisc, such as lipid composition and size of the nanodisc, in order to allow us to utilize the properties to control and manually tune the membrane protein of interest for the designs of the characterization methods. It is also important to keep in mind how those properties of nanodisc can affect the function or the structure of membrane protein, while considering the experimental designs.

Using bacteriorhodopsin as a model membrane protein and taking advantage of its production yield and stability, this work aims to demonstrate how the properties

of nanodisc such as lipid composition and size might influence the function of the membrane protein embedded on the nanodisc. In particular, the function of bacteriorhodopsin can be monitored by the study of its photocycle kinetics using time resolved absorption spectroscopy. Methods and the relevant backgrounds are introduced in Chap. 2. By combining the different chromatography and spectroscopic methods, bR embedded nanodisc can be prepared and characterized.

The effect of different lipid compositions of nanodisc on the embedded bacteriorhodopsin was investigated and demonstrated in Chap. 3. Utilizing the fact that lipid composition does not affect the size of the nanodisc and that nanodisc provide a well controlled lipid environment, we were able to perform systematic studies on the effect of lipid composition on the function of bR. We were able to successfully incorporate bR into nanodisc of different ratios of lipids with neutral and negative hydrophilic heads, as well as lipids with saturated or unsaturated hydrocarbon chains. The results of time resolved difference spectra indicate that the photocycle kinetics of bR is significantly influenced by the charge of the hydrophilic lipid head, altering both the duration and the pathway of a single pathway. Further analysis using photochemical measurement suggests that not only does the lipid affect the photocycle kinetics, but also plays a part in the proton release by the protein during the photocycle. The structure of the hydrophobic lipid tails was also shown to have minor contribution to the photocycle kinetics of bR. Therefore we demonstrate that the function of transmembrane protein can be tuned in controlled manner by adjusting the lipid composition of nanodisc.

The effect of the size of nanodisc on the embedded bacteriorhodopsin is studied in Chap. 4. Rather than isolating bacteriorhodopsin from *H. salinarum*, HmbRID94N expressed using *E. coli* was used to avoid native lipids of *H. salinarum*, which may be incorporated in different amounts into nanodisc of different sizes. The sizes of the nanodisc are controlled by the lengths of the membrane scaffold proteins, and the product is size homogeneous. By using modified MSPs with chemically joint C and N termini, monomeric bR incorporated into nanodisc were compared to monomeric bR in detergent micelle, to reveal significant changes in photocycle kinetics and photocycle active population. However, bR embedded in different sizes of nanodisc with the same lipid composition showed no significant difference in photocycle durations. This could be due to the slow photocycle kinetics caused by the amino acid mutation, as preliminary results from the study of bR from *H. salinarum*, with native lipids removed by detergent, incorporated into nanodisc showed a difference in the photocycle lifetime between different sizes of nanodisc. This suggests the sizes of the nanodisc play only a minor factor in the study of membrane protein, and the effect is dependent on the function and dynamic of the membrane protein.

We showed by adjusting the lipid composition one can manipulate the function of membrane protein, but we also showed that the use of synthetic lipid molecules can deviate from the true native environment despite a similar bilayer structure, as the lipid property can influence the function of the membrane protein. Inspired to study membrane protein in an environment as close to its native biological membrane while allowing biophysical characterization, we show in Chap. 5 a novel

method to extract bR and its native lipids from the purple membrane, and incorporate them into nanodisc without any additional synthetic lipid molecules or lipid extracts. By using the modified MSP with the chemical linked N and C termini, we have successfully extracted bR with the essential native PM lipid where the trimeric conformation and the function of bR were preserved. The native purple membrane nanodisc assembled using membrane scaffold protein showed a greater flexibility over assembly and characterization conditions in comparison to styrene malic acid copolymer. This suggests the native nanodisc assembled using membrane scaffold protein would be ideal for the study of a large variety of membrane protein, particularly in functional studies where the surrounding lipid environment can affect the dynamics or behavior of the membrane protein of interest.

References

1. Lodish H, Berk A, Zipursky SL et al (2000) *Molecular cell biology*, 4th edn. W. H. Freeman, New York
2. Wallin E, Heijne GV (1998) Genome-wide analysis of integral membrane proteins from eubacterial, archaean, and eukaryotic organisms. *Protein Sci* 7:1029–1038. <https://doi.org/10.1002/pro.5560070420>
3. Krogh A, Larsson B, von Heijne G, Sonnhammer ELL (2001) Predicting transmembrane protein topology with a hidden markov model: application to complete genomes1. *J Mol Biol* 305:567–580. <https://doi.org/10.1006/jmbi.2000.4315>
4. Ahram M, Litou ZI, Fang R, Al-Tawallbeh G (2006) Estimation of membrane proteins in the human proteome. *In Silico Biol* 6:379–386
5. Daley DO, Rapp M, Granseth E et al (2005) Global topology analysis of the Escherichia coli inner membrane proteome. *Science* 308:1321–1323. <https://doi.org/10.1126/science.1109730>
6. Kim H, Melén K, Österberg M, von Heijne G (2006) A global topology map of the Saccharomyces cerevisiae membrane proteome. *Proc Natl Acad Sci* 103:11142–11147. <https://doi.org/10.1073/pnas.0604075103>
7. Bakheet TM, Doig AJ (2009) Properties and identification of human protein drug targets. *Bioinformatics* 25:451–457. <https://doi.org/10.1093/bioinformatics/btp002>
8. Overington JP, Al-Lazikani B, Hopkins AL (2006) How many drug targets are there? *Nat Rev Drug Discov* 5:993–996. <https://doi.org/10.1038/nrd2199>
9. Yıldırım MA, Goh K-I, Cusick ME et al (2007) Drug–target network. *Nat Biotechnol* 25:1119–1126. <https://doi.org/10.1038/nbt1338>
10. Henderson R, Unwin PNT (1975) Three-dimensional model of purple membrane obtained by electron microscopy. *Nature* 257:28–32. <https://doi.org/10.1038/257028a0>
11. Deisenhofer J, Epp O, Miki K et al (1985) Structure of the protein subunits in the photosynthetic reaction centre of Rhodospseudomonas viridis at 3[ångström] resolution. *Nature* 318:618–624. <https://doi.org/10.1038/318618a0>
12. Michel H (1982) Three-dimensional crystals of a membrane protein complex. *J Mol Biol* 158:567–572. [https://doi.org/10.1016/0022-2836\(82\)90216-9](https://doi.org/10.1016/0022-2836(82)90216-9)
13. White SH (2004) The progress of membrane protein structure determination. *Protein Sci* 13:1948–1949. <https://doi.org/10.1110/ps.04712004>
14. Almén MS, Nordström KJ, Fredriksson R, Schiöth HB (2009) Mapping the human membrane proteome: a majority of the human membrane proteins can be classified according

- to function and evolutionary origin. *BMC Biol* 7:50. <https://doi.org/10.1186/1741-7007-7-50>
15. Salom D, Palczewski K (2011) Structural biology of membrane proteins. In: Robinson AS (ed) *Production of membrane proteins*. Wiley-VCH Verlag GmbH & Co. KGaA, Weinheim, pp 249–273
 16. Fredriksson R, Lagerström MC, Lundin L-G, Schiöth HB (2003) The G-protein-coupled receptors in the human genome form five main families. Phylogenetic analysis, paralogon groups, and fingerprints. *Mol Pharmacol* 63:1256–1272. <https://doi.org/10.1124/mol.63.6.1256>
 17. Kobilka BK (2007) G protein coupled receptor structure and activation. *Biochim Biophys Acta BBA—Biomembr* 1768:794–807. <https://doi.org/10.1016/j.bbamem.2006.10.021>
 18. Okada T, Le Trong I, Fox BA et al (2000) X-ray diffraction analysis of three-dimensional crystals of bovine rhodopsin obtained from mixed micelles. *J Struct Biol* 130:73–80. <https://doi.org/10.1006/jjsbi.1999.4209>
 19. Okada T, Sugihara M, Bondar A-N et al (2004) The retinal conformation and its environment in rhodopsin in light of a new 2.2 Å crystal structure†. *J Mol Biol* 342:571–583. <https://doi.org/10.1016/j.jmb.2004.07.044>
 20. White SH (2009) Biophysical dissection of membrane proteins. *Nature* 459:344–346. <https://doi.org/10.1038/nature08142>
 21. Hanson MA, Stevens RC (2009) Discovery of new GPCR biology: one receptor structure at a time. *Structure* 17:8–14. <https://doi.org/10.1016/j.str.2008.12.003>
 22. Bowie JU (1999) Helix-bundle membrane protein fold templates. *Protein Sci* 8:2711–2719. <https://doi.org/10.1110/ps.8.12.2711>
 23. Dutzler R, Campbell EB, Cadene M et al (2002) X-ray structure of a CIC chloride channel at 3.0 [ångstr] reveals the molecular basis of anion selectivity. *Nature* 415:287–294. <https://doi.org/10.1038/415287a>
 24. Toyoshima C, Nomura H (2002) Structural changes in the calcium pump accompanying the dissociation of calcium. *Nature* 418:605–611. <https://doi.org/10.1038/nature00944>
 25. Olesen C, Sørensen TL-M, Nielsen RC et al (2004) Dephosphorylation of the calcium pump coupled to counterion occlusion. *Science* 306:2251–2255. <https://doi.org/10.1126/science.1106289>
 26. Manning G, Whyte DB, Martinez R et al (2002) The protein kinase complement of the human genome. *Science* 298:1912–1934. <https://doi.org/10.1126/science.1075762>
 27. Kandalepas PC, Vassar R (2012) Identification and biology of β -secretase: Identification and biology of β -secretase. *J Neurochem* 120:55–61. <https://doi.org/10.1111/j.1471-4159.2011.07512.x>
 28. Reiss K, Saftig P (2009) The “A Disintegrin And Metalloprotease” (ADAM) family of sheddases: physiological and cellular functions. *Semin Cell Dev Biol* 20:126–137. <https://doi.org/10.1016/j.semcdb.2008.11.002>
 29. Pahl MC, Askinazi OL, Hamilton C, et al (2001) Signalling via single-pass transmembrane proteins. In: eLS. John Wiley & Sons, Ltd
 30. Zvilning M, Kochva U, Arkin IT (2007) How important are transmembrane helices of bitopic membrane proteins? *Biochim Biophys Acta BBA—Biomembr* 1768:387–392. <https://doi.org/10.1016/j.bbamem.2006.11.019>
 31. Lemmon MA, Treutlein HR, Adams PD et al (1994) A dimerization motif for transmembrane α -helices. *Nat Struct Mol Biol* 1:157–163. <https://doi.org/10.1038/nsb0394-157>
 32. Arkin IT (2002) Structural aspects of oligomerization taking place between the transmembrane α -helices of bitopic membrane proteins. *Biochim Biophys Acta BBA—Biomembr* 1565:347–363. [https://doi.org/10.1016/S0005-2736\(02\)00580-1](https://doi.org/10.1016/S0005-2736(02)00580-1)
 33. Kleinschmidt JH (2005) Folding and stability of monomeric β -barrel membrane proteins. In: Tamm LK (ed) *Protein-lipid interactions*. Wiley-VCH Verlag GmbH & Co. KGaA, Weinheim, pp 27–56

34. Pautsch A, Schulz GE (2000) High-resolution structure of the OmpA membrane domain. *J Mol Biol* 298:273–282. <https://doi.org/10.1006/jmbi.2000.3671>
35. Ferguson AD, Hofmann E, Coulton JW et al (1998) Siderophore-mediated iron transport: crystal structure of FhuA with bound lipopolysaccharide. *Science* 282:2215–2220. <https://doi.org/10.1126/science.282.5397.2215>
36. Snijder HJ, Ubarretxena-Belandia I, Blaauw M et al (1999) Structural evidence for dimerization-regulated activation of an integral membrane phospholipase. *Nature* 401:717–721. <https://doi.org/10.1038/44890>
37. Cowan SW, Schirmer T, Rummel G et al (1992) Crystal structures explain functional properties of two *E. coli* porins. *Nature* 358:727–733. <https://doi.org/10.1038/358727a0>
38. Forst D, Welte W, Wacker T, Diederichs K (1998) Structure of the sucrose-specific porin ScrY from *Salmonella typhimurium* and its complex with sucrose. *Nat Struct Mol Biol* 5:37–46. <https://doi.org/10.1038/nsb0198-37>
39. Goñi FM (2002) Non-permanent proteins in membranes: when proteins come as visitors (Review). *Mol Membr Biol* 19:237–245. <https://doi.org/10.1080/0968768021000035078>
40. Whited AM, Johs A (2015) The interactions of peripheral membrane proteins with biological membranes. *Chem Phys Lipids* 192:51–59. <https://doi.org/10.1016/j.chemphyslip.2015.07.015>
41. Murray D, Honig B (2002) Electrostatic control of the membrane targeting of C2 domains. *Mol Cell* 9:145–154. [https://doi.org/10.1016/S1097-2765\(01\)00426-9](https://doi.org/10.1016/S1097-2765(01)00426-9)
42. Harel M, Aharoni A, Gaidukov L et al (2004) Structure and evolution of the serum paraoxonase family of detoxifying and anti-atherosclerotic enzymes. *Nat Struct Mol Biol* 11:412–419. <https://doi.org/10.1038/nsmb767>
43. Ames JB, Ishima R, Tanaka T et al (1997) Molecular mechanics of calcium–myristoyl switches. *Nature* 389:198–202. <https://doi.org/10.1038/38310>
44. Cho W, Stahelin RV (2005) Membrane-protein interactions in cell signaling and membrane trafficking. *Annu Rev Biophys Biomol Struct* 34:119–151. <https://doi.org/10.1146/annurev.biophys.33.110502.133337>
45. Smith EM, Macdonald PJ, Chen Y, Mueller JD (2014) Quantifying protein-protein interactions of peripheral membrane proteins by fluorescence brightness analysis. *Biophys J* 107:66–75. <https://doi.org/10.1016/j.bpj.2014.04.055>
46. Newby ZER, O’Connell JD, Gruswitz F et al (2009) A general protocol for the crystallization of membrane proteins for X-ray structural investigation. *Nat Protoc* 4:619–637. <https://doi.org/10.1038/nprot.2009.27>
47. Striegel AM (2005) Multiple detection in size-exclusion chromatography of macromolecules. *Anal Chem* 77:104 A–113 A. <https://doi.org/10.1021/ac053345e>
48. Nury H, Manon F, Arnou B et al (2008) Mitochondrial bovine ADP/ATP carrier in detergent is predominantly monomeric but also forms multimeric species. *Biochemistry (Mosc)* 47:12319–12331. <https://doi.org/10.1021/bi801053m>
49. Wei Y, Li H, Fu D (2004) Oligomeric state of the *Escherichia coli* metal transporter YiiP. *J Biol Chem* 279:39251–39259. <https://doi.org/10.1074/jbc.M407044200>
50. Riley ML, Wallace BA, Flitsch SL, Booth PJ (1997) Slow α helix formation during folding of a membrane protein. *Biochemistry (Mosc)* 36:192–196. <https://doi.org/10.1021/bi962199r>
51. Lórenz-Fonfría VA, Villaverde J, Trézéguet V et al (2003) Structural and functional implications of the instability of the ADP/ATP transporter purified from mitochondria as revealed by FTIR spectroscopy. *Biophys J* 85:255–266. [https://doi.org/10.1016/S0006-3495\(03\)74471-3](https://doi.org/10.1016/S0006-3495(03)74471-3)
52. Pascal AA, Caron L, Rousseau B et al (1998) Resonance Raman spectroscopy of a light-harvesting protein from the brown alga *Laminaria saccharina*. *Biochemistry (Mosc)* 37:2450–2457. <https://doi.org/10.1021/bi9719657>
53. Reyes N, Ginter C, Boudker O (2009) Transport mechanism of a bacterial homologue of glutamate transporters. *Nature* 462:880–885. <https://doi.org/10.1038/nature08616>

54. Junge F, Schneider B, Reckel S et al (2008) Large-scale production of functional membrane proteins. *Cell Mol Life Sci* 65:1729–1755. <https://doi.org/10.1007/s00018-008-8067-5>
55. Privé GG (2007) Detergents for the stabilization and crystallization of membrane proteins. *Methods* 41:388–397. <https://doi.org/10.1016/j.ymeth.2007.01.007>
56. Carpenter EP, Beis K, Cameron AD, Iwata S (2008) Overcoming the challenges of membrane protein crystallography. *Curr Opin Struct Biol* 18:581–586. <https://doi.org/10.1016/j.sbi.2008.07.001>
57. Pedersen BP, Buch-Pedersen MJ, Preben Morth J et al (2007) Crystal structure of the plasma membrane proton pump. *Nature* 450:1111–1114. <https://doi.org/10.1038/nature06417>
58. Long SB, Tao X, Campbell EB, MacKinnon R (2007) Atomic structure of a voltage-dependent K⁺ channel in a lipid membrane-like environment. *Nature* 450:376–382. <https://doi.org/10.1038/nature06265>
59. Cherezov V, Rosenbaum DM, Hanson MA et al (2007) High-resolution crystal structure of an engineered human β 2-adrenergic G protein-coupled receptor. *Science* 318:1258–1265. <https://doi.org/10.1126/science.1150577>
60. Adrian M, Dubochet J, Lepault J, McDowell AW (1984) Cryo-electron microscopy of viruses. *Nature* 308:32–36. <https://doi.org/10.1038/308032a0>
61. Mosser G (2001) Two-dimensional crystallography of transmembrane proteins. *Micron* 32:517–540. [https://doi.org/10.1016/S0968-4328\(00\)00047-0](https://doi.org/10.1016/S0968-4328(00)00047-0)
62. Luca S, Heise H, Baldus M (2003) High-resolution solid-state NMR applied to polypeptides and membrane proteins. *Acc Chem Res* 36:858–865. <https://doi.org/10.1021/ar020232y>
63. Ketchum RR, Hu W, Cross TA (1993) High-resolution conformation of gramicidin A in a lipid bilayer by solid-state NMR. *Science* 261:1457–1460. <https://doi.org/10.1126/science.7690158>
64. Andrew ER, Bradbury A, Eades RG (1958) NMR spectra from a crystal rotated at high speed. *Nat Lond* 182:1659
65. Garavito RM, Ferguson-Miller S (2001) Detergents as tools in membrane biochemistry. *J Biol Chem* 276:32403–32406. <https://doi.org/10.1074/jbc.R100031200>
66. le Maire M, Champeil P, Møller JV (2000) Interaction of membrane proteins and lipids with solubilizing detergents. *Biochim Biophys Acta BBA—Biomembr* 1508:86–111. [https://doi.org/10.1016/S0304-4157\(00\)00010-1](https://doi.org/10.1016/S0304-4157(00)00010-1)
67. Linke D (2009) Chapter 34 detergents: an overview. In: Deutscher RRB, MP (ed) *Methods in enzymology*. Academic Press, pp 603–617
68. Lin S-H, Guidotti G (2009) Chapter 35 Purification of Membrane Proteins. In: Deutscher RRB, MP (ed) *Methods in Enzymology*. Academic Press, pp 619–629
69. Newby ZER, O’Connell JD, Gruswitz F et al (2009) A general protocol for the crystallization of membrane proteins for X-ray structural investigation. *Nat Protoc* 4:619–637. <https://doi.org/10.1038/nprot.2009.27>
70. Seddon AM, Curnow P, Booth PJ (2004) Membrane proteins, lipids and detergents: not just a soap opera. *Biochim Biophys Acta BBA—Biomembr* 1666:105–117. <https://doi.org/10.1016/j.bbamem.2004.04.011>
71. Hunte C, Screpanti E, Venturi M et al (2005) Structure of a Na⁺/H⁺ antiporter and insights into mechanism of action and regulation by pH. *Nature* 435:1197–1202. <https://doi.org/10.1038/nature03692>
72. Lund S, Orlowski S, de Foresta B et al (1989) Detergent structure and associated lipid as determinants in the stabilization of solubilized Ca²⁺ -ATPase from sarcoplasmic reticulum. *J Biol Chem* 264:4907–4915
73. Gutmann DAP, Mizohata E, Newstead S et al (2007) A high-throughput method for membrane protein solubility screening: the ultracentrifugation dispersity sedimentation assay. *Protein Sci* 16:1422–1428. <https://doi.org/10.1110/ps.072759907>
74. Gautier A, Mott HR, Bostock MJ et al (2010) Structure determination of the seven-helix transmembrane receptor sensory rhodopsin II by solution NMR spectroscopy. *Nat Struct Mol Biol* 17:768–774. <https://doi.org/10.1038/nsmb.1807>

75. Tribet C, Audebert R, Popot J-L (1996) Amphipols: polymers that keep membrane proteins soluble in aqueous solutions. *Proc Natl Acad Sci* 93:15047–15050
76. Gorzelle BM, Hoffman AK, Keyes MH et al (2002) Amphipols can support the activity of a membrane enzyme. *J Am Chem Soc* 124:11594–11595. <https://doi.org/10.1021/ja027051b>
77. Mueller K (1981) Structural dimorphism of bile salt/lecithin mixed micelles. A possible regulatory mechanism for cholesterol solubility in bile? X-ray structural analysis. *Biochemistry (Mosc)* 20:404–414
78. Sanders CR, Landis GC (1995) Reconstitution of membrane proteins into lipid-rich bilayered mixed micelles for NMR studies. *Biochemistry (Mosc)* 34:4030–4040. <https://doi.org/10.1021/bi00012a022>
79. Prosser RS, Evanics F, Kitevski JL, Al-Abdul-Wahid MS (2006) Current applications of bicelles in NMR studies of membrane-associated amphiphiles and proteins. *Biochemistry (Mosc)* 45:8453–8465. <https://doi.org/10.1021/bi060615u>
80. Johansson LC, Wöhri AB, Katona G et al (2009) Membrane protein crystallization from lipidic phases. *Curr Opin Struct Biol* 19:372–378. <https://doi.org/10.1016/j.sbi.2009.05.006>
81. Loudet C, Khemtémourian L, Aussenac F et al (2005) Bicelle membranes and their use for hydrophobic peptide studies by circular dichroism and solid state NMR. *Biochim Biophys Acta BBA—Gen Subj* 1724:315–323. <https://doi.org/10.1016/j.bbagen.2005.04.026>
82. van Dam L, Karlsson G, Edwards K (2004) Direct observation and characterization of DMPC/DHPC aggregates under conditions relevant for biological solution NMR. *Biochim Biophys Acta BBA—Biomembr* 1664:241–256. <https://doi.org/10.1016/j.bbamem.2004.06.005>
83. Lau T-L, Partridge AW, Ginsberg MH, Ulmer TS (2008) Structure of the integrin β 3 transmembrane segment in phospholipid bicelles and detergent micelles. *Biochemistry (Mosc)* 47:4008–4016. <https://doi.org/10.1021/bi800107a>
84. Lindberg M, Biverstahl H, Gräslund A, Måler L (2003) Structure and positioning comparison of two variants of penetratin in two different membrane mimicking systems by NMR. *Eur J Biochem* 270:3055–3063. <https://doi.org/10.1046/j.1432-1033.2003.03685.x>
85. Poget SF, Girvin ME (2007) Solution NMR of membrane proteins in bilayer mimics: small is beautiful, but sometimes bigger is better. *Biochim Biophys Acta BBA—Biomembr* 1768:3098–3106. <https://doi.org/10.1016/j.bbamem.2007.09.006>
86. Kagawa Y, Racker E (1971) Partial Resolution of the enzymes catalyzing oxidative phosphorylation XXV. Reconstitution of vesicles catalyzing 32Pi—adenosine triphosphate exchange. *J Biol Chem* 246:5477–5487
87. Ramos-Franco J, Bare D, Caenepeel S et al (2000) Single-channel function of recombinant type 2 inositol 1,4,5-trisphosphate receptor. *Biophys J* 79:1388–1399. [https://doi.org/10.1016/S0006-3495\(00\)76391-0](https://doi.org/10.1016/S0006-3495(00)76391-0)
88. Wang L, Sigworth FJ (2009) Structure of the BK potassium channel in a lipid membrane from electron cryomicroscopy. *Nature* 461:292–295. <https://doi.org/10.1038/nature08291>
89. Wang L, Tonggu L (2015) Membrane protein reconstitution for functional and structural studies. *Sci China Life Sci* 58:66–74. <https://doi.org/10.1007/s11427-014-4769-0>
90. Young HS, Rigaud JL, Lacapère JJ et al (1997) How to make tubular crystals by reconstitution of detergent-solubilized Ca²⁺(+)-ATPase. *Biophys J* 72:2545–2558. [https://doi.org/10.1016/S0006-3495\(97\)78898-2](https://doi.org/10.1016/S0006-3495(97)78898-2)
91. Tonge SR, Tighe BJ (2001) Responsive hydrophobically associating polymers: a review of structure and properties. *Adv Drug Deliv Rev* 53:109–122. [https://doi.org/10.1016/S0169-409X\(01\)00223-X](https://doi.org/10.1016/S0169-409X(01)00223-X)
92. Knowles TJ, Finka R, Smith C et al (2009) Membrane proteins solubilized intact in lipid containing nanoparticles bounded by styrene maleic acid copolymer. *J Am Chem Soc* 131:7484–7485. <https://doi.org/10.1021/ja810046q>
93. Orwick-Rydmark M, Lovett JE, Graziadei A et al (2012) Detergent-free incorporation of a seven-transmembrane receptor protein into nanosized bilayer lipodisq particles for functional and biophysical studies. *Nano Lett* 12:4687–4692. <https://doi.org/10.1021/nl3020395>

94. Alfrey T, Lavin E (1945) The copolymerization of styrene and maleic anhydride. *J Am Chem Soc* 67:2044–2045. <https://doi.org/10.1021/ja01227a502>
95. Hill DJT, O'Donnell JH, O'Sullivan PW (1985) Analysis of the mechanism of copolymerization of styrene and maleic anhydride. *Macromolecules* 18:9–17. <https://doi.org/10.1021/ma00143a002>
96. Klumperman B (2010) Mechanistic considerations on styrene? Maleic anhydride copolymerization reactions. *Polym Chem* 1:558. <https://doi.org/10.1039/b9py00341j>
97. Yao Z, Li B-G, Wang W-J, Pan Z-R (1999) Continuous thermal bulk copolymerization of styrene and maleic anhydride. *J Appl Polym Sci* 73:615–622. [https://doi.org/10.1002/\(sici\)1097-4628\(19990801\)73:5<615::aid-app1>3.0.co;2-1](https://doi.org/10.1002/(sici)1097-4628(19990801)73:5<615::aid-app1>3.0.co;2-1)
98. Dörr JM, Scheidelaar S, Koorengevel MC et al (2016) The styrene–maleic acid copolymer: a versatile tool in membrane research. *Eur Biophys J* 45:3–21. <https://doi.org/10.1007/s00249-015-1093-y>
99. Lee SC, Knowles TJ, Postis VLG et al (2016) A method for detergent-free isolation of membrane proteins in their local lipid environment. *Nat Protoc* 11:1149–1162. <https://doi.org/10.1038/nprot.2016.070>
100. Scheidelaar S, Koorengevel M, Pardo J et al (2015) Molecular model for the solubilization of membranes into nanodisks by styrene maleic acid copolymers. *Biophys J* 108:279–290. <https://doi.org/10.1016/j.bpj.2014.11.3464>
101. Dörr JM, Koorengevel MC, Schäfer M, et al (2014) Detergent-free isolation, characterization, and functional reconstitution of a tetrameric K⁺ channel: the power of native nanodiscs. *Proc Natl Acad Sci* 111:18607–18612. <https://doi.org/10.1073/pnas.1416205112>
102. Long AR, O'Brien CC, Malhotra K et al (2013) A detergent-free strategy for the reconstitution of active enzyme complexes from native biological membranes into nanoscale discs. *BMC Biotechnol* 13:41
103. Smirnova IA, Sjöstrand D, Li F et al (2016) Isolation of yeast complex IV in native lipid nanodiscs. *Biochim Biophys Acta BBA—Biomembr* 1858:2984–2992. <https://doi.org/10.1016/j.bbamem.2016.09.004>
104. Jamshad M, Grimard V, Idini I et al (2015) Structural analysis of a nanoparticle containing a lipid bilayer used for detergent-free extraction of membrane proteins. *Nano Res* 8:774–789. <https://doi.org/10.1007/s12274-014-0560-6>
105. Gulati S, Jamshad M, Knowles TJ et al (2014) Detergent-free purification of ABC (ATP-binding-cassette) transporters. *Biochem J* 461:269–278. <https://doi.org/10.1042/BJ20131477>
106. Postis V, Rawson S, Mitchell JK et al (2015) The use of SMALPs as a novel membrane protein scaffold for structure study by negative stain electron microscopy. *Biochim Biophys Acta BBA—Biomembr* 1848:496–501. <https://doi.org/10.1016/j.bbamem.2014.10.018>
107. Jamshad M, Charlton J, Lin Y-P et al (2015) G-protein coupled receptor solubilization and purification for biophysical analysis and functional studies, in the total absence of detergent. *Biosci Rep* 35:e00188. <https://doi.org/10.1042/BSR20140171>
108. Dominguez Pardo JJ, Dörr JM, Iyer A et al (2017) Solubilization of lipids and lipid phases by the styrene–maleic acid copolymer. *Eur Biophys J* 46:91–101. <https://doi.org/10.1007/s00249-016-1181-7>
109. Sahu ID, McCarrick RM, Troxel KR et al (2013) DEER EPR measurements for membrane protein structures via bifunctional spin labels and lipidisq nanoparticles. *Biochemistry (Mosc)* 52:6627–6632. <https://doi.org/10.1021/bi4009984>
110. Prabudiansyah I, Kusters I, Caforio A, Driessen AJM (2015) Characterization of the annular lipid shell of the Sec translocon. *Biochim Biophys Acta BBA—Biomembr* 1848:2050–2056. <https://doi.org/10.1016/j.bbamem.2015.06.024>
111. Banerjee S, Pal TK, Guha SK (2012) Probing molecular interactions of poly (styrene-co-maleic acid) with lipid matrix models to interpret the therapeutic potential of the co-polymer. *Biochim Biophys Acta BBA—Biomembr* 1818:537–550. <https://doi.org/10.1016/j.bbamem.2011.12.010>

112. Huang Y, DiDonato JA, Levison BS et al (2014) An abundant dysfunctional apolipoprotein A1 in human atheroma. *Nat Med* 20:193–203. <https://doi.org/10.1038/nm.3459>
113. Lund-Katz S, Phillips MC (2010) High density lipoprotein structure–function and role in reverse cholesterol transport. In: Harris JR (ed) *Cholesterol binding and cholesterol transport proteins*. Springer Netherlands, pp 183–227
114. Silva RAGD, Huang R, Morris J et al (2008) Structure of apolipoprotein A-I in spherical high density lipoproteins of different sizes. *Proc Natl Acad Sci* 105:12176–12181. <https://doi.org/10.1073/pnas.0803626105>
115. Davidson WS, Thompson TB (2007) The Structure of apolipoprotein A-I in high density lipoproteins. *J Biol Chem* 282:22249–22253. <https://doi.org/10.1074/jbc.R700014200>
116. Huang R, Silva RAGD, Jerome WG et al (2011) Apolipoprotein A-I structural organization in high-density lipoproteins isolated from human plasma. *Nat Struct Mol Biol* 18:416–422. <https://doi.org/10.1038/nsmb.2028>
117. Phillips JC, Wriggers W, Li Z et al (1997) Predicting the structure of apolipoprotein A-I in reconstituted high-density lipoprotein disks. *Biophys J* 73:2337–2346. [https://doi.org/10.1016/S0006-3495\(97\)78264-X](https://doi.org/10.1016/S0006-3495(97)78264-X)
118. Bayburt TH, Grinkova YV, Sligar SG (2002) Self-assembly of discoidal phospholipid bilayer nanoparticles with membrane scaffold proteins. *Nano Lett* 2:853–856. <https://doi.org/10.1021/nl025623k>
119. Jonas A (1986) Reconstitution of high-density lipoproteins. *Methods Enzymol* 128:553–582
120. Denisov IG, Grinkova YV, Lazarides AA, Sligar SG (2004) Directed self-assembly of monodisperse phospholipid bilayer nanodiscs with controlled size. *J Am Chem Soc* 126:3477–3487. <https://doi.org/10.1021/ja0393574>
121. Klon AE, Segrest JP, Harvey SC (2002) Comparative models for human apolipoprotein A-I bound to lipid in discoidal high-density lipoprotein particles. *Biochemistry (Mosc)* 41:10895–10905. <https://doi.org/10.1021/bi020315m>
122. Denisov IG, Sligar SG (2016) Nanodiscs for structural and functional studies of membrane proteins. *Nat Struct Mol Biol* 23:481–486. <https://doi.org/10.1038/nsmb.3195>
123. Efremov RG, Leitner A, Aebersold R, Raunser S (2015) Architecture and conformational switch mechanism of the ryanodine receptor. *Nature* 517:39–43. <https://doi.org/10.1038/nature13916>
124. Frauenfeld J, Gumbart J, van der Sluis EO et al (2011) Cryo-EM structure of the ribosome–SecYE complex in the membrane environment. *Nat Struct Mol Biol* 18:614–621. <https://doi.org/10.1038/nsmb.2026>
125. Katayama H, Wang J, Tama F et al (2010) Three-dimensional structure of the anthrax toxin pore inserted into lipid nanodiscs and lipid vesicles. *Proc Natl Acad Sci* 107:3453–3457. <https://doi.org/10.1073/pnas.1000100107>
126. Yu T-Y, Raschle T, Hiller S, Wagner G (2012) Solution NMR spectroscopic characterization of human VDAC-2 in detergent micelles and lipid bilayer nanodiscs. *Biochim Biophys Acta BBA—Biomembr* 1818:1562–1569. <https://doi.org/10.1016/j.bbamem.2011.11.012>
127. Raschle T, Hiller S, Yu T-Y et al (2009) Structural and functional characterization of the integral membrane protein VDAC-1 in lipid bilayer nanodiscs. *J Am Chem Soc* 131:17777–17779. <https://doi.org/10.1021/ja907918r>
128. Shenkarev ZO, Lyukmanova EN, Solozhenkin OI et al (2009) Lipid-protein nanodiscs: possible application in high-resolution NMR investigations of membrane proteins and membrane-active peptides. *Biochemistry Mosc* 74:756–765. <https://doi.org/10.1134/S0006297909070086>
129. Shenkarev ZO, Lyukmanova EN, Paramonov AS et al (2010) Lipid-protein nanodiscs as reference medium in detergent screening for high-resolution NMR studies of integral membrane proteins. *J Am Chem Soc* 132:5628–5629. <https://doi.org/10.1021/ja9097498>
130. Morgado L, Zeth K, Burmann BM et al (2015) Characterization of the insertase BamA in three different membrane mimetics by solution NMR spectroscopy. *J Biomol NMR* 61:333–345. <https://doi.org/10.1007/s10858-015-9906-y>

131. Glück JM, Wittlich M, Feuerstein S et al (2009) Integral membrane proteins in nanodiscs can be studied by solution NMR spectroscopy. *J Am Chem Soc* 131:12060–12061. <https://doi.org/10.1021/ja904897p>
132. Hagn F, Eitzkorn M, Raschle T, Wagner G (2013) Optimized phospholipid bilayer nanodiscs facilitate high-resolution structure determination of membrane proteins. *J Am Chem Soc* 135:1919–1925. <https://doi.org/10.1021/ja310901f>
133. Davydov DR, Fernando H, Baas BJ et al (2005) Kinetics of dithionite-dependent reduction of cytochrome P450 3A4: heterogeneity of the enzyme caused by its oligomerization. *Biochemistry (Mosc)* 44:13902–13913. <https://doi.org/10.1021/bi0509346>
134. Baas BJ, Denisov IG, Sligar SG (2004) Homotropic cooperativity of monomeric cytochrome P450 3A4 in a nanoscale native bilayer environment. *Arch Biochem Biophys* 430:218–228. <https://doi.org/10.1016/j.abb.2004.07.003>
135. Bayburt TH, Vishnivetskii SA, McLean MA et al (2011) Monomeric rhodopsin is sufficient for normal rhodopsin kinase (GRK1) phosphorylation and arrestin-1 binding. *J Biol Chem* 286:1420–1428. <https://doi.org/10.1074/jbc.M110.151043>
136. Lanyi JK (1993) Proton translocation mechanism and energetics in the light-driven pump bacteriorhodopsin. *Biochim Biophys Acta BBA-Bioenerg* 1183:241–261
137. Huang KS, Bayley H, Liao M-J et al (1981) Refolding of an integral membrane protein. Denaturation, renaturation, and reconstitution of intact bacteriorhodopsin and two proteolytic fragments. *J Biol Chem* 256:3802–3809
138. Booth PJ, Flitsch SL, Stern LJ et al (1995) Intermediates in the folding of the membrane protein bacteriorhodopsin. *Nat Struct Mol Biol* 2:139–143. <https://doi.org/10.1038/nsb0295-139>
139. Bayburt TH, Grinkova YV, Sligar SG (2006) Assembly of single bacteriorhodopsin trimers in bilayer nanodiscs. *Arch Biochem Biophys* 450:215–222. <https://doi.org/10.1016/j.abb.2006.03.013>
140. Lanyi JK (2000) Molecular mechanism of ion transport in Bacteriorhodopsin: insights from crystallographic, spectroscopic, kinetic, and mutational studies. *J Phys Chem B* 104:11441–11448. <https://doi.org/10.1021/jp0023718>
141. Baudry J, Tajkhorshid E, Molnar F et al (2001) Molecular dynamics study of bacteriorhodopsin and the purple membrane. *J Phys Chem B* 105:905–918. <https://doi.org/10.1021/jp000898e>
142. Luecke H, Schobert B, Richter H-T et al (1999) Structure of bacteriorhodopsin at 1.55 Å resolution I. *J Mol Biol* 291:899–911. <https://doi.org/10.1006/jmbi.1999.3027>
143. Lemke H-D, Oesterhelt D (1981) Lysine 216 is a binding site of the retinyl moiety in bacteriorhodopsin. *FEBS Lett* 128:255–260. [https://doi.org/10.1016/0014-5793\(81\)80093-2](https://doi.org/10.1016/0014-5793(81)80093-2)
144. Oesterhelt D, Stoekenius W (1971) Rhodopsin-like protein from the purple membrane of halobacterium halobium. *Nature* 233:149–152. <https://doi.org/10.1038/10.1038/newbio233149a0>
145. Stoekenius W, Rowen R (1967) A morphological study of halobacterium halobium and its lysis in media of low salt concentration. *J Cell Biol* 34:365–393. <https://doi.org/10.1083/jcb.34.1.365>
146. Oesterhelt D, Stoekenius W (1973) Functions of a new photoreceptor membrane. *Proc Natl Acad Sci* 70:2853–2857
147. Turner J, El-Sayed MA (1985) Time-resolved resonance Raman spectroscopy of photobiological and photochemical transients. *Acc Chem Res* 18:331–338
148. Rothschild KJ, Zagaeski M, Cantore WA (1981) Conformational changes of bacteriorhodopsin detected by Fourier transform infrared difference spectroscopy. *Biochem Biophys Res Commun* 103:483–489. [https://doi.org/10.1016/0006-291X\(81\)90478-2](https://doi.org/10.1016/0006-291X(81)90478-2)
149. Hackett NR, Stern LJ, Chao BH et al (1987) Structure-function studies on bacteriorhodopsin. V. Effects of amino acid substitutions in the putative helix F. *J Biol Chem* 262:9277–9284
150. Hoffmann M, Wanko M, Strodel P et al (2006) Color tuning in rhodopsins: the mechanism for the spectral shift between bacteriorhodopsin and sensory rhodopsin II. *J Am Chem Soc* 128:10808–10818. <https://doi.org/10.1021/ja062082i>

151. Lanyi JK (2006) Proton transfers in the bacteriorhodopsin photocycle. *Biochim Biophys Acta BBA—Bioenerg* 1757:1012–1018. <https://doi.org/10.1016/j.bbabi.2005.11.003>
152. Sharkov AV, Pakulev AV, Chekalin SV, Matveetz YA (1985) Primary events in bacteriorhodopsin probed by subpicosecond spectroscopy. *Biochim Biophys Acta BBA—Bioenerg* 808:94–102. [https://doi.org/10.1016/0005-2728\(85\)90031-3](https://doi.org/10.1016/0005-2728(85)90031-3)
153. Lanyi JK (2004) Bacteriorhodopsin. *Annu Rev Physiol* 66:665–688. <https://doi.org/10.1146/annurev.physiol.66.032102.150049>
154. Zimanyi L, Varo G, Chang M et al (1992) Pathways of proton release in the bacteriorhodopsin photocycle. *Biochemistry (Mosc)* 31:8535–8543
155. Morgan JE, Vakkasoglu AS, Lanyi JK et al (2010) Coordinating the structural rearrangements associated with unidirectional proton transfer in the bacteriorhodopsin photocycle induced by deprotonation of the proton-release group: a time-resolved difference FTIR spectroscopic study. *Biochemistry (Mosc)* 49:3273–3281. <https://doi.org/10.1021/bi901757y>
156. Phatak P, Ghosh N, Yu H et al (2008) Amino acids with an intermolecular proton bond as proton storage site in bacteriorhodopsin. *Proc Natl Acad Sci* 105:19672–19677. <https://doi.org/10.1073/pnas.0810712105>
157. Gerwert K, Souvignier G, Hess B (1990) Simultaneous monitoring of light-induced changes in protein side-group protonation, chromophore isomerization, and backbone motion of bacteriorhodopsin by time-resolved Fourier-transform infrared spectroscopy. *Proc Natl Acad Sci* 87:9774–9778
158. Smith SO, Pardo JA, Mulder PPJ et al (1983) Chromophore structure in bacteriorhodopsin's O640 photointermediate. *Biochemistry (Mosc)* 22:6141–6148. <https://doi.org/10.1021/bi00295a016>
159. Riesle J, Oesterhelt D, Dencher NA, Heberle J (1996) D38 is an essential part of the proton translocation pathway in bacteriorhodopsin. *Biochemistry (Mosc)* 35:6635–6643. <https://doi.org/10.1021/bi9600456>
160. Richter H-T, Needleman R, Kandori H et al (1996) Relationship of retinal configuration and internal proton transfer at the end of the bacteriorhodopsin photocycle. *Biochemistry (Mosc)* 35:15461–15466. <https://doi.org/10.1021/bi9612430>
161. Blaurock AE, Stoeckenius W (1971) Structure of the purple membrane. *Nature* 233:152–155. <https://doi.org/10.1038/10.1038/newbio233152a0>
162. Cartailier J-P, Luecke H (2003) X-ray crystallographic analysis of lipid-protein interactions in the bacteriorhodopsin purple membrane. *Annu Rev Biophys Biomol Struct* 32:285–310. <https://doi.org/10.1146/annurev.biophys.32.110601.142516>
163. Corcelli A, Lattanzio VMT, Mascolo G et al (2002) Lipid-protein stoichiometries in a crystalline biological membrane: NMR quantitative analysis of the lipid extract of the purple membrane. *J Lipid Res* 43:132–140
164. Reynolds JA, Stoeckenius W (1977) Molecular weight of bacteriorhodopsin solubilized in Triton X-100. *Proc Natl Acad Sci* 74:2803–2804
165. Sternberg B, L'Hostis C, Whiteway CA, Watts A (1992) The essential role of specific *Halobacterium halobium* polar lipids in 2D-array formation of bacteriorhodopsin. *Biochim Biophys Acta BBA—Biomembr* 1108:21–30. [https://doi.org/10.1016/0005-2736\(92\)90110-8](https://doi.org/10.1016/0005-2736(92)90110-8)
166. Heberle J, Riesle J, Thiedemann G et al (1994) Proton migration along the membrane surface and retarded surface to bulk transfer. *Nature* 370:379–382. <https://doi.org/10.1038/370379a0>
167. Mukhopadhyay AK, Bose S, Hendler RW (1994) Membrane-mediated control of the bacteriorhodopsin photocycle. *Biochemistry (Mosc)* 33:10889–10895
168. Joshi MK, Dracheva S, Mukhopadhyay AK et al (1998) Importance of specific native lipids in controlling the photocycle of bacteriorhodopsin. *Biochemistry (Mosc)* 37:14463–14470. <https://doi.org/10.1021/bi980965j>
169. Dracheva S, Bose S, Hendler RW (1996) Chemical and functional studies on the importance of purple membrane lipids in bacteriorhodopsin photocycle behavior. *FEBS Lett* 382:209–212. [https://doi.org/10.1016/0014-5793\(96\)00181-0](https://doi.org/10.1016/0014-5793(96)00181-0)

170. Sugiyama Y, Yamada N, Mukohata Y (1994) The light-driven proton pump, cruxrhodopsin-2 in *Haloarcula* sp. arg-2 (bR+, hR-), and its coupled ATP formation. *Biochim Biophys Acta BBA—Bioenerg* 1188:287–292. [https://doi.org/10.1016/0005-2728\(94\)90047-7](https://doi.org/10.1016/0005-2728(94)90047-7)
171. Sugiyama Y, Maeda M, Futai M, Mukohata Y (1989) Isolation of a gene that encodes a new retinal protein, archaerhodopsin, from *Halobacterium* sp. aus-1. *J Biol Chem* 264:20859–20862
172. Balashov SP, Imasheva ES, Boichenko VA et al (2005) Xanthorhodopsin: a proton pump with a light-harvesting carotenoid antenna. *Science* 309:2061–2064. <https://doi.org/10.1126/science.1118046>
173. DeLong EF, Bèjà O (2010) The light-driven proton pump proteorhodopsin enhances bacterial survival during tough times. *PLoS Biol* 8:e1000359. <https://doi.org/10.1371/journal.pbio.1000359>
174. Tsai F-K, Fu H-Y, Yang C-S, Chu L-K (2014) Photochemistry of a dual-bacteriorhodopsin system in *Haloarcula marismortui*: HmbRI and HmbRII. *J Phys Chem B* 118:7290–7301. <https://doi.org/10.1021/jp503629v>
175. Sineshchekov OA, Jung K-H, Spudich JL (2002) Two rhodopsins mediate phototaxis to low-and high-intensity light in *Chlamydomonas reinhardtii*. *Proc Natl Acad Sci* 99:8689–8694
176. Baliga NS, Bonneau R, Facciotti MT et al (2004) Genome sequence of *Haloarcula marismortui*: A halophilic archaeon from the Dead Sea. *Genome Res* 14:2221–2234. <https://doi.org/10.1101/gr.2700304>
177. Fu H-Y, Lin Y-C, Chang Y-N et al (2010) A novel six-rhodopsin system in a single Archaeon. *J Bacteriol* 192:5866–5873. <https://doi.org/10.1128/JB.00642-10>
178. Fu H-Y, Yi H-P, Lu Y-H, Yang C-S (2013) Insight into a single halobacterium using a dual-bacteriorhodopsin system with different functionally optimized pH ranges to cope with periplasmic pH changes associated with continuous light illumination. *Mol Microbiol* 88:551–561. <https://doi.org/10.1111/mmi.12208>
179. Hsu M-F, Yu T-F, Chou C-C et al (2013) Using *Haloarcula marismortui* bacteriorhodopsin as a fusion tag for enhancing and visible expression of integral membrane proteins in *Escherichia coli*. *PLoS One* 8:e56363. <https://doi.org/10.1371/journal.pone.0056363>
180. Shevchenko V, Gushchin I, Polovinkin V et al (2014) Crystal structure of *Escherichia coli*-expressed *Haloarcula marismortui* bacteriorhodopsin I in the trimeric form. *PLoS One* 9:e112873. <https://doi.org/10.1371/journal.pone.0112873>
181. Luecke H, Schobert B, Richter H-T et al (1999) Structural changes in bacteriorhodopsin during ion transport at 2 Ångstrom resolution. *Science* 286:255–260. <https://doi.org/10.1126/science.286.5438.255>
182. von Heijne G (2006) Membrane-protein topology. *Nat Rev Mol Cell Biol* 7(12):909–918
183. Bayburt TH, Sliagar SG (2010) Membrane protein assembly into Nanodiscs. *FEBS Letters* 584(9):1721–1727
184. Baudry J, Tajkhorshid E, Molnar F et al (2001) Molecular Dynamics Study of Bacteriorhodopsin and the Purple Membrane. *J Phys Chem A* 105(5):905–918

Chapter 2

Experimental Background



2.1 Chromatography Methods

Chromatography methods are used extensively for protein and biomolecule purification or sample characterization. The biomolecules are separated according to the different specific properties of the chromatography methods, with some of the common methods illustrated in Fig. 2.1. Common chromatography methods include hydrophobic interaction chromatography, which separates biomolecules based on the reverse absorption depending on the differences in hydrophobicity. Affinity chromatography, on the other hand, separates biomolecules depending on the specific interaction, for example antibody, enzymes and ligands. This section introduces the chromatography methods used in the study of the different properties of nanodisc and their effects on the embedded membrane proteins.

2.1.1 Size Exclusion Chromatography

Also known as gel filtration chromatography in aqueous solution, size exclusion chromatography (SEC) is a chromatography method in which the sample is separated by size. The separation size is based on the difference in hydrodynamic volume, which for most globular proteins is directly related to molecular weight. Unlike the other common chromatography methods in Fig. 2.1 size exclusion chromatography separates protein without the sample binding to the column resin, giving flexibility over the buffer composition. This also means that size exclusion is suitable for proteins or biomolecules that are sensitive to pH changes, metal ions and does not have specific binding partners. With this flexibility over buffer conditions, size exclusion is often coupled with other chromatography methods since the buffer composition would not significantly affect the final separation.

The separation using size exclusion chromatography is achieved by the pores of gel beads packed in the size exclusion chromatography column. The pores in the

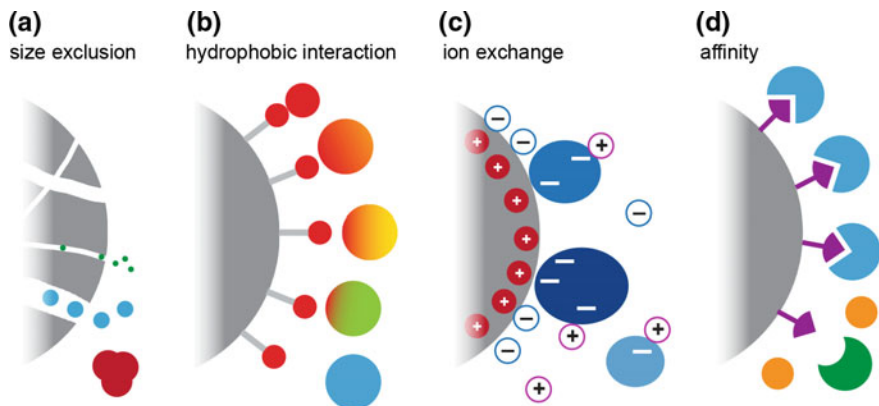


Fig. 2.1 Schematic diagrams showing the common chromatography methods and their separation principles: **a** size exclusion, **b** hydrophobic interaction, **c** ion exchange and **d** biorecognition affinity chromatography

beads make up the stationary phases that trap smaller molecules as the sample passes. The separation is based on the different permeation rate of each solute molecule into the interior of the pores. Shown in Fig. 2.2a, the differently sized molecules propagate through the size exclusion medium at different speeds. Smaller molecules enter the pores, travelling and exploring all the spaces within the matrix

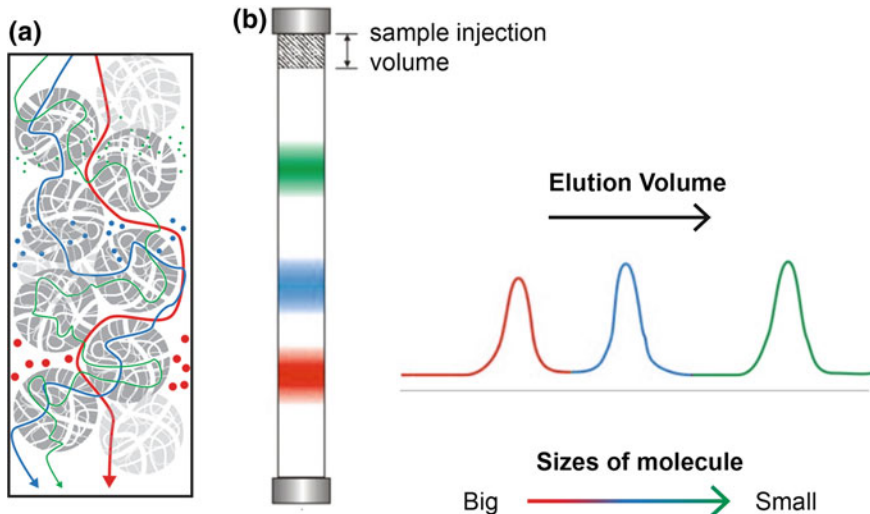


Fig. 2.2 Schematic diagrams of size exclusion chromatography. **a** The different pathlengths travelled by particles of different sizes, with the largest particle travelling only in the excluded volume between particles (red) and the smallest particles travelling through the pores within the inner space of the matrix (green). **b** The different sizes molecules travelling through the size exclusion chromatography columns at different times with the same flow rate, resulting in different elution volumes

before eluting from the column. Larger molecules, however, cannot enter the pores and are thus excluded from the inner pore space, and can only travel through the inter particle space. This implies that the larger molecules would have a smaller volume to travel through compared to the smaller molecules, hence eluting from the column faster than the smaller molecules under the same flow rate.

Each size exclusion chromatography column has a range of molecular sizes that it can separate, where if the molecules are bigger than this range they would elute in the void volume (V_0), and if smaller, the molecules would travel through the column together at the end of the total column volume. Void volume is the elution volume of molecules that are excluded from the size exclusion medium, in other words void volume is the volume of the mobile phase. If the size exclusion column is well packed, this volume is roughly 30% of the total column volume (V_t). The resolution of protein separation can be influenced by many factors, most of which are the physical properties of the column, such as column volume and dimensions, particle medium and sizes, packing density and pore sizes. Others factors such as loading volume, buffer viscosity and flow rate can be moderated during sample preparation in order to improve resolution and reduce peak broadening due to low separation efficiency. In addition to purification and fractionation of biomolecules based on size, size exclusion chromatography can also separate small molecules such as excess salt from the large biomolecules, serving as a quick and simple way for desalting or buffer exchange.

Size exclusion chromatography columns have the ability of size calibration within the separation range of the column. This can be achieved by plotting the selectivity curve with the partition coefficient, K_{av} as a function of log of molecular weight of a set of standard samples. The partition coefficient of a sample can be calculated with the elution volume of the sample V_e , the void volume V_0 and the total column volume V_t .

$$K_{av} = \frac{(V_e - V_0)}{(V_t - V_0)} \quad (2.1)$$

$(V_t - V_0)$ approximates the volume of stationary phase, and includes the volume of the materials that makes up the matrix. Although this suggests that the K_{av} determined using the Eq. 2.1 is not the true partition function, the volume of the solid material is constant and independent of the sample molecule and concentration. Therefore K_{av} determined using the Eq. 2.1 defines sample properties independent of the column packing or dimensions. Under normal circumstances K_{av} determined using the Eq. 2.1 should be between 0 and 1. If K_{av} is greater than 1 ($V_e > V_t$) it suggests that the molecules have non-specific binding to the matrix of the column and the elution volume is no longer dependent on the size of the molecules. On the other hand, if K_{av} is smaller than 0 ($V_e < V_0$), it suggests the previously determined void volume is no longer correct, likely caused by gaps or gas in the size exclusion chromatography column and the column should therefore be repacked. The selectivity curve is usually reasonably linear within the range $K_{av} = 0.1$ and 0.7 [1], providing the relationship,

$$K_{av} = a + b \log(MW) \quad (2.2)$$

Which can be used to estimate the molecular weight of samples based on the elution volume. Figure 2.3a shows the size exclusion profiles of size calibration using some

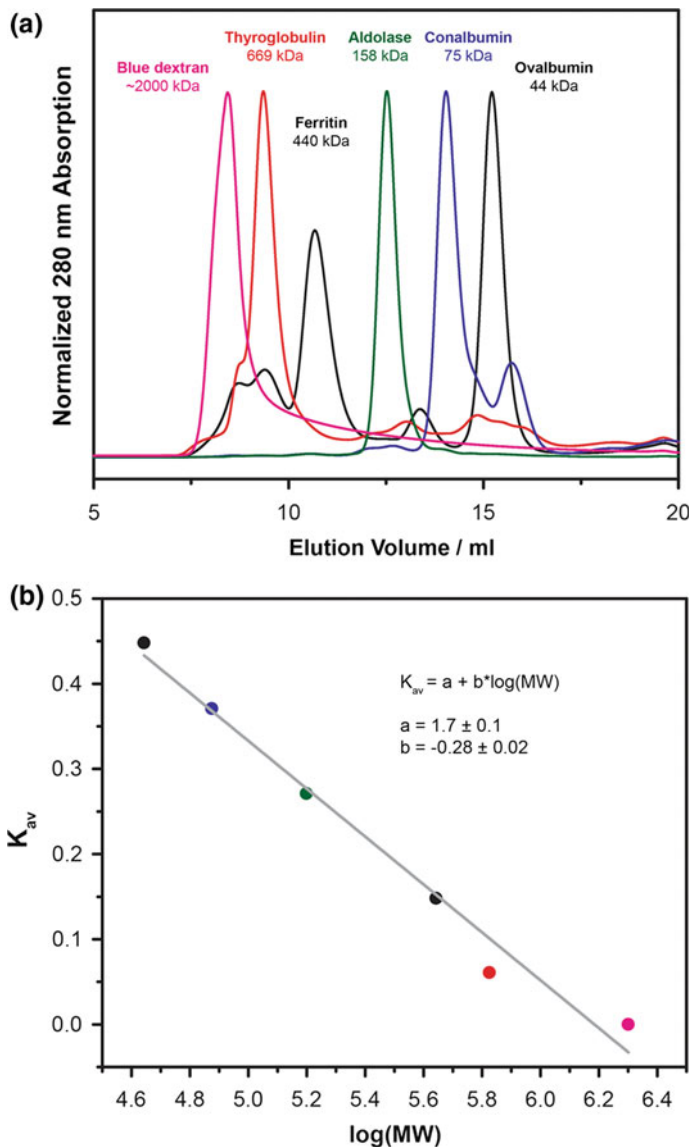


Fig. 2.3 Size exclusion chromatography profiles for size calibration of Superdex 200 Increase 10/300 GL (GE Healthcare) (a) and the selectivity curve from the size exclusion profiles (b). K_{av} values were calculated using Eq. 2.1, with the elution volume of blue dextran as the void volume

of the common standards, with each of the peak's elution volume translating to a point on the selectivity curve shown in Fig. 2.3b. The estimated molecular weight of the sample can be used as a guideline, since the estimation is based on the assumption of globular protein.

2.1.2 Ionic Exchange Chromatography

Ionic exchange chromatography is a chromatography method that separates the sample, in particular ionic or polar molecules, based on their electrostatic affinity to the oppositely charged ion exchanger. This interaction is strongly influenced by the overall charge, but also the charge density and the surface charge distribution. For biological samples, the charge is also dependent on the pH due to the composition of many amino acids containing weak basic or acidic groups. The surface charge of the protein can also be affected by the structure of the protein and the chemical environment. Since each protein has a unique isoelectric point (pI) based on its amino acid composition and structure, ionic exchange chromatography can separate the sample by its unique relationship between the surface charge and pH.

There are different types of ionic exchange chromatography and their use is dependent on the strength and the charge of the desired sample. Anionic exchange chromatography utilizes a positively charged medium to bind to the negatively charged protein, whereas cationic exchange chromatography contains a negatively charged medium to bind with the positively charged sample. After the sample is applied onto the ionic exchange chromatography column it binds with the medium contained in the column, shown in Fig. 2.4a. The sample can be eluted out of the column using either an increase of ionic strength, such as an increasing salt gradient, or by changing the pH that adjusts the surface charges of the protein. Shown in Fig. 2.4b is the elution profile of a typical anionic exchange chromatography where the samples were eluted out with different concentrations of NaCl. As the amount of salt ions present increases, the ions compete with the bound molecules to bind with the ionic exchange medium and eventually lead to the bound molecule eluting from the medium and being washed out of the column. The sample with the weakest surface charge would be eluted out first, with the lowest required salt concentration. Conversely, molecules with the strongest surface charge would require a higher salt concentration in order to be eluted from the column, and the higher the surface charge the higher ionic strength necessary for sample elution. By introducing a gradual change of ionic strength, typically a gradient or steps of increasing salt concentration, samples with different surface charges can be eluted out from the column at different times in a concentrated manner.

While size exclusion chromatography introduced in Sect. 2.1.1 has flexibility over the running buffer conditions due to the nature of the separation achieved, the buffer conditions for ionic exchange must be carefully designed to achieve the optimum separation. As discussed earlier in the section, the binding affinity of the sample to the ion exchange medium is dependent not only on the ionic strength of

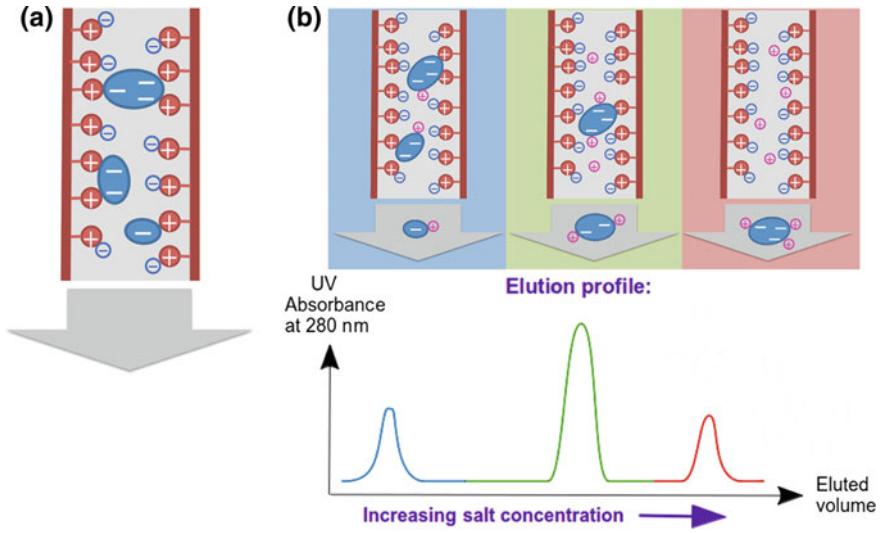


Fig. 2.4 Schematics of anionic exchange chromatography. As the sample passes through the column in low salt buffer (a), the protein will bind to the oppositely charged resin packed in the column and the protein sample is eluted out of the column at different elution volumes with different salt concentration (b)

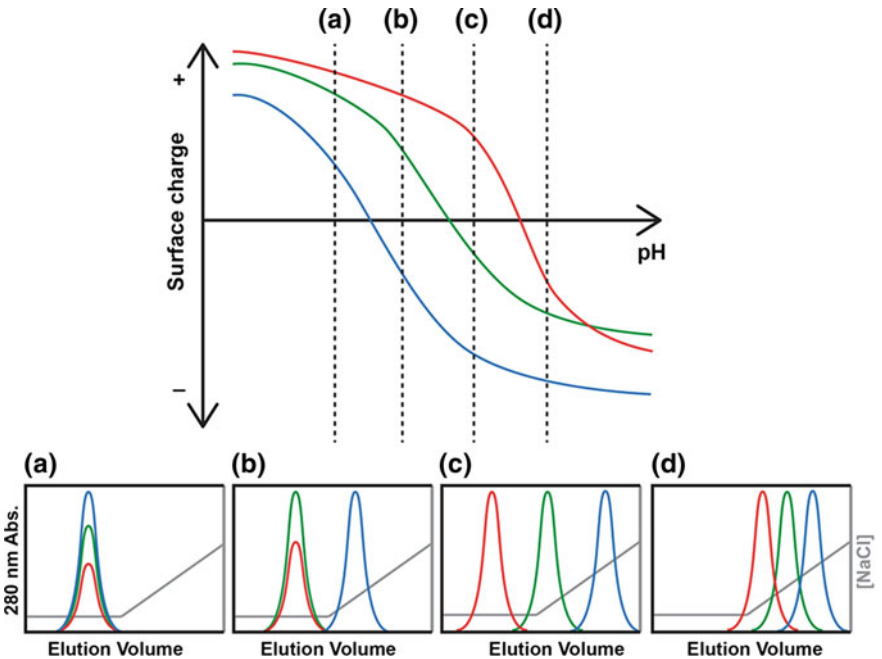


Fig. 2.5 schematic diagram illustrating the effect of pH on the binding and the elution of proteins using anionic exchange chromatography, where three different proteins and their elution pattern is represented by red, green and blue, and the gradient of increasing NaCl concentration is shown in grey

the elution buffers but also on the pH. Figure 2.5 illustrates the significance of pH in the selectivity of proteins using anionic exchange chromatography and the same NaCl concentration gradient. However, because the buffer conditions and the elution gradient can be adjusted according to the charge properties of the sample, ionic exchange offers a greater versatility as one can tailor the buffer conditions for a specific purpose. Furthermore, since separation using ionic exchange chromatography is achieved based on the difference in charge, ionic exchange chromatography can be used to qualitatively characterize the changes in surface charge.

2.2 Circular Dichroism Spectroscopy

Circular dichroism (CD) spectroscopy is an absorption spectroscopy that measures the difference between absorbance of the right and left circularly polarized light. Light is circularly polarized with the direction of the electric field rotating around the propagation axis, while the magnitude remains constant. When the circularly polarized light travels through matter that is optically active and chiral, the right rotating and left rotating polarized light interacts with the matter differently, resulting in circular dichroism. Most biomolecules are chiral, just as most of the common amino acids are chiral. Chirality can be conformational as well as structural, such in the cases of secondary structures. The high chirality of biomolecules allows circular dichroism spectroscopy to be a popular and useful spectroscopic technique in the field of biophysical characterization.

By definition, the difference in absorbance between the left and the right circularly polarized light can be expressed as

$$\Delta A(\lambda) = A_L(\lambda) - A_R(\lambda) \quad (2.3)$$

where ΔA is a function of wavelength. By applying Beer's law, Eq. 2.3 becomes

$$\Delta A(\lambda) = [\varepsilon_L(\lambda) - \varepsilon_R(\lambda)] \cdot d \cdot C \quad (2.4)$$

where $\varepsilon(\lambda)$ is the molar extinction coefficient with the unit $\text{cm}^{-1}\text{M}^{-1}$, d is the path length of the sample in cm and C is the molarity of the sample in M. The ellipticity, θ , of the polarization is defined as

$$\tan \theta = \frac{E_R - E_L}{E_R + E_L} \quad (2.5)$$

where E_R and E_L are the electric field vectors of the right and left circularly polarized light, respectively. When E_R and E_L have the same magnitude, θ is 0 and the light is linearly polarized. Due to the magnitude of circular dichroism being small, small angle approximation can be applied onto $\tan\theta$. By equating the

relationship between electric field vector E and intensity of light I , where $I = E^2$, Eq. 2.5 becomes

$$\tan \theta \approx \theta \text{ (radians)} = \frac{I_R^{1/2} - I_L^{1/2}}{I_R^{1/2} + I_L^{1/2}} \quad (2.6)$$

By applying Beer's law, Eq. 2.6 becomes

$$\theta = \frac{e^{-\frac{A_R \ln 10}{2}} - e^{-\frac{A_L \ln 10}{2}}}{e^{-\frac{A_R \ln 10}{2}} + e^{-\frac{A_L \ln 10}{2}}} \quad (2.7)$$

By substituting Eq. 2.7 with Eq. 2.4,

$$\theta = \frac{e^{\frac{\Delta A \ln 10}{2}} - 1}{e^{\frac{\Delta A \ln 10}{2}} + 1} \quad (2.8)$$

Since ΔA is $\ll 1$, the exponentials in Eq. 2.8 can be approximating using Taylor expansion to the first order. Together with conversion from radians into degrees,

$$\begin{aligned} \theta(\text{degrees}) &= \Delta A \left(\frac{\ln 10}{4} \right) \left(\frac{180}{\pi} \right) \\ &= 32.98 \cdot \Delta A \end{aligned} \quad (2.9)$$

Finally, by applying Eq. 2.4 and removing the dependence of concentration of the sample and path length, the molar ellipticity can be defined as

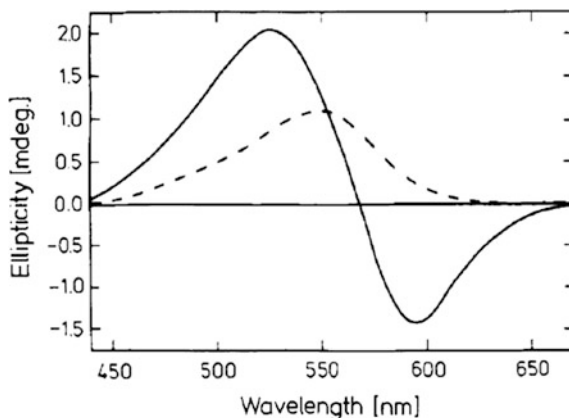
$$[\theta] = \frac{100\theta}{Cd} = 3298(\varepsilon_L - \varepsilon_R) \quad (2.10)$$

The unit of molar ellipticity is $\text{deg cm}^2 \text{ dmol}$. For proteins, the circular dichroism between the short wavelength ranges from 180 to 350 nm can often be used to determine secondary structure, as α helix, β sheets and random loops have distinct patterns in circular dichroism spectrum of that range.

Other than determining the secondary structure of protein, circular dichroism has been utilized to elucidate the oligomeric state of bacteriorhodopsin. Demonstrated first by Heyn et al., the visible wavelength circular dichroism spectra within the range between 400 and 700 nm exhibited a biphasic feature for purple membrane. The biphasic couplet contains a positive peak at a wavelength shorter than 567 nm and a negative peak at a wavelength longer than 567 nm. They found that the couplet was decreased and shifted into a monophasic positive peak when Triton X-100 was added to solubilize the purple membrane, suggesting the biphasic couplet was influenced by the integrity of the trimeric conformation.

Shown in Fig. 2.6 is a visible wavelength CD spectrum comparing the different features of monomeric and trimeric bacteriorhodopsin [2]. Further studied by

Fig. 2.6 Visible wavelength CD spectra of bacteriorhodopsin in DMPC vesicles, trimeric bacteriorhodopsin at 0.6 °C (solid) and monomeric bacteriorhodopsin when temperature is raised to 35.0 °C (dashed). Reprint with permission from Ref. [2]. Copyright 1981 American Chemical Society



Becher and Ebrey [3], the singularly positive peak was found to be caused by attachment of the retinal to the protein, whereas positive and negative couplet relates the interaction of chromophores between separate proteins. The inter-protein interaction was recognized as exciton coupling. A recent study done by Pescitelli and Woody looked closer at the origin of the doublet of PM in visible wavelength CD spectrum using theoretical calculations, and found that the CD spectrum was dominated by exciton interaction [4]. Furthermore, they showed that not only is the CD spectrum influenced by intra-trimeric interaction but also inter-trimeric interaction.

2.3 Transient Absorption Spectroscopy

2.3.1 Principles

Transient absorption spectroscopy is a time resolved spectroscopy that can measure the changes in absorbance or transmittance in the sample. The basic set up and principle is illustrated in Fig. 2.7. The sample is placed in front of a continuous wave light source, and is excited by a pulsed laser to initiate the reaction. During the reaction the changes in absorbance are measured with respect to time, providing

$$\Delta\text{Abs}(\lambda, t) = \log \frac{I_0(\lambda)}{I(\lambda, t)} \quad (2.11)$$

where λ is a particular wavelength. For bacteriorhodopsin at a fixed wavelength of light, ΔAbs corresponds to a change in intermediate states due to the progression of the photocycle. The negative ΔAbs observed for the parent state and its recovery to zero represents the initiation and the completion of a single photocycle, respectively. The positive rise of ΔAbs and its decay, on the other hand, corresponds to

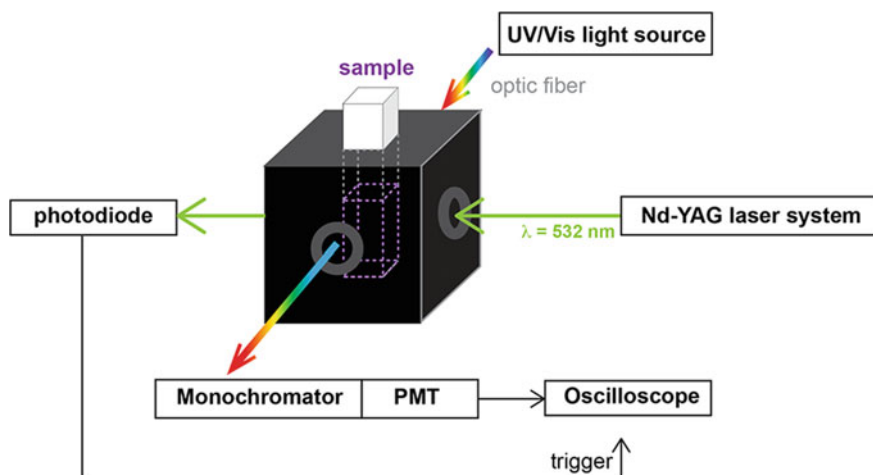


Fig. 2.7 Schematics of transient absorption spectroscopy experiment setup. The sample was excited with pulsed laser at 532 nm. Perpendicular to the excitation laser was an UV/Vis light source which passed through the sample and the transmitted light entered a monochromator to select observing wavelength. The final time-resolved results were displayed and recorded on the oscilloscope. The oscilloscope was triggered by the photodiode

the formation and the transition from the intermediate state. The transient absorption spectroscopy result can provide information of photocycle duration, pathway and individual intermediate lifetime, which can be used to analyze photocycle kinetics of bacteriorhodopsin in a given environment.

2.3.2 Experimental Setup

The time-resolved absorption spectroscopy experiment set up is shown in Fig. 2.8. The experimental set up can be grouped into 3 categories: the pulsed laser excitation, the sample set up and the data acquisition. The pulsed Q-switched laser excitation, highlighted in orange in Fig. 2.8, is generated by neodymium-doped yttrium aluminum garnet (Nd:YAG) system LS-2134UTF (Lotis Tii), on the second harmonic (SH) mode to provide a laser at 532 nm. The laser pulse then enters a series of lenses before reaching to the sample. A mechanical shutter VS25S2T2 (Uniblitz) monitors the repetition frequency of the laser pulse slower than 1 Hz. The beam is then split into two, one continues to travel towards the sample and the other towards the power detector in order to monitor the power of the laser. Finally the laser passes through a set of neutral density lenses to monitor the intensity of the beam, before entering the sample cell to excite and initiate bacteriorhodopsin photocycle.

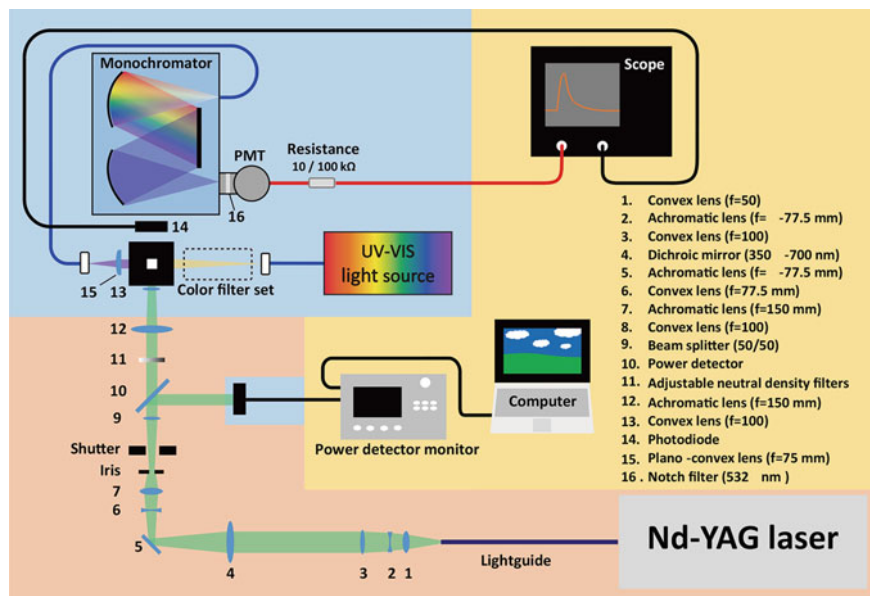


Fig. 2.8 Experimental set up of single wavelength transient absorption spectroscopy, where the set up can be separated into 3 categories: pulsed laser excitation (orange), probing sample (blue) and data acquisition (yellow)

The blue region shown in Fig. 2.8 illustrates the sample and probing set up. As described in Fig. 2.7, the sample was placed in the holder where it was excited by a pulsed laser. The sample temperature was monitored with qpod® (Quantum Northwest). The pulsed laser also initiated trigger through the photodiode. Perpendicular to the pulsed laser was the probing continuous wave (CW) light generated by UV/Vis light source DH2000 (Ocean Optics). To avoid the CW light source interfering with the photocycle initiated by the pulsed laser, the intensity of CW light source was monitored to be below 10% of the pulsed laser. As the excitation pulsed laser initiated the photocycle of bacteriorhodopsin, the changes in intermediate state caused a change in the absorbance in certain wavelengths. To investigate the changes in absorbance of a particular wavelength, the CW light transmitted through the sample would go towards Model 218 monochromator (McPherson), where a single wavelength was selected. The selected wavelength passed through a final lens to filter the scattered laser at 532 nm, and then proceed to photomultiplier (PMT) for signal transformation. The wavelength selection is based on the absorption wavelength of each intermediate state, illustrated in Fig. 2.9.

The yellow region in Fig. 2.8 highlights the signal detection and data acquisition. The changes in absorbance due to the photocycle were detected and recorded with an oscilloscope WaveSurfer 2MXs-B (LeCory). The signal was triggered by a

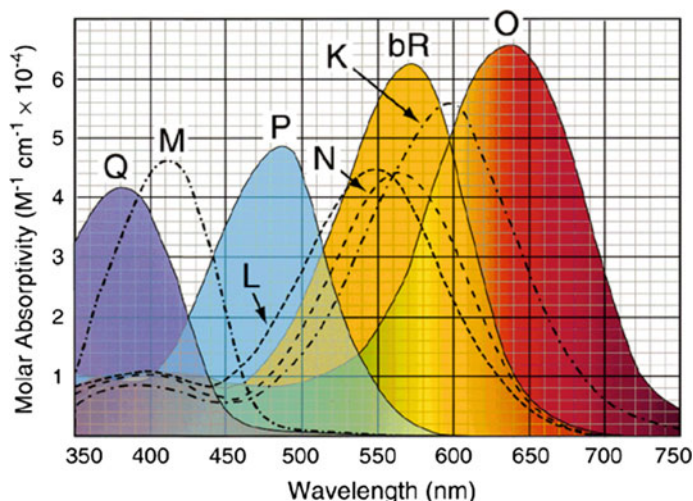


Fig. 2.9 Intermediate states and their absorption spectra during bR photocycle, reprint from with permission Ref. [18]. Copyright 1999 American Chemical Society

photodiode, placed around the optical pathway to detect the scattered intense laser pulse. Power meter 1919-R (Newport Crop.) detected the pulsed laser after beam splitter, and was recorded using a computer.

2.4 Transient Photocurrent Measurement

2.4.1 Principles

Photocurrent is the electrical current generated due to exposure to illumination. It may occur as a result of photoelectric, photoemissive or photovoltaic effects. For bacteriorhodopsin, the photovoltaic signals caused by the proton release have been previously studied [5–9]. As bR initiates photocycle and the proton pumping process, the protein releases a free proton into the bulk solution. Utilizing the concept of concentration cell, where both half-cells consist of the same chemical composition differing only in concentration, the changes in proton concentration due to the photocycle can be detected. In a concentration cell, a small voltage is generated as the concentration cell attempts to reach chemical equilibrium. By setting up the experiment so that bR is only contained in the working half cell, the proton released by bR during the photocycle leads to a proton gradient between the two half cells. The potential difference between the two half cells can be expressed as a function of concentration

$$V \propto \ln\left(\frac{n_0 + n_{H^+}(t)}{n_0}\right) = \ln\left(1 + \frac{n_{H^+}(t)}{n_0}\right) \quad (2.12)$$

n_0 represents the number densities of the cations, and $n_{H^+}(t)$ corresponds to the proton concentration modulation during the photocycle of bR. The concentration of the ions from NaCl is kept constant across the two half cells. Because the proton concentration modulation of $n_{H^+}(t)$ is relatively small in comparison to the bulk solution, Eq. 2.12 can therefore be approximated to [5]

$$V \propto n_{H^+}(t) \quad (2.13)$$

The current is defined as the rate of flow of the electron charge, Q . By using the relationship between charge, capacitance and voltage, the photocurrent can be derived in terms of the differentiation of the proton concentration related to the photocycle.

$$I = \frac{dQ}{dt} = C \frac{dV(t)}{dt} \propto \frac{d[n_{H^+}(t)]}{dt} \quad (2.14)$$

Thus the photocurrent measures the change of proton released by the protein into the bulk solution during the photocycle.

2.4.2 Experimental Setup

The photoelectrochemical cell is set up according to a study performed by Kuo and Chu [5], shown in Fig. 2.10. The experimental assembly is shown in Fig. 2.10a, where the sample cell is connected to a laser system. The neodymium-doped yttrium aluminum garnet (Nd:YAG) system LS-2134UTF (Lotis Tii), on the second harmonic (SH) mode generates a laser pulse at 532 nm and the signal passes through a mechanical shutter VS25S2T2 (Uniblitz), to monitor the repetition frequency. The laser pulse is introduced to the sample via wave-guider Model 77629 (Oriol Instruments). The photocurrent, generated by the proton release of bR during the photocycle, is amplified by an external current amplifier SR570 (Stanford Research System) before being recorded using oscilloscope WaveSurfer 2MXs-B (LeCory).

The photoelectrochemical cell is shown in Fig. 2.10b. The two identical pieces of glass with dimensions 25 mm \times 50 mm \times 1.1 mm, coated with fluorine-doped tin oxide (FTO, Sinoar Solar Corp.) on a single side, served as both a transparent window and the electrodes. Both working and reference cells consisted of a circular Teflon spacer and were placed on the FTO surface. The two cells are separated by a molecular porous membrane with MWCO 14 kDa (BioDesign Inc.), and both the sample and reference contain 50 mM NaCl.

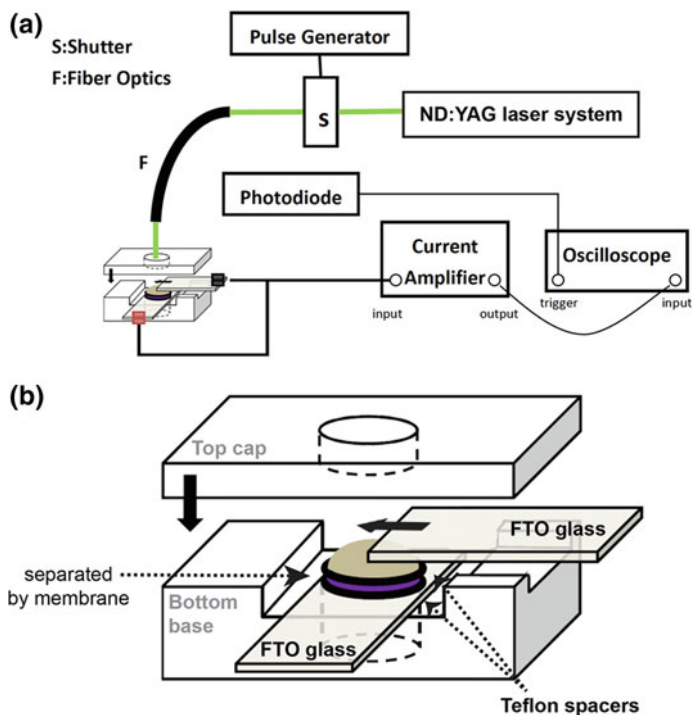


Fig. 2.10 Schematic diagram of the photoelectrochemical set up. **a** The cell is connected to a laser which generates excitation pulse to initiate bR photocycle. **b** Close up on the electrochemical cell, where the purple represents the bR containing working half cell, and the grey represent the reference half cell Adapted with permission from Ref. [5], copyright 2014 Elsevier

2.5 Solution State NMR

Nuclear magnetic resonance (NMR) spectroscopy utilizes the magnetic properties of nuclei to determine their physical and chemical properties. In protein studies, NMR spectroscopy is often employed to obtain information on the structure and dynamics of the protein, as the signals are highly sensitive to local environments. There are many specialized NMR spectroscopy techniques, each probes a specific condition, and the data is combined and processed to calculate the protein structure or interactions.

The spin quantum number is determined by the number of protons and neutrons in the nuclei, and nuclei with spin quantum number $I \geq \frac{1}{2}$ are magnetic and thus possess an intrinsic magnetic moment. Isotopes are defined by nuclei with the same chemical properties but a different number of neutrons, where they can be distinguished by their spin quantum number and by gyromagnetic ratio, γ . The magnitude of the spin angular momentum, L , is quantized by

$$L = [I(I + 1)]^{\frac{1}{2}}\hbar \quad (2.15)$$

\hbar is the reduced Plank's constant. Spin angular momentum is a vector, with its direction and magnitude quantized. The z component of spin angular momentum is given by

$$I_z = m\hbar \quad (2.16)$$

where $m = I, I - 1, \dots, -I$. Spin gives rise to magnetic moment,

$$\mu_z = \gamma I_z \quad (2.17)$$

where the gyromagnetic ratio, γ , is the ratio between the magnetic dipole moment to the angular momentum of the nuclei. When the nuclei is placed in an applied magnetic field, B_0 , the frequency at which the magnetization precesses around the field is defined by the Larmor frequency, ω_0 , of a nuclei spin,

$$\omega_0 = -\gamma B_0 \quad (2.18)$$

An NMR experiment measures the Larmor frequency, and it can be measured as a change of energy

$$|\Delta E| = |\hbar\gamma B_z| \quad (2.19)$$

The sample is placed in a strong magnetic field B_0 and a second magnetic field, B_1 , is applied. B_1 is relatively weak in comparison B_0 and is generated using a radio frequency (rf) pulse

$$\hat{B}_1 = |B_1|\cos(\omega_{rf}t + \phi) \quad (2.20)$$

When $\omega_{rf} = \omega_0$, the magnetization will nutate around the direction of the B_1 pulse. This means that only the nuclei close to or on resonance are affected. In this case, an on resonance 90° pulse will create a transverse magnetization. When such a pulse is switched off, the transverse magnetization will precess around B_0 at the frequency ω_0 to return to thermal equilibrium. The NMR signal is generated by this phenomenon in a coil through electromagnetic induction. The schematic description is shown in Fig. 2.11.

In a multiple spin system there exists many different interactions such that the Hamiltonian operator can be expressed as

$$H = H_z + H_Q + H_D + H_{CS} + H_{CSA} + H_J \quad (2.21)$$

where H_z is the Zeeman interaction between the nuclei and the external magnetic field, H_Q is the quadrupolar interaction for nuclei with $I > \frac{1}{2}$, H_D is the homonuclear and heteronuclear dipolar interaction, H_{CS} is the isotropic chemical shift, H_{CSA}

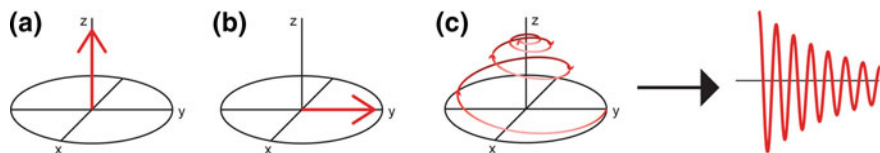


Fig. 2.11 Schematic vector diagram of (a) magnetization at thermal equilibrium, (b) transverse magnetization due to on-resonance rf pulse and (c) after the rf pulse has been switched off and then magnetization precesses around B_0 at the Larmor frequency returning to the equilibrium state via relaxation. This generates a NMR signal which can be Fourier transformed into the frequency domain

is the chemical shift anisotropy and H_J is the spin-spin J coupling. In solution state NMR spectroscopy, spatial dependent and anisotropic interactions such as dipolar interaction and CSA are averaged due to the fast tumbling of molecules in solution. By employing nuclei with $I = 1/2$, quadrupolar interaction can be eliminated.

Isotropic chemical shift describes the electronic shielding induced by the external magnetic field B_0 . The external magnetic field creates a small current flow in the electron orbitals, and generates a local magnetic field that is dependent on the surrounding chemical environment whereby

$$B_z = (1 - \sigma)B_0 \quad (2.22)$$

σ is the chemical shielding. Including this equation into Eq. 2.18, the observed Larmor frequency, ω , becomes

$$\omega = -\gamma B_0(1 - \sigma) \quad (2.23)$$

Since different electronic arrangements and bonding give rise to different chemical shielding, the resulting chemical shift is unique to the environment of nuclei. By comparing to reference frequency of a standard sample, ω_{ref} , chemical shift, δ , can be measured independent to the external magnetic field strength,

$$\delta = \frac{(\omega - \omega_{ref})}{\omega_{ref}} \times 10^6 \quad (2.24)$$

The factor of 10^6 is required to express chemical shift in terms of parts per million (ppm).

Two-dimensional (2D) correlation NMR is often used to study protein dynamic and structure. 2D NMR consists of four stages, as shown in Fig. 2.12: preparation, evolution, mixing and detection. The main difference between two-dimensional and one-dimensional NMR spectroscopy is the evolution and the mixing periods. During the preparation state, magnetization coherence is created by *rf* pulses, while in the evolution time no pulse will be present and the magnetization is free to precess. The mixing period manipulates the magnetization by *rf* pulses and results in the observable signal, and the NMR signal is detected in the form of free induction

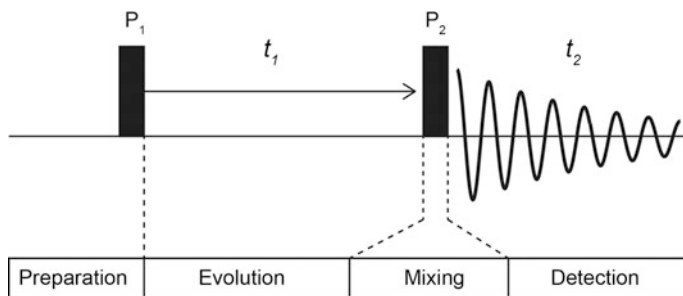


Fig. 2.12 Schematics of general pulse sequence structure for a 2D NMR experiment. The stages include preparation, evolution, mixing and detection

decay. A 2D NMR spectrum is generated by a series of one-dimensional experiments with different duration of evolution periods. Both dimensions in a 2D NMR spectrum are shown in frequency, which in turn are represented in chemical shift.

Heteronuclear single quantum correlation spectroscopy (HSQC) detects the correlation between two different types of nuclei that are connected by a chemical bond. The general pulse sequence for a HSQC experiment is shown in Fig. 2.13. ^1H - ^{15}N HSQC is frequently performed in the study of protein to check the size and the folding of a protein. For a folded protein, the spectrum will usually be well dispersed. Each amino acid with the exception of proline contains an amide proton attached to the backbone nitrogen, providing at least one signal to the spectrum. ^1H - ^{15}N HSQC experiment is relatively sensitive and can be acquired in a short period of time, making it ideal for preliminary experiments in protein NMR studies. Moreover, ^1H - ^{15}N HSQC can be used to study protein-protein interaction or protein-ligand binding experiments, as the changes in structure or interaction can be detected through changes in chemical shift. HSQC can also be combined with other NMR pulse sequence schemes to achieve higher dimensional NMR experiments for sequence assignments and structural determinations.

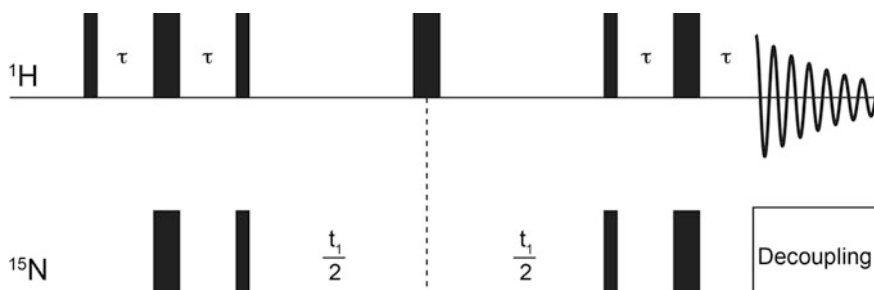


Fig. 2.13 General pulse sequence of ^1H - ^{15}N HSQC. The thin black square represent 90° pulse, whereas the thicker black square represent 180° pulse

2.6 Nanodisc Assembly and Optimization

2.6.1 MSP Expression and Purification

Membrane scaffold proteins, MSP1E3D1 and MSP1E3D1_srt (E3D1_srt), which is MSP1E3D1 with an additional his tag and a sortase recognition site, and GB1_MSP1D1ΔH5_srt (GB1ΔH5_srt), were expressed using *E. coli* with pET28 vector with kanamycin antibiotic resistance. The additional soluble protein, protein G domain B1 (GB1) fused on the N terminal of ΔH5_srt is to increase the protein expression yield. While MSP1E3D1 and E3D1_srt were expressed using Rosetta with an additional chloramphenicol antibiotic resistance, GB1ΔH5_srt was expressed using BL21 (DE3). The bacteria carrying the plasmid were first transformed. The overnight culture was grown from 2 to 3 colonies, and was grown for 14–16 h in 37 °C before transferring into the expression culture. The bacteria were grown to optical density at 600 (OD₆₀₀) of 0.8–1.0 before inducing with 1 mM IPTG. In the case of GB1ΔH5_srt, the induction was performed at 30 °C. The bacteria were harvested after 4–5 h of induction for E3D1_srt and after 6 h for GB1ΔH5_srt. The bacterial pellet was kept at –80 °C until purification.

The purification buffer of MSP is shown in Table 2.1. The bacterial pellet was resuspended in a buffer containing 50 mM Tris-HCl, 500 mM NaCl, 1 mM EDTA, 1 mM PMSF, 1% Triton X-100, a small amount of DNase and lysozyme. After the bacterial pellet had fully suspended, lysis was done by sonication using Q700 sonicator (QSonica) at amplitude 25 with 1 s on and 3 s off, for 4 min. After the insoluble membrane fraction was separated using centrifugation, the solutions were then applied onto a Ni-NTA column that was equilibrated with suspension buffer. The samples were bound to the column for 1 h with gentle agitation.

After binding to Ni-NTA, the resins were washed with wash buffers containing 50 mM Tris-HCl, 500 mM NaCl at pH 8 and different detergent or imidazole concentrations. Wash buffer 2 has an additional 1% Triton X-100, whereas wash buffer 3 contains 50 mM sodium cholate. Wash 4 contains 20 mM imidazole and the protein was eluted from the resins with 500 mM imidazole. The eluted sample

Table 2.1 Purification buffer of membrane scaffold protein

Buffer	
Lysis	50 mM Tris HCl, 500 mM NaCl, 1 mM EDTA, 1 mM PMSF, 1% Triton X-100, DNase and lysozyme, at pH 8
Wash 1	50 mM Tris-HCl, 500 mM NaCl, pH 8
Wash 2	Wash 1 + 1% TX-100, pH 8
Wash 3	Wash 1 + 50 mM sodium cholate, pH 8
Wash 4	Wash 1 + 20 mM imidazole, pH 8
Wash 5	Wash 1 + 100 mM imidazole, pH 8
Elution	Wash 1 + 500 mM imidazole, pH 8
Dialysis	25 mM Tris-HCl, 100 mM NaCl, 0.5 mM EDTA, pH 7.5

was concentrated down to less than 10 ml using Centricon, before the imidazole was removed using dialysis overnight. The concentration of the purified protein was checked with NanoDrop, and the purity was verified using SDS PAGE and MALDI-TOF mass spectroscopy. In the case of MSP1E3D1 and MSP1E3D1_srt, the purification procedure had an additional wash using wash buffer 5, containing 100 mM imidazole before elution to avoid high molecular weight impurities.

For GB1 Δ H5_srt, the protein was purified using size exclusion chromatography after elution from Ni-NTA to separate impurities consisted of GB1, using HiLoad 16/600 Superdex 75. The fractions were checked with SDS PAGE and only fractions containing only GB1 Δ H5_srt were collected, shown in Fig. 2.14.

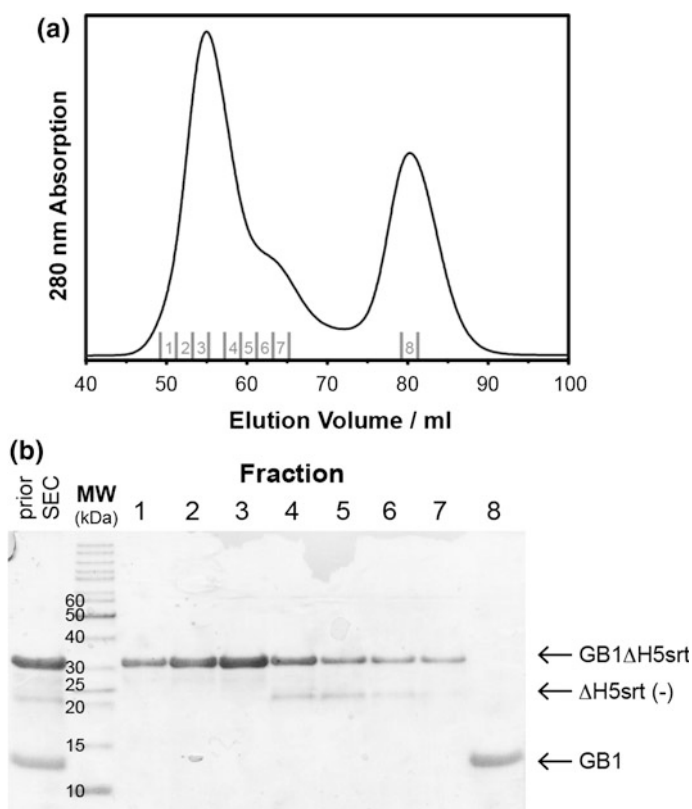


Fig. 2.14 **a** Size exclusion chromatography profile and **b** SDS PAGE of individual fractions for the purification of GB1 Δ H5_srt

2.6.2 Circularization of *cMSP*

Conventional nanodiscs were assembled using linear-form MSPs. The N and C terminal are held together through self-assembly, but the ends are not joined together thus the content of the nanodisc, particularly small lipid molecules, can move in and out of the MSP belts. This may lead to unfavorable lipid aggregation, especially at high concentration and higher temperature, and complicate the biophysical analysis. Inspired by circular proteins found in nature with circular backbones to prevent degradation [10, 11], MSP was designed to chemically join its N and C termini to improve stability [12, 13]. An additional Sortase A recognition site was added onto the MSP to undergo a sortase mediated catalytic reaction [14].

The schematic of E3D1_srt sortase catalyzed circularization reaction into cE3D1 is described in literature [13] and presented Fig. 2.15a. The process is the same for GB1ΔH5_srt. Evolved Sortase A (SrtA) required for the circularization process was expressed using *E. coli* with pET29 vector with kanamycin antibiotic resistance. The plasmid of SrtA was transformed into BL21(DE3) and the bacteria was grown in the expression culture until OD₆₀₀ reached 0.8 before the protein expression was induced with 0.45 mM IPTG at 30 °C for 3 h. The bacteria was centrifuged after harvest and the bacterial pellet was kept at -80 °C until purification. During purification, the bacterial pellet was resuspended in SrtA lysis buffer as described in Table 2.2. After binding to Ni-NTA for 1 h at 4 °C, the resin was washed with each of the wash buffers for 10 CV, before the protein was eluted from the resin using SrtA elution buffer. Imidazole was then removed via dialysis overnight.

E3D1_srt contains a polyhistidine tag on both the N and the C terminals, with an additional sortase recognition site located on the N terminal. First, the N terminal his tag was cleaved by TEV protease cleavage reaction to expose the sortase recognition site, with E3D1_srt to TEV ratio at 10 to 1 and cleaved for 15 h in RT. The TEV protease cleaved E3D1_srt(-) was diluted with a buffer containing 50 mM Tris-HCl, 150 mM NaCl and 2 mM Triton X-100 at pH 7.5. The mixture was added into the reaction mixture containing 3 μM of SrtA, 50 mM Tris-HCl, 150 mM NaCl, 1 mM Triton X-100 and 10 mM CaCl₂. The final ratio between E3D1_srt and SrtA was 1 to 1. The reaction was stirred in RT for 15 h before the sample was purified using Ni-NTA to remove SrtA, TEV protease and unreacted E3D1_srt(-). The Ni-NTA flowthrough was collected and condensed before the detergent was removed using BioBeads with overnight treatment. The final product, cE3D1, was characterized using SDS PAGE and MALDI-TOF mass spectroscopy, shown in Fig. 2.15b and c.

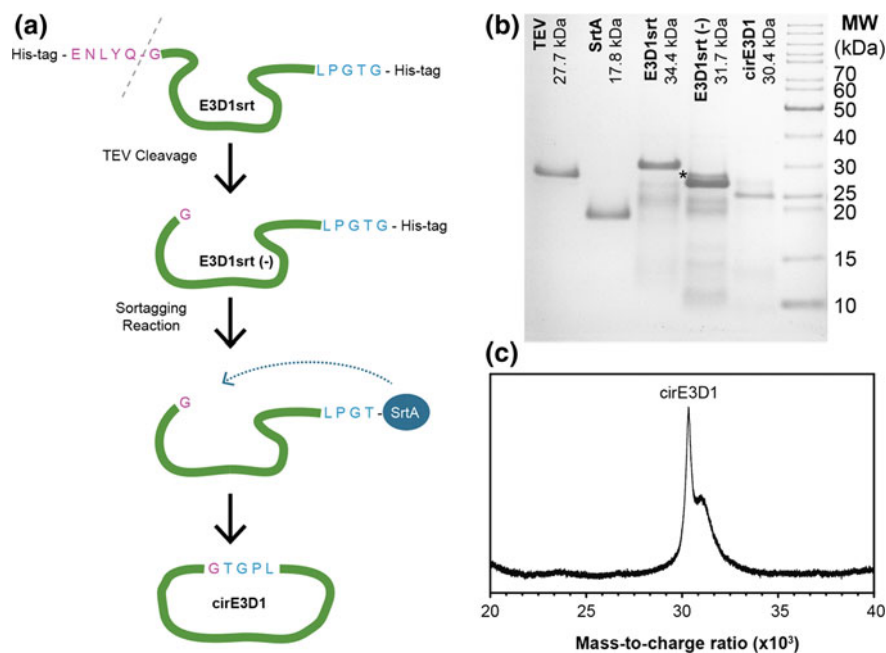


Fig. 2.15 Schematics of the circularization process of cE3D1 from E3D1srt **(a)**. The products during the circularization can then be characterized using **b** SDS PAGE and **c** MALDI-TOF mass spectra

Table 2.2 Purification buffers of SrtA

Buffer	
Lysis	50 mM Tris HCl, 300 mM NaCl, 1 mM MgCl ₂ , 1 mM PMSF, DNase and lysozyme, at pH 8
Wash 1	50 mM Tris-HCl, 300 mM NaCl, 5 mM imidazole, pH 8
Wash 2	Wash 1 with 20 mM imidazole, pH 8
Elution	Wash 1 + 500 mM imidazole, pH 8
Dialysis	50 mM Tris-HCl, 150 mM NaCl, pH 7.5

2.6.3 Lipid and MSP Optimization

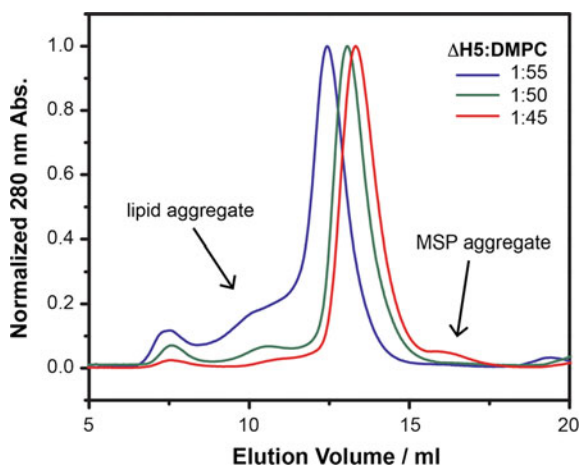
Membrane scaffold protein, lipid in detergent and target protein were mixed and incubated for 2 h before the detergent was removed with 400 mg of BioBeads per 500 μ l of assembly mixtures. The samples were treated with BioBeads with gentle agitation for at least 4 h in 4 °C, and the BioBeads were separated from the sample via centrifugation at $3381 \times g$ (6000 rpm) using Centrifuge 5425 R (Eppendorf).

The samples underwent fast centrifugation at $21130 \times g$ (15000 rpm) in order to remove precipitation before further purification using chromatography methods.

During nanodisc assembly, the membrane scaffold protein to lipid ratio is crucial to obtain a narrow distribution of nanodisc homogeneity. It is therefore important that the MSP to lipid ratio is optimized prior to incorporating the target protein for biophysical studies.

Figure 2.16 demonstrates an optimization process of MSP to DMPC ratio using linear MSP1D1 Δ H5 without joint termini with size exclusion chromatography. When the lipid to membrane scaffold protein ratio is too high, suggesting an excess amount of lipid in assembly mixture, the extra lipid would either enlarge a portion of the nanodisc causing the distribution to increase, or form large aggregation after the detergent has been removed. On the other hand, when the lipid to membrane scaffold protein ratio is too low, corresponding to an excess of membrane scaffold protein, the membrane scaffold protein would aggregate and thus decrease the efficiency and yield of the nanodisc formation. Moreover, the lipid to membrane scaffold protein ratio varies with different lipids even when the same membrane scaffold protein is used, as the packing of each lipid would differ depending on the charge of the hydrophilic head or the size and status of the hydrophobic tails. There is also a slight alteration of the lipid to membrane scaffold protein ratio across different batches of membrane scaffold protein expression or lipid in detergent preparation, due to the small inaccuracy in determination of protein concentration or measurements of lipid weight.

Fig. 2.16 Size exclusion chromatography of empty nanodisc composed of MSP1D1 Δ H5 and DMPC at different MSP to lipid ratios



2.7 PM Preparation

2.7.1 *H. salinarum* Culture

Halobacterium salinarum S9 was grown according to the protocols outlined by Oesterhelt and Stoeckenius [15]. After the expression culture shown in Table 2.3 was prepared the pH of the expression culture was adjusted to pH 7.4 using NaOH and the culture was autoclaved and sterilized. During the culture, since no bacteria can survive such harsh conditions, no antibiotic was necessary to avoid contamination. *H. salinarum* was expressed either with 1 L in 2.5 L Erlenmeyer flask or 2 L in Winpact Bench-Top Fermenter (Major Science). The expression culture was grown from the mature smaller culture of 20 ml, and was grown at 38 °C with illumination. As the population of *H. salinarum* grew the oxygen and nutrient level in the medium decreased rapidly. After 1 week of growth the colour of the culture would turn from yellow to pink, corresponding to the expression of functional bR. The expression of bR and production of PM was checked by centrifuging a small amount of culture daily and compares the increase of purple pellet. Once the bacterial pellet ceased to increase, *H. salinarum* was harvested by centrifuge and directly proceeded to lysis and purification to preserve the integrity of PM and avoid loss of yield.

2.7.2 PM Isolation

The PM containing bacterial pellet was resuspended in 4 M NaCl. Lysis of *H. salinarum* was achieved by adding a small amount of DNase and gentle shaking overnight. The lysis mixture was then dialyzed first in 0.1 M NaCl, then twice in doubly distilled water, each over night at 4 °C. The dialysis process induced lysis by osmosis and the gentle breaking of membrane. The membrane fraction containing purple membrane was obtained by fast centrifuge at $27216 \times g$ (15000 rpms) for 1 h using Avanti J-26S XP Centrifuge JA25.50 rotor (Beckman). The purple membrane was then suspended in distilled water, and transferred to a tissue

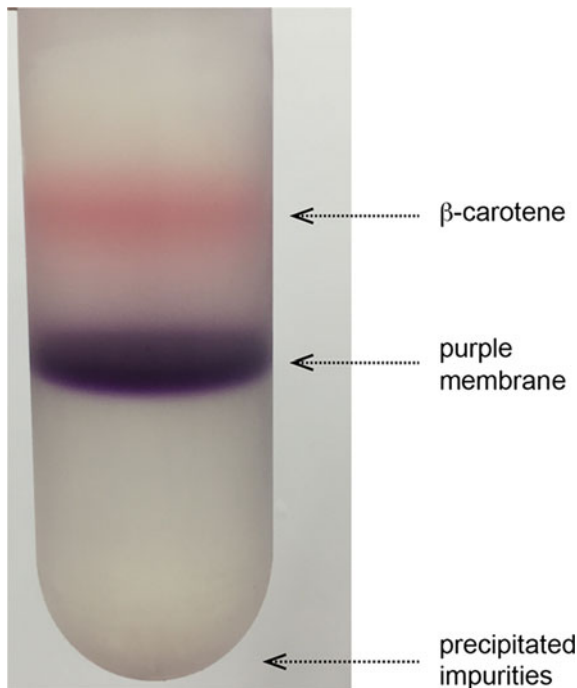
Table 2.3 Chemical composition of *H. salinarum* S9 strain culture medium

Chemical	Weight per litre/gL ⁻¹	Concentration/M
ddH ₂ O	Up to 4 L	
NaCl	250	4.28
KCl	2	2.68×10^{-2}
MgSO ₄	9.75	8.10×10^{-2}
CaCl ₂	0.202	1.82×10^{-3}
Na ₃ C ₆ H ₅ O ₇	3.4	1.16×10^{-2}
Peptone (LP0037)	10	

grinder. By creating a gentle vacuum using the tissue grinder, some intertrimer interaction was disrupted and large aggregation broken, allowing removing of impurities that were previously aggregated with PM. The purified PM was separated from β -carotene and impurities by sucrose gradient. The gradient consisted of 40%, 50%, 60% sucrose in distilled water, at 7 ml, 7 ml and 3 ml, respectively. The sucrose gradient purification was performed at $87300 \times g$ (22000 rpm) using Optima XE-90 Ultracentrifuge SW28 swing bucket rotor (Beckman) for 22 h, with slow deceleration to maintain the final gradient. Shown in Fig. 2.17 is the final sucrose gradient with a clear separation of β -carotene and impurities. The dark purple fraction was carefully extracted and the sucrose content was later removed by another centrifugation. After the purified, insoluble purple membrane was separated from the supernatant, purple membrane was resuspended in distilled water.

The sample was sonicated briefly using Q700 sonicator (QSonica) at amplitude 20 with 1 s on and 3 s off, for 1 min, to break apart the large aggregation of PM. This prevents light scattering of large particles in the sample. Finally the concentration of PM was estimated using steady state spectroscopy, using the absorption at 568 nm and extinction coefficient of bR at that wavelength $\epsilon_{568} = 62700 \text{ M}^{-1}\text{cm}^{-1}$. PM was stored at 4 °C.

Fig. 2.17 Sucrose gradient purification of purple membrane (PM), with double distilled water, 40% sucrose, 50% sucrose and 60% sucrose layers. Image reproduced with premission from Ref. [19], from Nature Publishing Group



2.8 HmbRI Preparation

2.8.1 Site Directed Mutagenesis

The plasmid of wild type HmbRI and HmbRII was generously provided by Professor Chii-Shen Yang from the department of Biochemical Science and Technology, National Taiwan University. The mutation of D94N from wild type HmbRI was achieved by mutating a DNA sequence from GAC to AAC. The forward and reverse primers, synthesized (Genomics BioSci and Tech) were 5'-CAACGCCGTTGCTGCTGTATAACCTCGGACTGCTTGCAGG-3' and 5'-CCTGCAAGCAGTCCGAGGTTATACAGCAGCAACGGCGTTG-3', respectively. The PCR reaction for site directed mutagenesis was performed with 40 ng of template containing wild type HmbRI, 0.2 μ M of primer pair, 200 μ M dNTPs, 1x Fusion DNA polymerase, using Mastercycler pro (Eppendorf). The reaction was started by an initial denaturation at 98 °C for 1 min then followed by 25 cycles, consisting of 25 s of denaturation at 98 °C, 20 s of annealing at 55 °C and 4 min elongation at 68 °C. The reaction was terminated with an additional 5 min elongation at 68 °C. The PCR product was then treated with a unit of Dpn1 at 37 °C for 3 h before purification using Gel/PCR DNA fragment extraction kit DF100/DF300 (Geneaid Biotech). The purified plasmid was then amplified by transformation into *E. coli* DH5 α . The sequence was confirmed by Sequencing Center at National Taiwan University, Taipei.

2.8.2 HmbRID94N Culture and Purification

The expression vectors containing HmbRID94N were transformed into *E. coli* C43 (DE3) [16]. The bacteria was grown in small volume overnight using LB in 37 °C with carbenicillin antibiotics. For protein production, the appropriate volume of overnight culture was transferred to a large expression culture in Erlenmeyer flask and grown until OD₆₀₀ was around 1.0 at 37 °C. The culture was then induced with 0.5 mM IPTG and 10 μ M of *all-trans* retinal (Sigma). The retinal was necessary for the functionality of bR. Unlike in the case of HsbR expression using *H. salinarum*, *E. coli* does not produce the retinal hence the molecule must be added separately. Shown in Fig. 2.18b is the result of HmbRID94N expression with and without the addition of *all-trans* retinal. The culture was harvested after 5 h of induction and the bacterial pellet was kept in -80 °C until purification.

For purification, the bacterial cell was suspended in buffer containing 50 mM Tris, 4 M NaCl, 0.2 mM PMSF, 14.2 mM β -mercaptoethanol, a small amount of lysozyme and DNase. The cell was disrupted using sonication, with 1 s on 3 s off for 120 s. The cell lysate was then centrifuged at high speed to separate the membrane and the soluble fraction, and the insoluble membrane fraction was dissolved in solubilization buffer containing 2% DDM for at least 24 h. The sample

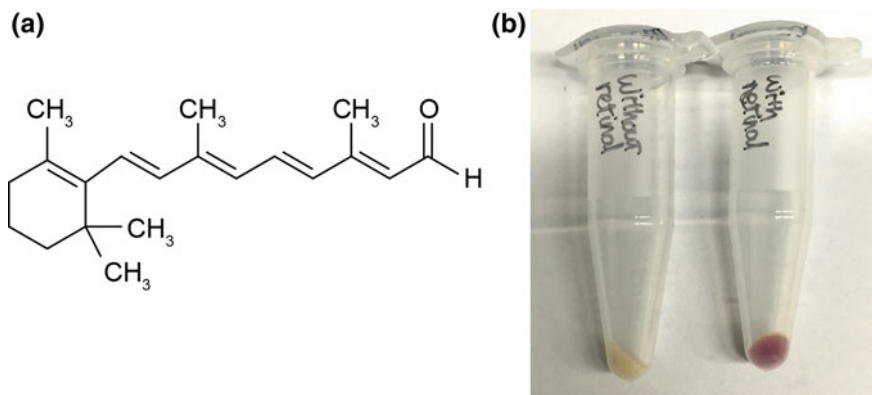


Fig. 2.18 **a** Structure of all-trans retinal required for the expression of HmbRID94N, which is commercially available. **b** Harvest bacterial pellet expression HmbRID94N using the same conditions except without (left) and with (right) addition of 10 μM all-trans retinal during IPTG induction

was kept in a dark environment to avoid protein denaturing. After solubilization and another centrifugation to separate the solubilized fraction and the insoluble impurities, the supernatant was applied onto Ni-NTA column in 4 $^{\circ}\text{C}$ for 1 h of binding. After incubation, the column was washed with wash buffers 1, 2 and 3 before the protein was eluted from the column using elution buffer. The chemical composition of each buffer is detailed in Table 2.4. The excess imidazole was removed using dialysis overnight.

The purity of the protein was checked with SDS-PAGE, shown in Fig. 2.19, and the concentration of the protein was determined using 280 nm absorption and extinction coefficient of $68410 \text{ M}^{-1}\text{cm}^{-1}$.

Table 2.4 HmbRID94N purification buffers using DDM

Buffer	Chemical composition
Lysis	50 mM Tris-HCl, 4 M NaCl, 0.2 mM PMSF, 14.7 mM β -mercaptoethanol, small amount of lysozyme and DNase, pH 8
Solubilization	50 mM Tris-HCl, 4 M NaCl, 0.2 mM PMSF, 14.7 mM β -mercaptoethanol, small amount DNase and 2% DDM, pH 8
Wash 1	50 mM Tris-HCl, 4 M NaCl, 0.05% DDM, pH 8
Wash 2	Binding buffer + 20 mM imidazole
Wash 3	Binding buffer + 50 mM imidazole
Elution	50 mM Tris-HCl, 1 M NaCl, 0.1% DDM, 300 mM imidazole, pH 8
Dialysis	25 mM Tris-HCl, 100 mM NaCl, 0.5 mM EDTA, pH 7.5

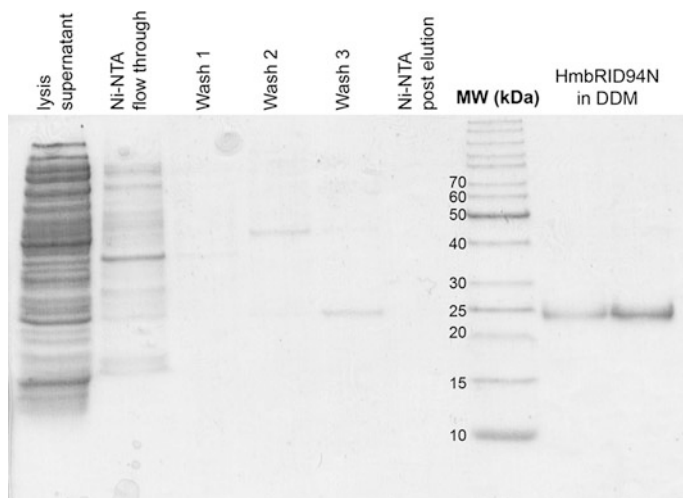


Fig. 2.19 SDS PAGE of HmbRID94N purification using DDM

2.8.3 Isotopic Labeling Expression

A benefit of using *E. coli* to express HmbRID94N, rather than growing the native archaea like *H. salinarum* for HsbR, is the convenience of isotopic labeling of HmbRID94N for NMR experiments. For HSQC experiment, HmbRID94N was expressed with ^2D and ^{15}N labels using modified high salt minimum media [17] dissolved in D_2O . The chemical composition of the expression media is detailed in Table 2.5.

The expression vector containing HmbRID94N was transformed into *E. coli* C43(DE3) and was grown overnight in small volume in LB at 37°C . The overnight culture was briefly centrifuged for 3 min at $1811 \times g$ (3000 rpm) using Centrifuge 5810 R (Eppendorf) to collect the bacteria. The LB was removed and the bacterial pellet was carefully suspended with the high salt minimum media to avoid any disruption of the cell, then the resuspended bacterial culture was added to a small

Table 2.5 Chemical composition of modified high salt minimum media per 1 L of expression culture

Chemical	/L
KH_2PO_4	13 g
K_2HPO_4	10 g
Na_2HPO_4	9 g
K_2SO_4	2.4 g
$^{15}\text{NH}_4\text{Cl}$	1 g
MgCl_2	0.952 g
Glucose	4 g
Trace elements + vitamin	1x
ISOGRO	0.5 g

volume of high salt minimum media for adaptation growth. The bacteria was adapted for 6 h and was added to large expression culture, where it was grown until OD_{600} before induction with 0.5 mM IPTG and 10 μ M of *all trans* retinal. 0.5 g/L of 2D , ^{15}N labeled ISOGRO (Sigma) growth medium was added during the addition of IPTG and *all trans* retinal to provide enrichment and increase expression yield. Due to the substitution of D_2O for H_2O which would significantly slow down the growth and expression rate of the bacteria, the culture was induced for 10 h before harvest. The purification procedure of 2D , ^{15}N labeled protein is the same as LB expressed, unlabeled protein.

References

1. Hong P, Koza S, Bouvier ESP (2012) Size-exclusion chromatography for the analysis of protein biotherapeutics and their aggregates. *J Liq Chromatogr Relat Technol* 35:2923–2950. <https://doi.org/10.1080/10826076.2012.743724>
2. Heyn MP, Cherry RJ, Dencher NA (1981) Lipid-protein interactions in bacteriorhodopsin-dimyristoylphosphatidylcholine vesicles. *Biochemistry (Mosc)* 20:840–849. <https://doi.org/10.1021/bi00507a029>
3. Becher B, Ebrey TG (1976) Evidence for chromophore-chromophore (exciton) interaction in the purple membrane of *Halobacterium halobium*. *Biochem Biophys Res Commun* 69:1–6. [https://doi.org/10.1016/S0006-291X\(76\)80263-X](https://doi.org/10.1016/S0006-291X(76)80263-X)
4. Pescitelli G, Woody RW (2012) The exciton origin of the visible circular dichroism spectrum of bacteriorhodopsin. *J Phys Chem B* 116:6751–6763. <https://doi.org/10.1021/jp212166k>
5. Kuo C-L, Chu L-K (2014) Modeling of photocurrent kinetics upon pulsed photoexcitation of photosynthetic proteins: a case of bacteriorhodopsin. *Bioelectrochemistry* 99:1–7. <https://doi.org/10.1016/j.bioelechem.2014.05.003>
6. Miyasaka T, Koyama K (1992) Rectified photocurrents from purple membrane Langmuir-Blodgett films at the electrode-electrolyte interface. *Thin solid films* 210–211. Part 1:146–149. [https://doi.org/10.1016/0040-6090\(92\)90193-F](https://doi.org/10.1016/0040-6090(92)90193-F)
7. Liu SY, Govindjee R, Ebrey TG (1990) Light-induced currents from oriented purple membrane: II. Proton and cation contributions to the photocurrent. *Biophys J* 57:951–963. [https://doi.org/10.1016/S0006-3495\(90\)82615-1](https://doi.org/10.1016/S0006-3495(90)82615-1)
8. Okajima TL, Hong FT (1986) Kinetic analysis of displacement photocurrents elicited in two types of bacteriorhodopsin model membranes. *Biophys J* 50:901–912. [https://doi.org/10.1016/S0006-3495\(86\)83531-7](https://doi.org/10.1016/S0006-3495(86)83531-7)
9. Simmeth R, Rayfield GW (1990) Evidence that the photoelectric response of bacteriorhodopsin occurs in less than 5 picoseconds. *Biophys J* 57:1099–1101. [https://doi.org/10.1016/S0006-3495\(90\)82629-1](https://doi.org/10.1016/S0006-3495(90)82629-1)
10. Craik DJ, Allewell NM (2012) Thematic minireview series on circular proteins. *J Biol Chem* 287:26999–27000. <https://doi.org/10.1074/jbc.R112.390344>
11. Craik DJ, Čemažar M, Wang CKL, Daly NL (2006) The cyclotide family of circular miniproteins: nature's combinatorial peptide template. *Pept Sci* 84:250–266. <https://doi.org/10.1002/bip.20451>
12. Nasr ML, Baptista D, Strauss M et al (2016) Covalently circularized nanodiscs for studying membrane proteins and viral entry. *Nat Methods* advance online publication: <https://doi.org/10.1038/nmeth.4079>
13. Yusuf Y, Massiot J, Chang Y-T et al (2018) Optimization of the production of covalently circularized nanodiscs and their characterization in physiological conditions. *Langmuir* 34:3525–3532. <https://doi.org/10.1021/acs.langmuir.8b00025>

14. Antos JM, Popp MW-L, Ernst R et al (2009) A straight path to circular proteins. *J Biol Chem* 284:16028–16036. <https://doi.org/10.1074/jbc.M901752200>
15. Oesterhelt D, Stoekenius W (1974) Isolation of the cell membrane of *Halobacterium halobium* and its fractionation into red and purple membrane. *Methods Enzymol* 31:667–678
16. Hsu M-F, Yu T-F, Chou C-C et al (2013) Using haloarcula marismortui bacteriorhodopsin as a fusion tag for enhancing and visible expression of integral membrane proteins in *Escherichia coli*. *PLoS One* 8:e56363. <https://doi.org/10.1371/journal.pone.0056363>
17. Cai M, Huang Y, Sakaguchi K et al (1998) An efficient and cost-effective isotope labeling protocol for proteins expressed in shape *Escherichia coli*. *J Biomol NMR* 11:97–102
18. Birge RR, Gillespie NB, Izaguirre EW et al (1999) Biomolecular electronics: protein-based associative processors and volumetric memories. *J Phys Chem B* 103:10746–10766. <https://doi.org/10.1021/jp991883n>
19. Yeh V, Lee T-Y, Chen C-W et al (2018) Highly efficient transfer of 7TM membrane protein from native membrane to covalently circularized nanodisc. *Scientific Reports* 8(1)

Chapter 3

Effect of Lipid Composition of Nanodisc



3.1 Introduction

As discussed in Chap. 1, the idea of using a membrane mimic for studying membrane protein is not only for solubilization of the membrane protein but also to provide the protein a near native environment, ensuring the relevant structures and the functions are preserved. Introduced in Chap. 1, nanodisc has been utilized to study numerous membrane proteins. The ability to be able to embed membrane protein in a near native phospholipid bilayer while keeping the size of the complex reasonable has advanced the use of solution NMR in the studies of membrane protein. An advantage of nanodisc is the flexibility of lipid composition. In lipid bicelle, and composition of lipid, the choice of detergent and the ratio between the two are kept very specific in order to produce size homogenous bicelle. This means that the choice of lipid composition is limited. In nanodisc, however, the choice of lipid bilayer composition is only limited by the lipid molecule's ability to self assemble into lipid bilayer in aqueous solution without solubilization agents. Most commonly used phospholipids in nanodisc are zwitterionic, such as DMPC, POPC, DPPC [1], with some negatively charged PG lipids incorporated to increase stability [2].

The effect of lipid composition has been known to be an important factor affecting the structure, function or stability of certain membrane proteins. For example, in the cases of bacterial secondary transporters, some proteins were found unable to functionally fold in *E. coli* lacking PE lipids [3, 4]. Lipid composition can affect a large range of membrane properties such as charge, curvature or curvature stress, membrane thickness or packing and specific lipid-protein interaction. The effect of the surrounding lipid composition on the function of bacteriorhodopsin has been suggested by previous studies [5, 6]. The interaction between bR and the surrounding membrane lipids is proposed to have significant effect on its photocycle [7, 8], where some native lipids were shown to be more important than others in preserving the photocycle kinetics of PM.

Bacteriorhodopsin has been successfully incorporated into liposomes [9–11] or nanodisc [12] composed of synthetic lipids. Demonstrated by Wang et al. the synthetic lipid composition of the liposome can alter the intermediate state M decay of the bR reconstituted onto the liposome [13]. However, the lipid composition also influences the orientation of the proton pump [13, 14], with similar phenomenon reported for proteorhodopsin [15]. This further complicates the investigation on the effect of the lipid, as an inward pumping and an outward pumping bacteriorhodopsin would behave differently. Another concern during the studies of bR using liposome is the inhomogeneous sample, where the number of proteins on a vesicle is difficult to monitor, particularly with the changes in lipid composition. Liposome also introduces optical scattering due to its physical properties, which would affect the signal-to-noise ratio [16].

By utilizing the homogenous and disc-like nature of nanodisc, the concerns of bR orientation and homogeneity associated with lipid composition can be eliminated. Furthermore, nanodisc can provide a size homogenous lipid environment with exact control of the lipid ratio between zwitterionic and negatively charged hydrophilic heads, and between the saturated and unsaturated hydrophobic tails. By using MSP1E3D1 membrane scaffold protein we were able to produce larger nanodisc, which introduces less structural confinement in comparison to the smaller nanodisc assembled using MSP1D1. By systematically studying of monomeric bR incorporated into nanodisc of different lipid composition, we were able to demonstrate the significant influence of lipid on the function of bR using transient absorption spectroscopy and electrochemical measurement. The results indicate a decrease in the negatively charged lipid content leads to an increase in photocycle lifetime, in particular decelerated kinetics of the intermediate M, suggesting a decreased rate of proton translocation. While the photocycle duration increases, the decrease in the negatively charged lipid content also leads to decreased populations of intermediates N and O, suggesting an alteration in the photocycle pathway. On the other hand, photocurrent measurements results show that even though a decrease in the negatively charged lipid content results in longer intermediate M lifetime, the neutral and the positively charged lipid were found to assist in the release of protons from the protein after proton translocation. In addition to the effect of the charge of lipid, the structure of the hydrophobic lipid tails was found to have minor influence over the photocycle kinetics. This suggests that although the charge of the lipid hydrophilic head is the dominant factor when tuning the photocycle kinetics of bacteriorhodopsin embedded in nanodisc, the lipid packing and transition temperature affected by the structure of the hydrophobic lipid tails should not be over looked.

3.2 Experimental Details

3.2.1 Sample Preparation

3.2.1.1 Monomeric bR in Triton X-100 Micelle

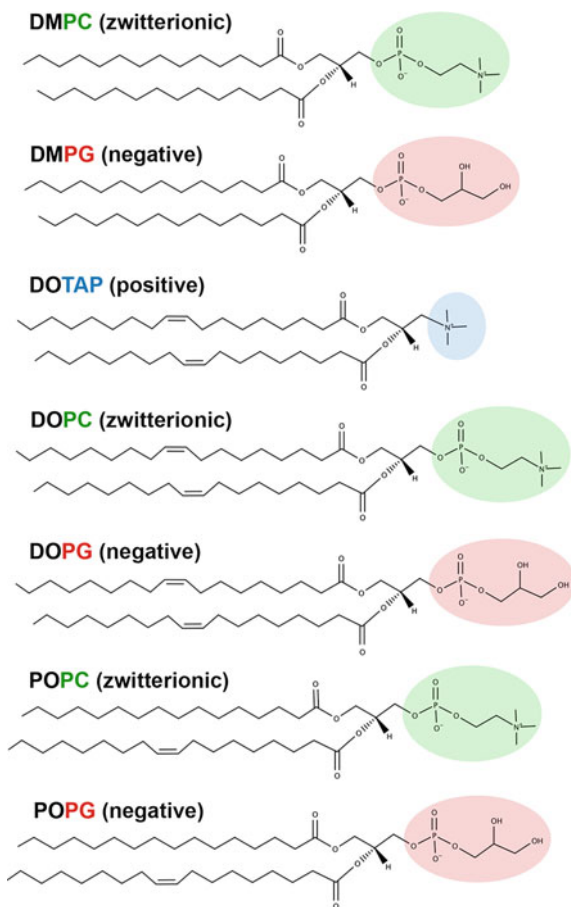
The purple membrane (PM) of *Halobacterium salinarum* S9 strain was harvested and purified following a standard method described in Sect. 2.7. The detergent solubilized monomeric bR (mbR) was prepared by mixing purified PM with detergent Triton X-100 at a ratio of 1 to 7 (w/w) [17], and the solubilization process was kept in dark environment for 72 h at 25 °C. After the solubilization process was complete, mbR was collected from the supernatants after three centrifugations at $18,400 \times g$ for 30 min. The steady state absorption contour maximum of the light adapted mbR in detergent micelle shifted from 568 to 553 nm.

3.2.1.2 Nanodisc Assembly

The synthetic lipids used to assemble the nanodisc are shown in Fig. 3.1. DMPC (1,2-dimyristoyl-sn-glycero-3-phosphocholine), DMPG (1,2-dimyristoyl-sn-glycero-3-phospho-[1'-rac-glycerol]), DOPC (1,2-dioleoyl-sn-glycero-3-phosphocholine), DOPG (1,2-dioleoyl-sn-glycero-3-phospho-[1'-rac-glycerol]), DOTAP (1,2-dioleoyl-3-tri-methylammonium-propane), POPC (1-palmitoyl-2-oleoyl-sn-glycero-3-phosphocholine) and POPG (1-palmitoyl-2-oleoyl-sn-glycero-3-phospho-[1'-rac-glycerol]) were purchased from Avanti Polar Lipids, Inc. and were solubilized to stock solution using buffer solution containing Triton X-100. The concentrations of the lipids and Triton X-100 in the stock solution were 50 mM and 200 mM, respectively, and were used to make different molar ratios of DOPC/DOPG, DMPC/DMPG, DMPC/DOPG, DOPC/DOTAP and POPC/POPG mixtures. The assembly of nanodisc was outlined in Sect. 2.6, with the final molar ratios between bR, MSP and lipids shown in Table 3.1. The molar ratios of MSP to each different lipid mixture have been optimized prior to the study. After BioBeads are removed from the assembly mixture, the sample was centrifuged at 15000 rpm to remove further aggregates and precipitation, before moving on to purification using chromatography methods.

After purification, the bR embedded nanodisc samples were collected, condensed and exchanged into relevant buffers before proceeding to optical and functional characterizations. For bR embedded in nanodisc composed of DMPG/DMPC, DOPG/DOPC and DOPG/DMPC, the buffer contained 0.5x phosphate saline buffer with an additional 100 mM NaCl at pH 5.8 and the concentration of the bR embedded nanodisc was maintained at 10 μ M. For bR embedded in nanodisc composed of DOTAP/DOPC, DOPG/DOPC and POPG/POPC, the buffer contained 50 mM NaCl at pH 7, adjusted by careful addition of HCl or NaOH, and the concentration was diluted to 5 μ M.

Fig. 3.1 The molecular structures of synthetic lipids used in the nanodisc assembly. The charges of the hydrophilic heads are represented in different colors: zwitterionic (green), negative (red) and positive (blue)



3.2.2 Sample Characterization

3.2.2.1 Size and Assembly

Size Exclusion Chromatography. The size exclusion chromatography was performed with either a HiLoad 16/600 Superdex 200 PG column or a Superdex 200 10/300 GL column (GE Healthcare) depending on the volume of the sample and concentration for optimum separation. The assembled nanodisc samples were condensed to the appropriate volume if necessary, using a Centrifugal Concentrator (Vivaspin), and was applied onto the column at 4 °C.

SDS PAGE. The samples collected from size exclusion chromatography were exchanged into distilled water to remove the salt content before the solution was

Table 3.1 Molar ratios of lipid to bR in different bR embedded nanodisc assemblies

	100/0	75/25	50/50	25/75	10/90	0/100
DMPG/DMPC						
Lipid:MSP	50:1	50:1	60:1	67:1	–	90:1
MSP:bR	6:1	6:1	6:1	6:1	–	8:1
DOPG/DOPC						
Lipid:MSP	40:1	40:1	47:1	65:1	65:1	70:1
MSP:bR	6:1	6:1	6:1	6:1	6:1	6:1
DOPG/DMPC						
Lipid:MSP	40:1	50:1	55:1	70:1	–	90:1
MSP:bR	6:1	6:1	6:1	6:1	–	6:1
DOTAP/DOPC						
Lipid:MSP	–	–	–	–	65:1	–
MSP:bR	–	–	–	–	6:1	–
POPG/POPC						
Lipid:MSP	35:1	–	40:1	–	85:1	–
MSP:bR	6:1	–	6:1	–	6:1	–

removed using Savant SPD111 V SpeedVac (Thermo Fisher) at 40 °C for more than 2 h. The dried sample was rehydrated in SDS PAGE loading dye and urea.

Matrix Assisted Laser Desorption Ionization Time of Flight (MALDI-TOF) Mass Spectroscopy. Sample fractions from size exclusion chromatography were collected and combined. The salt buffer in the sample was removed by exchanging the sample into distilled water using Centrifugal Concentrator (Vivaspin), before addition of organic solvent mixture of acetone and methanol at a ratio of 7–1, respectively. The sample mixture containing organic solvent was rested on ice for 1.5 h. Protein precipitate was obtained after fast centrifuge, and was dissolved using trifluoroacetic acid (TFA). The dissolved sample was then mixed with DHB matrix mixture before the mass spectroscopy experiment.

3.2.2.2 Surface Charge

Anionic Exchange Chromatography. The anionic exchange chromatography was performed using a Resource Q anion exchange column (GE Healthcare). The sample was eluted from the column with a linearly increased salt concentration from 0 to 1 M NaCl, and in some cases an increasing pH from pH 6.5 to pH 8, in elution buffer containing 25 mM Tris-HCl and 0.5 mM EDTA. The sample elution was monitored using 280 nm absorption.

Zeta Potential Measurements. The cuvette used to analyse zeta potential was equipped with carbon electrodes. The concentration of samples were diluted and maintained at 1.1 μ M, while the temperature was monitored at 25 °C.

3.2.2.3 Oligomeric State and Retinal State

Circular Dichroism Spectroscopy. The circular dichroism (CD) spectra were recorded with a model No. J-815 spectrometer (JASCO), averaged for 1.2 s at 1 nm intervals between 700 and 400 nm at 28 °C. The path length of the cuvette was 1 cm.

Steady state Absorption Spectroscopy. The steady state UV-Vis absorption spectra were recorded with a model No. USB4000-UV-VIS spectrometer (Ocean Optics) at room temperature. The cuvette used for the steady state absorption spectroscopy was the same as in CD experiments.

3.2.2.4 Photocycle Kinetics

Time-resolved Absorption Spectroscopy. The transient absorption spectroscopy was performed at 25 °C using a temperature monitor, where the concentration of sample was maintained at 10 μM prior to the laser excitation. An appropriate excitation repetition rate was optimized and carefully selected for each bR embedded nanodisc sample depending on the overall photocycle lifetime, shown in Table 3.2. Temporal profiles upon 550–1200 laser excitations, also stated in Table 3.2, were averaged to increase the signal to noise ratio.

Time-resolved Photoelectric Measurements. The concentration of bR embedded nanodisc was kept at 5 μM using 50 mM NaCl in the working half-cell, and the reference half-cell contained only 50 mM NaCl. 240 μl of solutions were injected in the each of the half cells. The laser flux was controlled at 0.5 mJ cm^{-2} , and the repetition rate of 2 Hz. The temporal profiles of photocurrent averaged over 200 laser excitations.

Table 3.2 Repetition rates of the 532 nm excitation pulse for various bR samples for time-resolved difference spectrum acquisitions

	100/0	75/25	50/50	25/76	100/0
DMPG/DMPC					
Repetition rate/Hz	5	2	2	1	0.5
Number of averages	1200	1200	1200	600	550
DOPG/DOPC					
Repetition rate/Hz	5	5	5	5	2
Number of averages	1100	1200	1200	1200	1200
DOPG/DMPC					
Repetition rate/Hz	5	5	5	2.5	0.5
Number of averages	1100	1100	1100	1100	550

3.3 Results and Discussion

The bR embedded nanodisc samples were characterised using chromatography methods as well as optical experiments. Anionic exchange chromatography was used to characterize the surface charge of the nanodisc samples, while size exclusion chromatography determined the size of the nanodiscs. Steady state spectroscopy was performed to examine the confirmations of the retinal pocket of bR, and visible wavelength circular dichroism was used to inspect the oligomeric state of bR in nanodisc. The photocycle kinetics of bR in nanodisc with different lipid composition was studied using time-resolved difference spectra, and the kinetics of the release of proton by bR into the bulk solution was investigated using time-resolved photoelectric measurements.

3.3.1 Sizes, Oligomeric State and Surface Charge

The sizes of bR embedded lipid nanodisc were estimated to be 140 ± 25 kDa using size exclusion chromatography. The estimation was achieved by creating a relationship between elution volume from the size exclusion column and protein molecular size of standard samples.

The sample collected from size exclusion then underwent MALDI-TOF mass spectroscopy and SDS-PAGE for verification, shown in Fig. 3.2. MALDI-TOF mass spectra showed two major peaks, with molecular weights identified as bR and MSP1E3D1. In 5–13% SDS PAGE, the fractions collected from size exclusion chromatography showed two bands, identified as bR, MSP1E3D1 and MSP1E3D1 (-), which is the MSP1E3D1 without its histidine tag. Moreover, the intensities of the bands across the different fractions showed agreement to the intensity of the peak of which the fraction was taken, suggesting the peak was homogeneous and singular.

The circular dichroism was performed to verify the oligomeric state of bR embedded in nanodisc. Shown in Fig. 3.3, bR embedded in nanodisc consisting of DMPG/DMPC, DOPG/DOPC and DOPG/DMPC all at 50/50 displayed clear monophasic feature in the visible light range. Compared to the biphasic peaks of trimeric bR in PM, the monophasic feature indicated bR embedded in nanodisc to be monomeric rather than trimeric. Moreover, we found that despite reports of oligomeric state of bR being influenced by the bR to lipid ratio, as PC lipid was substituted with PG lipids and the number of lipids to MSP decreased, bR embedded in nanodisc maintained the monomeric form. This eliminates the trimeric coupling effect in functional studies.

The ionic exchange chromatography profiles of the nanodisc assembled are shown in Figs. 3.4, 3.5 and 3.6. Samples of empty nanodisc and bR embedded nanodisc of DMPG/DMPC, DOPG/DOPC and DOPG/DMPC were eluted from Resource Q column with a linearly increasing gradient of NaCl concentration and

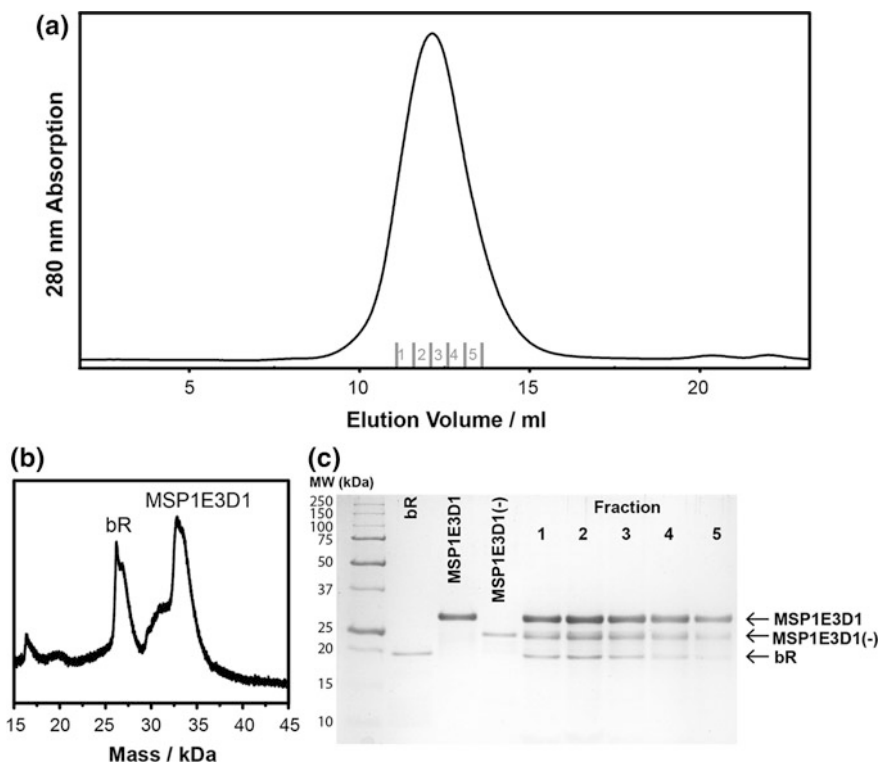
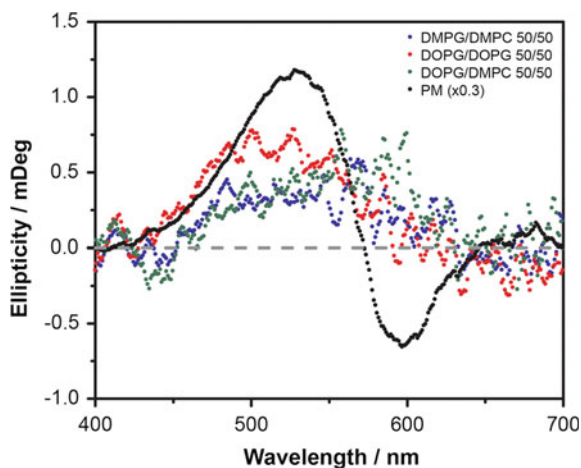


Fig. 3.2 a Size exclusion chromatography profile of bR embedded nanodisc composed of DOPG/DOPC 10/90. b MALDI-TOF mass spectrum and c SDS PAGE of fractions taken from the size exclusion chromatography profiles shown in (a). Reproduced with permission from Ref. [22], copyright Elsevier 2015

Fig. 3.3 Circular dichroism spectra of (black) bR in PM and bR embedded in nanodiscs consisting of PC/PG 50/50. The lipid compositions of the nanodiscs are DMPG/DMPC (blue), DOPG/DOPC (red) and DOPG/DMPC (green). The ellipticity of bR in PM was scaled to 30% to showcase the biphasic feature in comparison. Reproduced with permission from Ref.[22], copyright Elsevier 2015



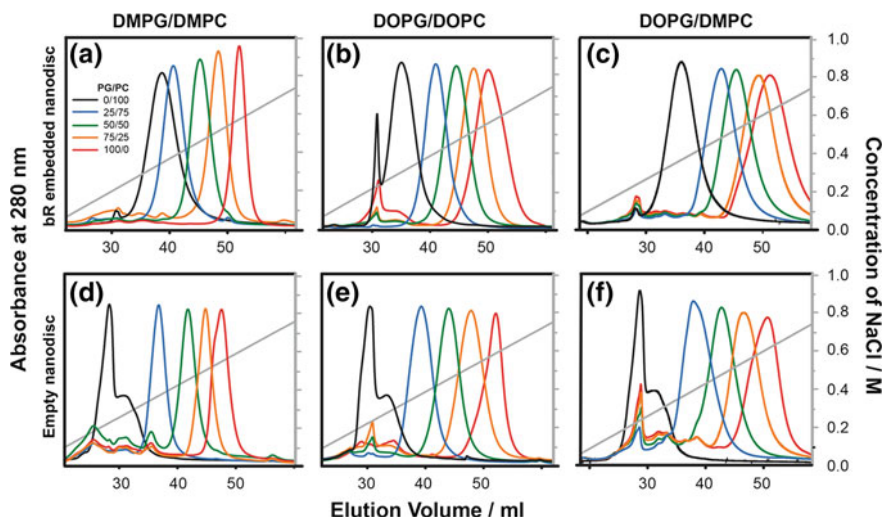


Fig. 3.4 Anionic exchange chromatography profile of **a–c** bR embedded nanodisc and **d–f** empty nanodisc, composed of **a, d** DMPG/DMPC, **b, e** DOPG/DOPC and **c, f** DOPG/DMPC. The molar ratio of the PG/PC lipids are 0/100 (black), 25/75 (blue), 50/50 (green), 75/25 (orange) and 100/0 (red). The NaCl linear gradient that was used to elute the sample is shown in grey. Adapted and reproduced with permission from Ref. [22], copyright Elsevier 2015

pH, represented by the grey lines. In both the case of bR embedded nanodisc (**a–c**) and empty nanodisc (**d–f**), the nanodisc with higher DMPG or DOPG contents resulted in greater elution volume and a higher salt concentration. Since in anionic exchange chromatography a greater elution volume with a greater salt concentration indicates a greater negative surface charge, the results shown in Fig. 3.4 suggest an increase of DMPG or DOPG content increases the negative surface charge.

Moreover the zeta potential analyses shown in Fig. 3.5, showed agreement to the trend found in ionic exchange chromatography profiles, with the increase in negative surface charge as the PG lipid content in nanodisc was increased. This phenomenon is due to the negatively charged hydrophilic head of PG. The zeta potential of PM at pH 7.5 was reported to be 52.0 ± 1.2 mV [18] and between -15 and -20 mV at pH 5.8 [19]. By comparing the ionic exchange profiles and zeta potentials of bR embedded nanodisc and empty nanodisc of the same lipid composition, the incorporation of monomeric bR into nanodisc slightly increases the negative surface charges. This suggests that monomeric bR has intrinsic negative surface charge and therefore played a small role in changing the surface charge of the nanodiscs.

Figure 3.6 shows the anionic exchange chromatography of bR embedded in DOTAP/DOPC, DOPG/DOPC and POPG/POPG. Unlike in Fig. 3.4, the elution buffer contained only a linearly increasing NaCl concentration and no increasing pH, while the pH remained at pH8. This was due to the fact that DOTAP/DOPC 10/90 sample contained less negative surface charge and the initial pH 6.5 caused the

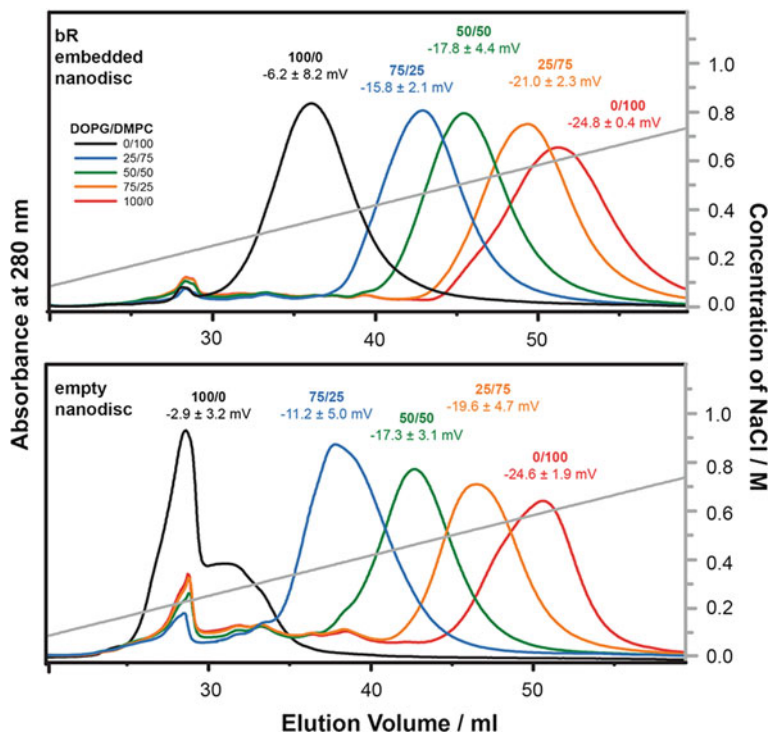


Fig. 3.5 Anionic exchange chromatography profile and zeta potentials of bR embedded nanodisc (above) and empty nanodisc (below), composed of DOPG/DMPC lipids, at molar ratio of 0/100 (black), 25/75 (blue), 50/50 (green), 75/25 (orange) and 100/0 (red). The NaCl linear gradient that was used to elute the sample is shown in grey. Adapted and reproduced with permission from Ref. [22], copyright Elsevier 2015

sample to only weakly interact with the anion exchange resin. Since the elution of samples was still governed by the increase in NaCl concentration, the trend of increasing PG content in nanodisc increases the overall surface charge was also found in Fig. 3.6.

3.3.2 Steady State Absorption and CD Spectroscopy

The purified PM showed a characteristic absorption band at 563 nm, and the detergent solubilized mbR showed a shift to 553 nm. Shown in Fig. 3.7, the absorption contours of bR embedded nanodisc shows an absorption band at 560 nm. The peak around 660 nm is a known artefact from the UV-Vis light source. No additional absorption band was observed at 390 nm, suggesting no hydrolysis of retinal had taken place in the different lipid environment.

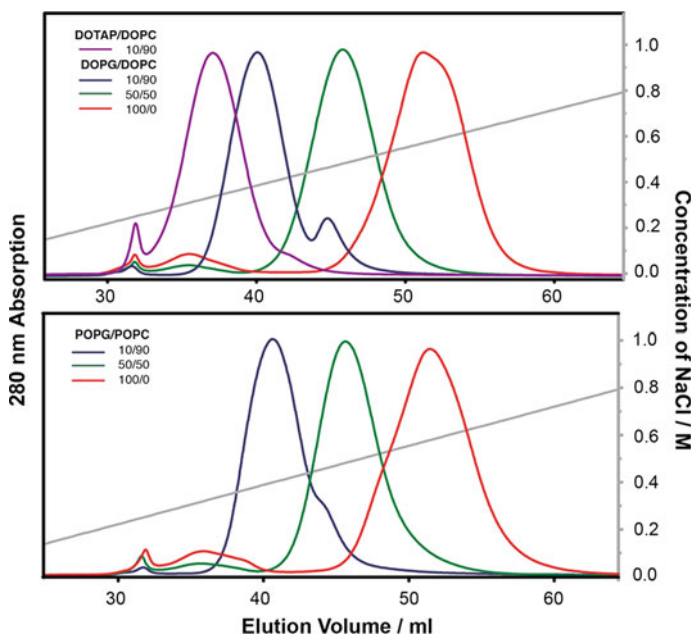
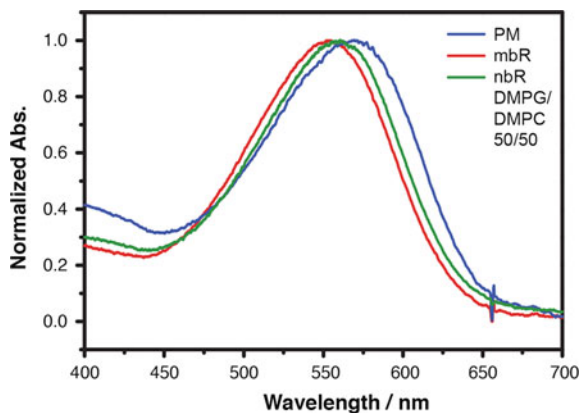


Fig. 3.6 Anionic exchange chromatography profiles of bR embedded in nanodisc consisted of DOTAP/DOPC and DOPG/DOPC (above) and POPG/POPC (below). The molar ratio of the lipids is DOTAP/DOPC 90/10 (purple), or PG/PC with 10/90 (navy), 50/50 (green) and 100/0 (red). The NaCl linear gradient that was used to elute the sample is shown in grey Adapted and reproduced with permission from Ref. [23] from The Royal Society of Chemistry

Fig. 3.7 Steady state absorption spectra of PM (blue), mbR (red) and bR embedded in nanodisc (green) consisted of DMPG/DMPC at molar ratio of 50/50. The sample was light Adapted for at least 30 min, and the concentration was controlled at about 10 μ M



Shown in Figs. 3.8 and 3.9 are the steady state absorption contours of bR embedded in nanodisc composed of DMPG/DMPC, DOPG/DOPC, DOPG/DMPC, DOTAP/DOPC and POPG/POPC lipids at different ratios. The shift of bR embedded in nanodisc in the absorption contour observed in Fig. 3.7 was found to

Fig. 3.8 Steady state absorption spectra of bR embedded in nanodisc consisting of **a** DMPG/DMPC, **b** DOPG/DOPC and **c** DOPG/DMPC. The molar ratios of PG/PC lipids are shown as 0/100 (black), 25/75 (blue), 50/50 (green), 75/25 (orange) and 100/0 (red). The samples are in buffer consisted of 0.5x PBS with additional 100 mM NaCl at pH 5.8. Adapted and reproduced with permission from Ref. [22], copyright Elsevier 2015

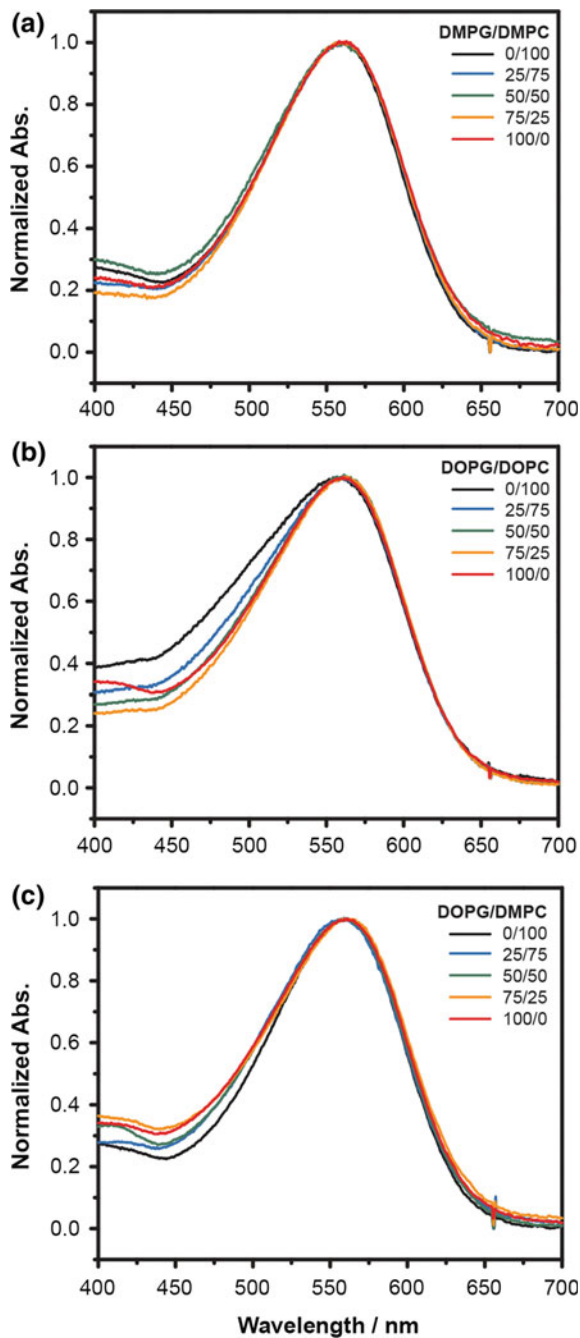
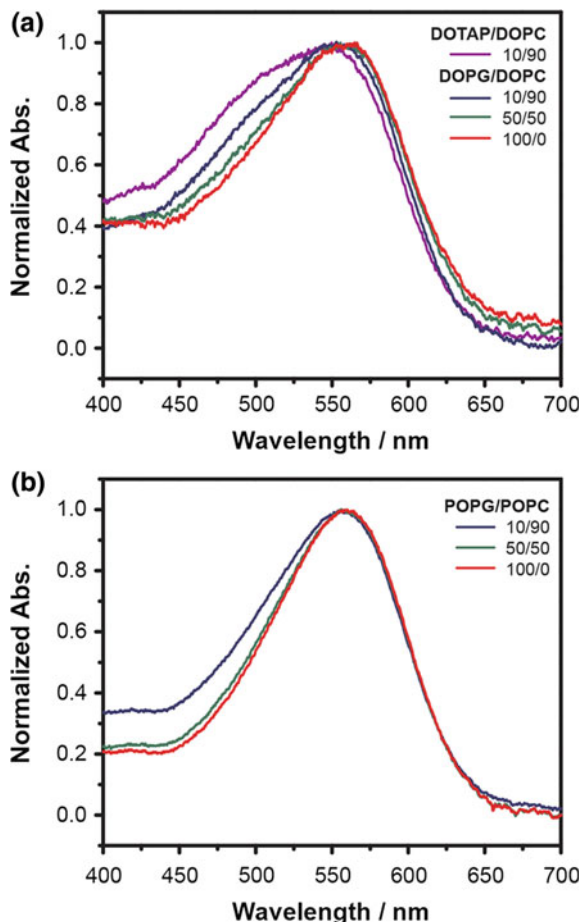


Fig. 3.9 Steady state absorption spectra of bR embedded in nanodisc consisting of **a** DOTAP/DOPC and DOPG/DOPC, and **b** POPG/POPC. The molar ratio of DOTAP/DOPC is 10/90 (purple), and the PG/PC lipids are shown as 10/90 (navy) 50/50 (green) and 100/0 (red). The samples are in buffer consisting of 100 mM NaCl at pH 7. Adapted and reproduced with permission from Ref.[23], from The Royal Society of Chemistry



be almost independent of lipid composition and buffer conditions, suggesting the retinal pocket of bR is not significantly affected by lipid composition and only by the structure of surrounding lipid environment.

In the case of lipids with two unsaturated hydrocarbon tails (DO) or only one unsaturated hydrocarbon tail (PO), a minor blue shift can be observed as the zwitterionic or positive lipid content is increased. This could be due to an alteration of the population of the different states of retinal in the bR interior in nanodiscs of different lipid compositions. In particular, the blue shift could be attributed to the decrease in retinal with all-*trans* population and an increase in the 13-*cis* conformation [20].

3.3.3 Time Resolved Difference Spectra

The time-resolved difference spectrum measures the changes in absorption of a particular wavelength of bR with respect to time after the photocycle was initiated with a pulsed laser at 532 nm. By selecting different observation wavelengths the experiment was designed to monitor not only the recovering of the parent state, which measures the overall photocycle duration, but also the lifetime of the intermediate states.

Before the difference spectra could be collected, it was important to optimize the repetition rate of the excitation laser to avoid overshooting or distortion due to incomplete photocycles. Shown in Fig. 3.10, the repetition optimization for each bR embedded nanodisc monitored the recovery parent state at 560 nm. In the case of complete photocycle within the duration between each excitation pulses the recovery curve would overlap. As the photocycle began to fail to complete within the duration between the excitation pulses, the recovery curve, though seeming to

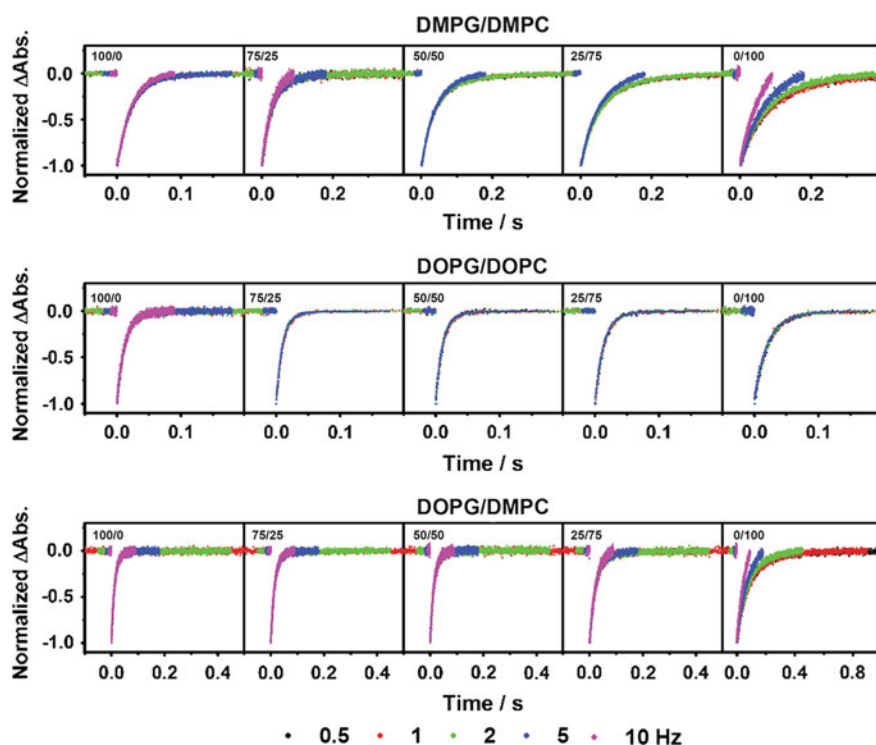


Fig. 3.10 Normalized temporal profiles for repetition optimization of the recovery of bR at 560 nm upon 532 nm excitation pulses of bR in nanodisc of different lipid composition. The repetition rates are 0.5 Hz (black), 1 Hz (red), 2 Hz (green), 5 Hz (blue) and 10 Hz (purple). Reproduced with permission from Ref. [22], copyright Elsevier 2015

return to zero indicating a return to the parent state, would become distorted and fail to successfully overlap with the recovery curves using a slower repetition rate. For example, with bR embedded in nanodisc composed of DMPG/DMPC 100/0, the 560 nm recovery curve of 5 Hz excitation repetition overlapped with recovery curves from 0.5, 1 and 2 Hz repetition rate, however at 10 Hz the recovery curve became distorted. This suggested the optimum excitation repetition for bR embedded in DMPG/DMPC 100/0 would be 5 Hz. The final repetition rates for transient absorption spectra for each bR embedded in nanodisc samples are listed in Table 3.2.

By looking at the recovery of the parent state at 560 nm after excitation, shown in Fig. 3.11, the duration of the overall photocycle was characterised. In all the cases of lipids with either saturated hydrocarbon tails (DM), unsaturated hydrocarbon tails (DO) or a mixture of the two, the increase in PG lipid content significantly increased the recovery rate of bR parent state, therefore resulting in a decrease in photocycle lifetime. By analysing the native lipid composition in PM, the percentages of PGP-Me, PG and PGS is about 40% [21]. Shown in Fig. 3.11 the increase of recovery rate of bR embedded in nanodisc reaches a maximum as PG content exceeds 50%, which shows agreement to the native composition and biological conditions.

Moreover, by comparing Fig. 3.11a and b, the changes in photocycle across the different surface charges of nanodisc are more observable in DM lipid tails compared to DO lipid tails. This suggests not only would the charge of hydrophilic lipid head significantly affect the rate of the photocycle and thus, the rate of the proton pump, but the structure of the hydrophobic hydrocarbon chain might also have an effect. With the differences in the recovery of the bR parent state observed, it is clear that the photocycle kinetics of bR is strongly influenced by the different nanodisc environments. In order to investigate the effect of the lipid further, the entire photocycle activities of bR embedded in nanodisc of different lipid nanodisc, such as the different intermediate states, were characterized.

Time-resolved difference absorption spectroscopy was performed across a range of wavelengths. The experiment was performed to probe from 380 to 710 nm upon 532 nm excitation pulses, thus recording the proton translocation and retinal re-isomerization by observing the transition from intermediate M state and to the following intermediate states. The time-resolved full-wavelength difference spectra of monomeric bR embedded in nanodisc of different lipid composition are shown in Fig. 3.12, with the untruncated spectra shown in Fig. 3.13. The upward (rise of intermediate state) and downward (decay from parent state) features in the difference spectra were shown in red and blue, respectively. The contours of the full-wavelength difference spectra showed the depletion of the parent state at 560 nm (downward), rise of the intermediate state M at 410 nm (upward), the intermediate state N characterized by asymmetric recovery at 450–500 nm (downward) and the intermediate state O at 650 nm (upwards). In the cases of bR in nanodisc containing high (>50%) PG contents, the intermediates N and O are

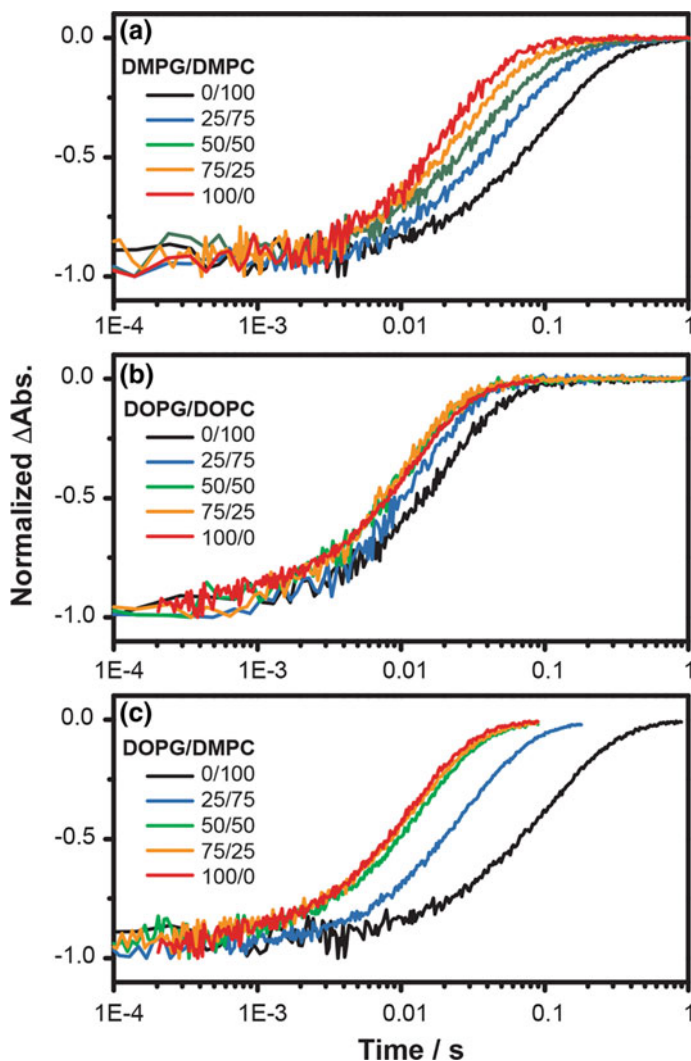


Fig. 3.11 Normalized temporal profiles of the recovery of bR depletion at 560 nm upon 532 nm excitation of monomeric bR embedded in nanodisc of different lipid composition. The nanodisc consisted of **a** DMPG/DMPC, **b** DOPG/DOPC and **c** DOPG/DMPC, with PG/PC molar ratios of 0/100 (black), 25/75 (blue), 50/50 (green), 75/25 (orange) and 100/0 (red). Adapted and reproduced with permission from Ref. [22], copyright Elsevier 2015

strongly preserved. Not only does this suggest a conventional photocycle pathway, bR embedded in nanodisc containing high PG contents also displayed a faster photocycle lifetime and shorter intermediate state lifetime, showing similarities to native bR behaviour compared to bR embedded in nanodisc containing higher PC contents. For bR embedding in nanodisc of higher PC contents, the photocycle

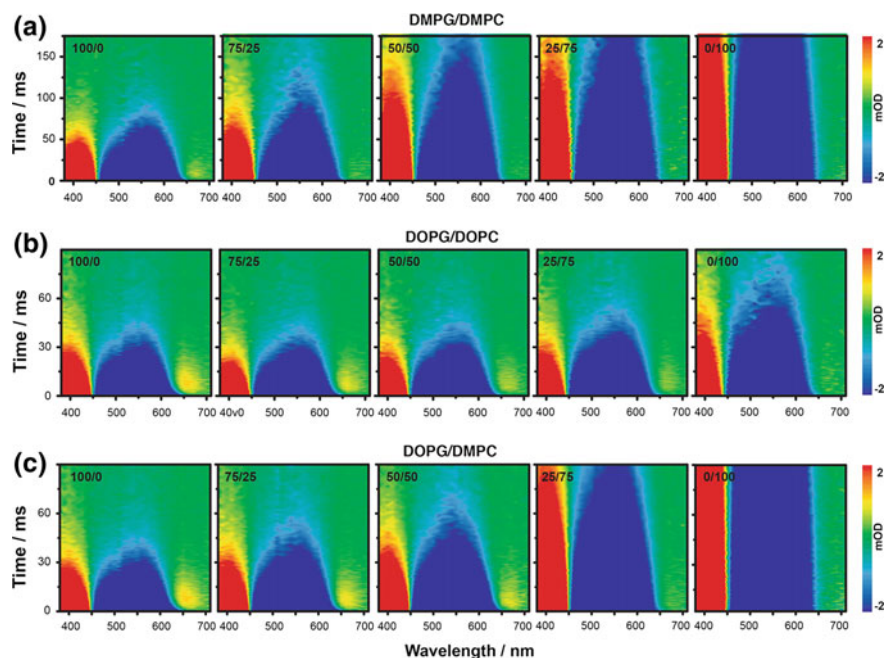


Fig. 3.12 Time-resolved difference absorption spectra in two-dimension contours of monomeric bR in nanodisc consisting of **a** DMPG/DMPC, **b** DOPG/DOPC and **c** DOPG/DMPC upon excitation with 532 nm pulsed laser. Adapted and reproduced with permission from Ref. [22], copyright Elsevier 2015

lifetime increases as the amount of PC content increases, while the population of intermediate states N and O decreases. In the cases of higher PC contents, the difference spectra showed two symmetrical features, an upwards feature at 410 nm denoting the M intermediate states and a downward feature at 560 nm denoting a depletion of parent state. These features suggested bR embedded in nanodisc with lower PG content undergoes an altered pathway rather than the conventional photocycle, and that the transition from the M intermediate returns to the parent ground state without going through N or O states.

Furthermore, the difference in photocycle kinetics in the parent state recoveries between bR embedded in nanodisc consisted of saturated hydrocarbon tails, and those consisted of unsaturated hydrocarbon tails observed in Fig. 3.11 are also apparent in the full-wavelength difference spectra. Comparing bR embedded in nanodisc composed of only DMPG and those composed of only DOPG (PG/PC 100/0) in Figs. 3.12 and 3.13, the transient absorption contours showed distinct differences. Particularly, the population of intermediate O state appeared to be significantly less in bR embedded in nanodisc composed of only DMPG compared to DOPG. Also, the rate of the photocycle of bR embedded in nanodisc composed

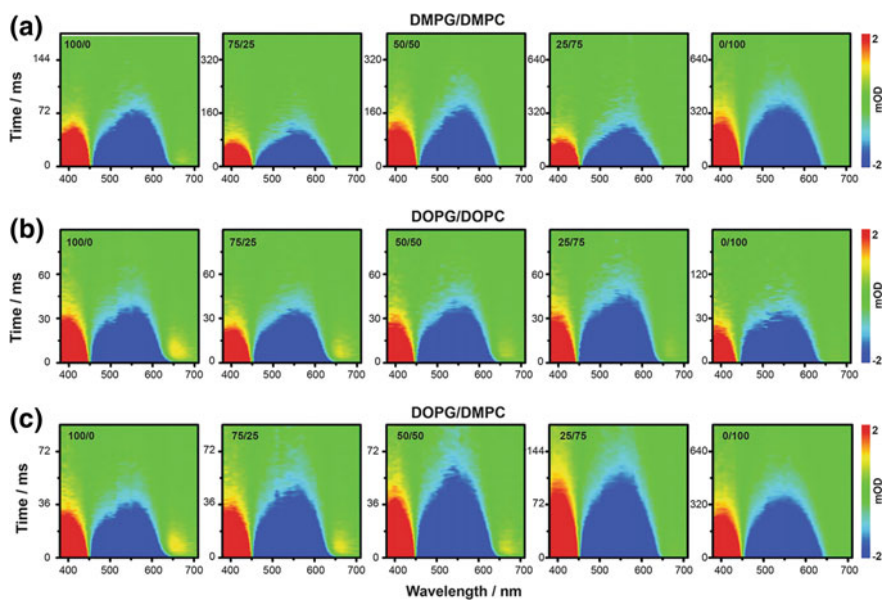


Fig. 3.13 Untruncated time-resolved difference absorption spectra in two-dimension contours of monomeric bR in nanodisc consisting of **a** DMPG/DMPC, **b** DOPG/DOPC and **c** DOPG/DMPC upon excitation with 532 nm pulsed laser. Adapted and reproduced with permission from Ref. [22], copyright Elsevier 2015

of only DMPG was found to be longer than DOPG. The distinction in photocycle lifetime is more significant in the cases of bR embedded in nanodisc composed of only DMPC lipid and only DOPC lipid. Such differences caused by the different hydrocarbon chains could arise from variety of different properties. The melting points of the lipids might be a factor in the alteration of photocycle kinetics. The experiments were performed at 25 °C, and melting temperatures of DMPG (23 °C) and DMPC (24 °C) are much higher than that of DOPG (−18 °C) and DOPC (−17 °C). The difference in the structure and in the length of the lipid tails might affect the packing of the nanodisc, considering the difference in the optimized number of lipids per disc. It is therefore reasonable to conclude that the lipid tail can have a moderate influence on the photocycle kinetics, while the effects of the charge of the lipid head are more significant.

With the knowledge of the general patterns, full-wavelength transient absorption experiments can be simplified to only observing parent state recovery at 560 nm, M state intermediate at 410 nm and O state intermediate at 650 nm. Shown in Figs. 3.14 and 3.15 are the temporal profiles of bR embedded in nanodisc composed of DOTAP/DOPC, DOPG/DOPC and POPG/POPC lipids at different molar ratios. Figure 3.14 shows the weighted temporal profile where the observed temporal profiles were divided by the optical density of the steady state absorption spectra at 532 nm, the excitation wavelength, to eliminate small deviation of the

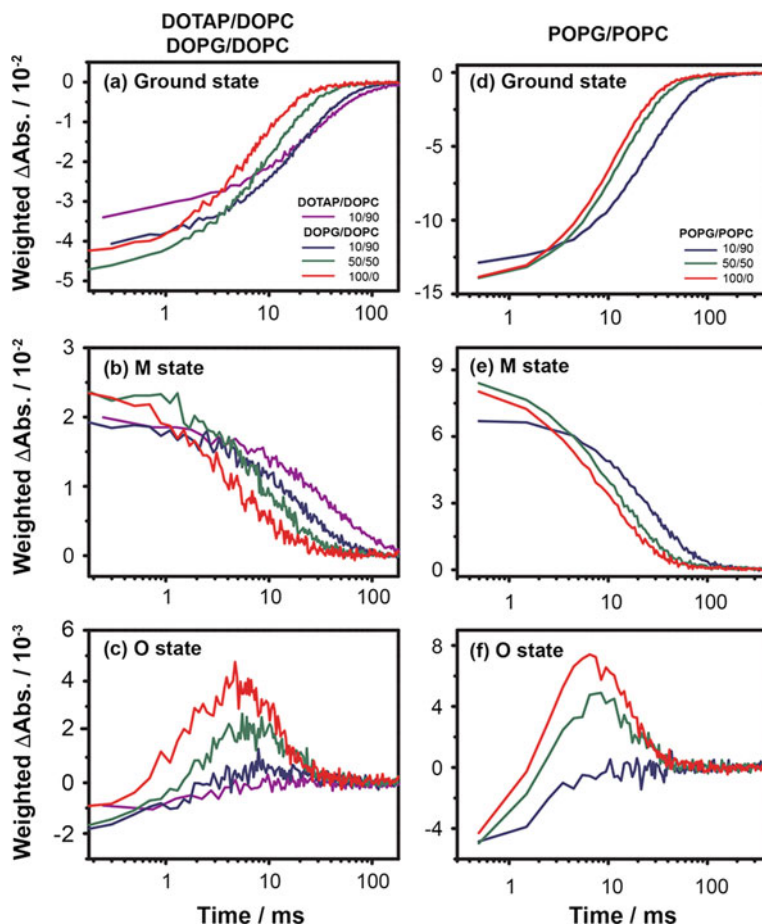


Fig. 3.14 Weighted temporal profiles of (a, d) recovery of bR depletion at 560 nm, (b, e) intermediate M state at 410 nm and (c, f) intermediate O state at 650 nm upon 532 nm excitation laser of bR embedded in nanodisc consisting of (a–c) DOTAP/DOPC and DOPG/DOPC and (d–f) POPG/POPC. The molar ratio of DOTAP/DOPC is 10/90 (purple), and molar ratios of PG/PC are 10/90 (navy), 50/50 (green) and 100/0 (red). Adapted and reproduced with permission from Ref. [23], from The Royal Society of Chemistry

sample concentration, whereas Fig. 3.15 shows the normalized temporal profiles for parent state recovery and M state intermediate. As anticipated, the rate of recovery of the parent state at 560 nm decreased as the PG content was decreased. The lifetime of intermediate state M increased as the PG content was reduced, while the population of intermediate state O intermediate reduced, consistent with the previous findings.

Weighted profiles of parent state recovery in Fig. 3.14a and d show a decrease in the maximum absorbance as the neutral and positive lipid content of the nanodisc

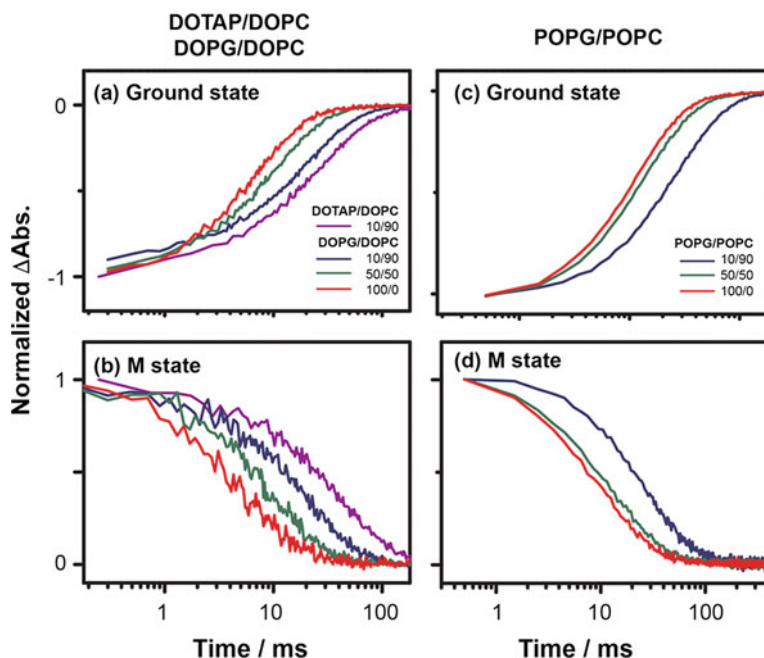


Fig. 3.15 Normalized temporal profiles of **a, c** recovery of bR depletion at 560 nm and **b, d** intermediate M state at 410 upon 532 nm excitation laser of bR embedded in nanodisc consisting of **(a–c)** DOTAP/DOPC and DOPG/DOPC and **(d–f)** POPG/POPC. The molar ratio of DOTAP/DOPC is 10/90 (purple), and molar ratios of PG/PC are 10/90 (navy), 50/50 (green) and 100/0 (red). Adapted and reproduced with permission from Ref. [23], from The Royal Society of Chemistry

increases, showing agreement to the minor decrease in the population of the photocycle active all-*trans* retinal.

3.3.4 Transient Photocurrent Measurements

Photocurrent is generated by the release of a proton to the exterior by bR after excitation pulse, thus by measuring the time-resolved photocurrent it is possible to measure the changes in free proton population due to release of a proton from the protein to the bulk solution during the photocycle. The temporal profiles of the photocurrent of bR embedded in nanodisc composed of DO and PO lipids are shown in Fig. 3.16, both weighted and normalized. The waveform across the different nanodisc sample displayed similar shapes, however the magnitudes vary depending on the lipid composition of nanodiscs. As the PG content was reduced, the maximum intensity of the photocurrent increased, suggesting a great population of free protons are released into the bulk solution after 532 nm excitation pulses.

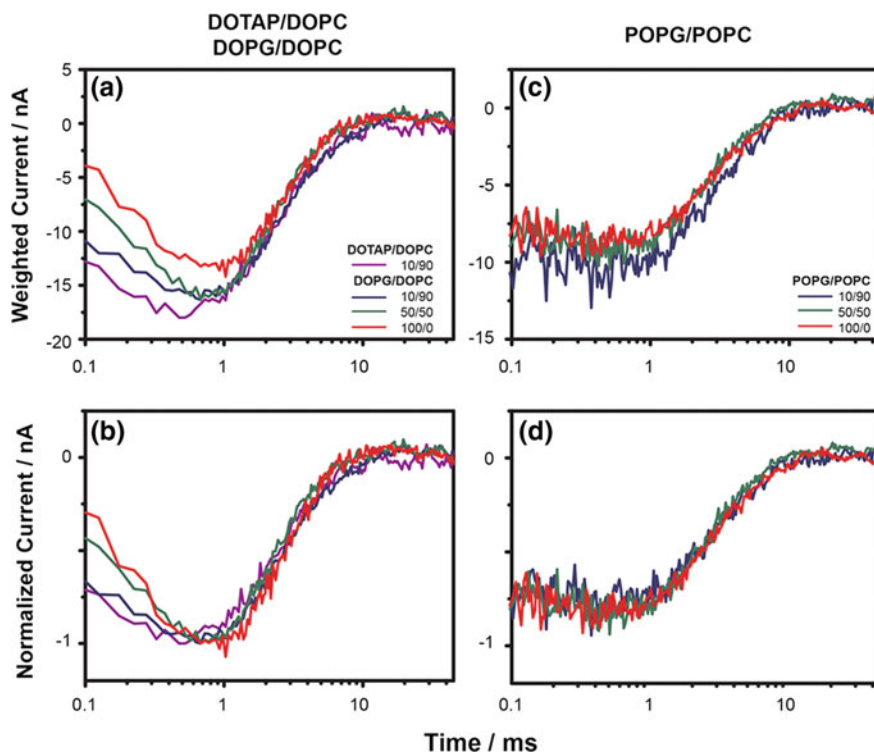


Fig. 3.16 **a, c** Weighted and **b, d** normalized temporal profiles of the photocurrent upon 532 nm excitation of bR embedded in nanodiscs consisting of **(a, b)** DOTAP/DOPC and DOPG/DOPC or **(c, d)** POPG/POPC. The molar ratio of DOTAP/DOPC is 10/90 (purple), and molar ratio of PG/PC are 10/90 (navy), 50/50 (green) and 100/0 (red). Adapted and reproduced with permission from Ref. [23], from The Royal Society of Chemistry

From the steady state absorption spectra shown in Fig. 3.9, as the PG content was reduced the characteristic absorption peak underwent a minor blue shift, which could be caused by a decrease in all-trans retinal suggesting a decrease in photocycle active population. This was further supported by a decrease in the intensity of the depleted bR parent state, observed in weighted transient absorption spectra shown in Fig. 3.14. With a decrease in photocycle active bR population, it is therefore reasonable to expect bR embedded in nanodisc composed of neutral or positive lipids to exhibit a weakened photocurrent, since the photocurrent is related to the release of proton by bR during the photocycle. However, the magnitudes of photocurrent produced by bR embedded in nanodisc composed DOTAP/DOPC 10/90, which consisted of positive and zwitterionic hydrophilic lipid heads, was shown to be greater than bR embedded in nanodisc composed of DOPG/DOPC. This trend was also observed in the case of bR embedded in POPG/POPC nanodiscs, suggesting that the effect was predominantly governed by the charge of the hydrophilic lipid head.

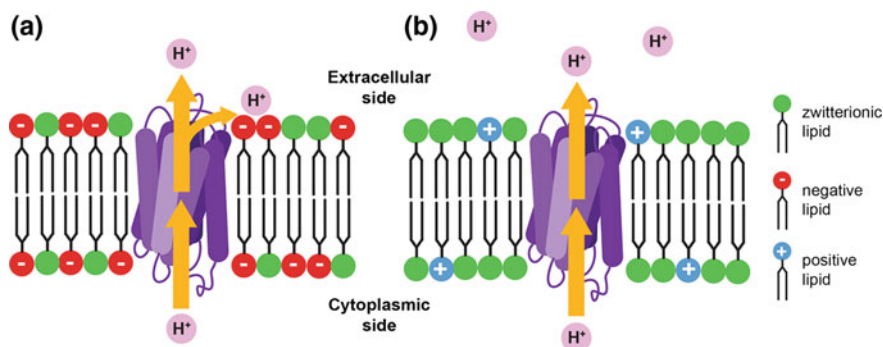


Fig. 3.17 Schematics of the effect of lipids on the release of free proton by bR embedded in nanodisc composed of negatively charged (a) and positively charged lipids (b). The differently charged lipids were shown in different colours: zwitterionic (green), negative (red) and positive (blue) lipid head groups. Adapted with permission from Ref. [23], from The Royal Society of Chemistry

By examining the results, the phenomenon can be explained by the intrinsic property of the hydrophilic head, particularly the fact that hydrophilic lipid heads reside on the surface of the lipid bilayer. After the photo excitation pulse the photocycle is initiated and the retinal begins to change conformation, leading to the proton on the protonated Schiff base to translocate towards the extracellular side through a series of hydrogen bonding networks. As the proton is released by the protein on the extracellular side, if the lipid bilayer surface consists of negatively charged lipid heads, such in the case shown in Fig. 3.17a, the positive free proton would be attracted to the negatively charged lipid heads and thus could be trapped on the surface rather than released into the bulk solution. If however, the surface of the nanodisc is composed of neutral or positively charge lipid heads, shown in Fig. 3.17b, rather than being attracting to and becoming trapped, the proton would be repulsed into the bulk solution resulting in an increase of non-bound protons in the bulk solution and photocurrent magnitude.

3.4 Conclusion

Since its invention, nanodisc has provided an advantageous platform for membrane protein studies for its ability to act as a lipid bilayer membrane mimic. However, while the membrane environment is critical for the stability, the solubility, the structure and the function of some membrane proteins, the lipid composition of such membrane environment can have a crucial effect on the membrane protein.

Demonstrated in this systematic study, the effect of the lipid composition on the function of membrane protein bacteriorhodopsin was elucidated. The size exclusion chromatography, MALDI-TOF mass spectroscopy and SDS PAGE showed bR was

successfully incorporated into nanodisc and circular dichroism spectra showed bR was in monomeric form while embedded on nanodisc. Anionic exchange chromatography and zeta potential measurements showed an increase of negative surface charge as the PG lipid content was increased. Steady state absorption spectroscopy was employed to show the retinal pocket was almost unaffected by the different lipid composition of the nanodisc, with a minor blue shift observed as the PG content was decreased and the positively charged lipid content increased. This minor blue shift can be attributed to a small change in the population of retinal conformation, specifically a small decrease in the photoactive *all-trans* retinal state. Full wavelength transient absorption spectroscopy was used to characterize the photocycle kinetics of bR embedded in nanodisc of different lipid compositions. It was observed that a change in lipid composition, especially the charge of the hydrophilic lipid head, would lead to a significant alternation in the photocycle kinetics of bR. Furthermore, electrochemical measurements showed that the positively charged lipids would assist the release of proton from the protein after translocation, by repulsing the proton into the bulk solution and increasing the population of the non-bound protons during photocycle. The results suggest that negatively charged lipids in the nanodisc would accelerate the photocycle kinetics and trap the proton in the proximity of bR and preserve the electromotive force across the lipid bilayer.

The results presented in this chapter indicate the significant influence of lipid composition on the ion translocation membrane protein, with the lipids having important effects on the function of the protein. Therefore, it is possible to manually tune the function of membrane protein by adjusting the lipid composition of the nanodisc, which can aid and provide greater control when using the appropriate characterization methods. However, the result also implied that while nanodisc provide remarkable advantages in the study of membrane protein, the choice of lipid composition should be carefully considered in order to provide a biologically relevant outcome.

Acknowledgements The results of this chapter were in collaboration with Professor Li-Kang Chu's students from National Tsing Hua University, Hsinchu, Taiwan. In particular, the preparation of monomeric bR in Triton X-100, the steady state absorption spectroscopy, and the single-wavelength transient absorption spectroscopy were performed either by Tsung-Yen Lee or Yin Hsin. The full-wavelength time resolved difference spectra were recorded by Tsung-Yen Lee, and the electrochemical measurement was carried out by Yin Hsin.

References

1. Mitra N (2015) Nanodiscs: membrane protein research in near-native conditions. *Mater Methods*
2. Wadsäter M, Maric S, Simonsen JB et al (2013) The effect of using binary mixtures of zwitterionic and charged lipids on nanodisc formation and stability. *Soft Matter* 9:2329–2337. <https://doi.org/10.1039/C2SM27000E>

3. Dowhan W, Bogdanov M (2009) Lipid-dependent membrane protein topogenesis. *Ann Rev Biochem* 78:515–540. <https://doi.org/10.1146/annurev.biochem.77.060806.091251>
4. Zhang W, Campbell HA, King SC, Dowhan W (2005) Phospholipids as Determinants of membrane protein topology phosphatidylethanolamine is required for the proper topological organization of the γ -aminobutyric acid permease (GabP) of *Escherichia coli*. *J Biol Chem* 280:26032–26038. <https://doi.org/10.1074/jbc.M504929200>
5. Mukhopadhyay AK, Bose S, Hendler RW (1994) Membrane-mediated control of the bacteriorhodopsin photocycle. *Biochemistry (Mosc)* 33:10889–10895
6. Mukhopadhyay AK, Dracheva S, Bose S, Hendler RW (1996) Control of the integral membrane proton pump, bacteriorhodopsin, by purple membrane lipids of *Halobacterium halobium*. *Biochemistry (Mosc)* 35:9245–9252
7. Joshi MK, Dracheva S, Mukhopadhyay AK et al (1998) Importance of specific native lipids in controlling the photocycle of bacteriorhodopsin. *Biochemistry (Mosc)* 37:14463–14470. <https://doi.org/10.1021/bi980965j>
8. Cui J, Kawatake S, Umegawa Y et al (2015) Stereoselective synthesis of the head group of archaeal phospholipid PGP-Me to investigate bacteriorhodopsin–lipid interactions. *Org Biomol Chem* 13:10279–10284. <https://doi.org/10.1039/C5OB01252J>
9. Rigaud J-L, Pitard B, Levy D (1995) Reconstitution of membrane proteins into liposomes: application to energy-transducing membrane proteins. *Biochim Biophys Acta BBA—Bioenerg* 1231:223–246. [https://doi.org/10.1016/0005-2728\(95\)00091-V](https://doi.org/10.1016/0005-2728(95)00091-V)
10. Yoshino M, Kikukawa T, Takahashi H et al (2013) Physicochemical studies of bacteriorhodopsin reconstituted in partially fluorinated phosphatidylcholine bilayers. *J Phys Chem B* 117:5422–5429. <https://doi.org/10.1021/jp311665z>
11. Yokoyama Y, Negishi L, Kitoh T et al (2010) Effect of lipid phase transition on molecular assembly and structural stability of bacteriorhodopsin reconstituted into phosphatidylcholine liposomes with different acyl-chain lengths. *J Phys Chem B* 114:15706–15711. <https://doi.org/10.1021/jp108034n>
12. Bayburt TH, Grinkova YV, Sligar SG (2006) Assembly of single bacteriorhodopsin trimers in bilayer nanodiscs. *Arch Biochem Biophys* 450:215–222. <https://doi.org/10.1016/j.abb.2006.03.013>
13. Wang Z, Bai J, Xu Y (2008) The effect of charged lipids on bacteriorhodopsin membrane reconstitution and its photochemical activities. *Biochem Biophys Res Commun* 371:814–817. <https://doi.org/10.1016/j.bbrc.2008.04.141>
14. Happe M, Teather RM, Overath P et al (1977) Direction of proton translocation in proteoliposomes formed from purple membrane and acidic lipids depends on the pH during reconstitution. *Biochim Biophys Acta BBA—Biomembr* 465:415–420. [https://doi.org/10.1016/0005-2736\(77\)90092-X](https://doi.org/10.1016/0005-2736(77)90092-X)
15. Tunuguntla R, Bangar M, Kim K et al (2013) Lipid bilayer composition can influence the orientation of proteorhodopsin in artificial membranes. *Biophys J* 105:1388–1396. <https://doi.org/10.1016/j.bpj.2013.07.043>
16. Johnson PJM, Halpin A, Morizumi T et al (2014) The photocycle and ultrafast vibrational dynamics of bacteriorhodopsin in lipid nanodiscs. *Phys Chem Chem Phys* 16:21310–21320. <https://doi.org/10.1039/C4CP01826E>
17. Wang J, Link S, Heyes CD, El-Sayed MA (2002) Comparison of the dynamics of the primary events of bacteriorhodopsin in its trimeric and monomeric states. *Biophys J* 83:1557–1566
18. Ng KC, Chu L-K (2013) Effects of surfactants on the purple membrane and bacteriorhodopsin: solubilization or aggregation? *J Phys Chem B* 117:6241–6249. <https://doi.org/10.1021/jp401254j>
19. Xiang Y, Zhang J, Liu Y et al (2011) Design of an effective methanol-blocking membrane with purple membrane for direct methanol fuel cells. *J Membr Sci* 367:325–331. <https://doi.org/10.1016/j.memsci.2010.11.013>
20. Scherrer P, Mathew MK, Sperling W, Stoekenius W (1989) Retinal isomer ratio in dark-adapted purple membrane and bacteriorhodopsin monomers. *Biochemistry (Mosc)* 28:829–834

21. Corcelli A, Lattanzio VMT, Mascolo G et al (2002) Lipid-protein stoichiometries in a crystalline biological membrane: NMR quantitative analysis of the lipid extract of the purple membrane. *J Lipid Res* 43:132–140
22. Lee T-Y, Yeh V, Chuang J et al (2015) Tuning the photocycle kinetics of bacteriorhodopsin in lipid nanodiscs. *Biophys J* 109:1899–1906. <https://doi.org/10.1016/j.bpj.2015.09.012>
23. Yeh V, Hsin Y, Lee T-Y et al (2016) Lipids influence the proton pump activity of photosynthetic protein embedded in nanodiscs. *RSC Adv* 6:88300–88305. <https://doi.org/10.1039/C6RA13650H>

Chapter 4

Effect of Size of Nanodisc



4.1 Introduction

Other than the ability to provide a lipid bilayer environment, nanodisc also has the advantage of producing size homogenous samples. The sample homogeneity is an important factor in the quality of biophysical characterisation, affecting resolution and repeatability.

As well as high size homogeneity, the size of the nanodisc can be varied by adjusting the size of the MSP used to assemble the nanodisc. While changing the lipid to detergent ratio or the types of lipid or detergent can modify the size of the bicelle, the resulting product can be unstable. On the other hand, the nanodisc provides a detergent free system, and the formation of the nanodisc is maintained by the double MSP belt. This indicates that the size of the nanodisc is tuneable by changing the length of the membrane scaffold protein. As mentioned in Chap. 1, MSP derives from human apolipoprotein A [1]. Membrane scaffold protein consists of several amphipathic α helices. Designed by Bayburt et al., MSP1 forms a nanodisc with diameter ~ 10 nm [1]. Longer MSPs were constructed by inserting additional helices, each composed of 22 amino acids, and were shown to successfully form larger nanodisc using size exclusion chromatography and small angle X ray scattering [2]. MSP1D1, which has a small truncation at the N-terminal, is the most commonly used MSP in membrane protein research using nanodisc due to its high stability.

One of the major applications of nanodisc is preparing the membrane protein for characterization using solution state NMR, since the dimension of the nanodisc is small thus providing sufficient resolution. The lack of detergent in the nanodisc system also provides significant benefit. Not only might detergent disrupt the function or the structure of the membrane protein and thus causing instability, detergent molecules also increases viscosity and reduces the resolution of NMR spectra. Many protein systems have been studied with solution state NMR using nanodisc as a membrane mimic. MSP1D1 produces nanodisc with a diameter of

roughly 9.5 nm, with the bilayer area estimated to be 7.5 nm in diameter [3]. The product nanodisc translates to roughly 150–200 kDa. Although MSP1D1 nanodisc has been used to perform 2D heteronuclear NMR experiments on various membrane proteins, the size of the nanodisc still proved difficult for multidimensional NMR experiments. Hagn et al. reported constructs of smaller nanodisc that are suitable for high resolution NMR experiments, by deleting an α helix from MSP1D1 [4]. By deleting the helix 5 from MSP1D1, MSP1D1 Δ H5 (Δ H5) nanodisc has a calculated diameter of 8.4 nm, and has a molecular weight \sim 100 kDa estimated using NMR rotational correlation time [4].

With the smaller complex and reduced molecular weight, the nanodisc was able to solve the structure of membrane protein using solution state NMR. However, with a reduction in size, the area of the phospholipid is reduced significantly, which may or may not cause small alterations to the membrane protein's properties. Furthermore it is unclear if the structural confinement of the nanodisc has any effect on the membrane protein. On the native membrane the area of lipid bilayers are not as restricting as those on a nanodisc, and it is uncertain if the decrease of lipid molecules surrounding the membrane protein would have an impact on the properties of protein.

By using the *E. coli* expressed bacteriorhodopsin from *Haloarcula marismortui* with a mutated site (HmBRID94N) as target membrane protein, we demonstrated the size of nanodisc does not have a significant influence over the function of the protein embedded. First HmBRID94N was optimized and purified using Triton X-100 as a solubilization agent to obtain monomeric bR in detergent micelle. HmBRID94N was purified using a polyhistidine tag attached to the C terminal, followed by size exclusion chromatography. Isotopically labeled (^2D , ^{15}N) HmBRID94N was studied using solution state NMR after being exchanged into 1,2-diheptanoyl-sn-glycero-3-phospho-choline (c7-DHPC), and showed promising potential for further characterization using solution state NMR. The different sizes of nanodisc were achieved by assembling nanodisc with membrane scaffold protein of different lengths, shown in Fig. 4.1. Instead of using the linear-form MSPs, the circularized MSPs with chemically joined C and N termini were employed, in order to achieve higher stability and size control. As the circularized MSP only contained a small modification in the termini of the protein, the overall structure and number of helices of the linear and the circularized form of respective MSP are the same. To demonstrate how the sizes of nanodisc would affect the function of HmBRID94N, cE3D1 and c Δ H5 were used, based on the significant difference of the reported sizes of their respective linear counterpart.

After incorporating HmBRID94N into nanodisc, the nanodisc assembly was purified using Ni-NTA to separate the HmBRID94N embedded and empty nanodisc, as the polyhistidine tag of MSP had been removed using TEV protease reaction. The oligomeric state of HmBRID94N in TX-100 micelle and embedded nanodisc was verified using visible wavelength circular dichroism, and the photocycle kinetics of each sample was characterized using transient absorption spectroscopy.

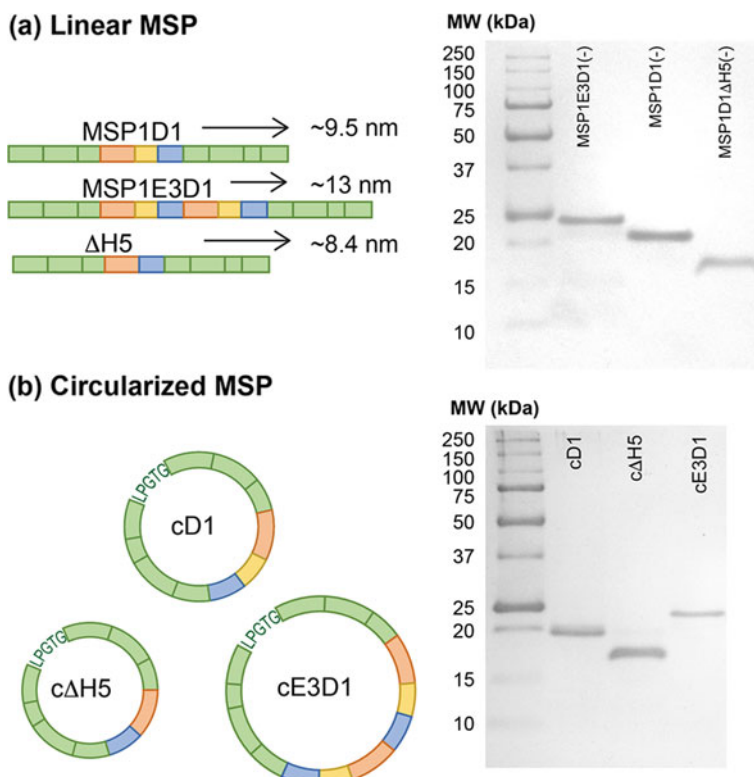


Fig. 4.1 Schematics and SDS PAGE of different sizes of **a** linear MSP and **b** circularized MSP (cMSP), and the reported nanodisc size in diameter for the linear MSP. Each MSP's individual helices are shown as color blocks, with highlights over helix 4, 5 and 6 of MSP1D1. SDS PAGE of each linear MSP had their N terminal histidine tag cleaved off using TEV protease

4.2 Experimental Details

4.2.1 Sample Preparation

4.2.1.1 Preparation of HmbrID94N

HmbrID94N with C terminal polyhistidine tag was expressed using *E. coli* C43 (DE3), generously provided by Professor Chii-Shen Yang of Department of Biochemical Science and Technology, National Taiwan University. The expression conditions of HmbrID94N and purification using DDM as solubilizing agent were described previously in Sect. 2.8. The final purified protein was eluted from the Ni-NTA resin using elution buffer containing DDM, and the excess imidazole was removed using dialysis overnight.

Table 4.1 HmbRID94N purification buffer containing Triton X-100

		pH
Lysis	50 mM Tris-HCl, 1 M NaCl, 0.2 mM PMSF, 14.7 mM β -mercaptoethanol, small amount of DNase and Lysozyme	6
Solubilization	Lysis buffer + 0.5% Triton X-100	6
Binding	50 mM Tris-HCl, 500 mM NaCl, 0.5% Triton X-100	8
Wash buffer 1	Binding buffer + 20 mM imidazole	8
Wash buffer 2	Binding buffer + 30 mM imidazole	8
Elution	Binding buffer + 500 mM imidazole	8
Dialysis	25 mM Tris-HCl, 100 mM NaCl, 0.5 mM EDTA	6
Size exclusion	25 mM Tris-HCl, 100 mM NaCl, 0.5 mM EDTA, 3 mM Triton X-100	6

HmbRID94N purified using Triton X-100 as detergent was modified to avoid denaturing of protein with Triton X-100 micelle, particularly in the presence of illumination (Table 4.1). The NaCl concentrations of the purification buffers were lowered to prevent phase separation with Triton X-100. After lysis and centrifugation, the membrane fraction was solubilized using solubilization buffer containing 0.5% Triton X-100 for 15 h. Employing centrifugation to separate the solubilized fraction and the unwanted insoluble fraction, the solubilized protein was mixed with binding buffer to adjust pH before binding to the Ni-NTA resin. After binding for 1 h, the Ni-NTA resins were washed with wash buffers containing 25 mM Tris-HCl, 500 mM NaCl, 0.5% Triton X-100 and 20 mM or 30 mM imidazole. The protein was eluted from the column using elution buffer containing high concentration imidazole. The imidazole was removed from the sample by dialysis, twice at 1 L to avoid the removal of Triton X-100. After dialysis, the sample was purified further using size exclusion chromatography. The buffer used for purification using size exclusion consisted of 25 mM Tris-HCl, 100 mM NaCl, 0.5 mM EDTA and 3 mM Triton X-100 at pH 6.

4.2.1.2 HmbRID94N Detergent Exchange

HmbRID94N in Triton X-100 was exchanged into C7-DHPC using Ni-NTA. HmbRID94N in Triton X-100 was diluted with buffer containing 50 mM Tris, 100 mM NaCl, 0.5% Triton X-100 at pH 8 to increase the pH of the sample optimum for Ni-NTA binding, then the sample was incubated with Ni-NTA for 80 min. After the buffer containing Triton X-100 was removed, sample bound to Ni-NTA was washed twice with buffer consisted of 50 mM Tris, 500 mM NaCl and 0.1% C7-DHPC at pH 8, before the sample was eluted from the column using the wash buffer with additional 500 mM imidazole at pH 8. The eluted sample was applied onto a size exclusion chromatography column. The buffer for size exclusion chromatography consisted of 50 mM NaPi, 100 mM NaCl and 3 mM C7-DHPC at pH 6.

4.2.1.3 Nanodisc Assembly

E3D1_srt and GB1 Δ H5_srt were expressed and purified as previously described in Sect. 2.6.1, while the sortase catalyzed circularization from E3D1_srt and GB1 Δ H5_srt into cE3D1 and c Δ H5, respectively, were described in Sect. 2.6.2. DMPG (1,2-dimyristoyl-sn-glycero-3-phospho-[1'-rac-glycerol]) was purchased from Avanti Polar Lipids, Inc, and were prepared in a stock solution with lipid and Triton X-100 concentration at 50 mM and 200 mM, respectively. HmBRID94N solubilized in Triton X-100, cMSP and solubilized lipid solution was mixed and incubated for 2 h in 4 °C with gentle agitation before the addition of BioBeads for detergent removal.

After the removal of Biobeads, the nanodisc sample was applied onto a Ni-NTA column for separation of empty and HmBRID94N embedded nanodiscs. The Ni-NTA flow through and an additional wash without imidazole was collected and condensed. The HmBRID94N embedded nanodisc was eluted from Ni-NTA using elution buffer containing 50 mM Tris, 500 mM NaCl and 500 mM imidazole at pH 8. Both fractions were applied onto size exclusion chromatography columns, monitoring both 280 and 552 or 545 nm absorption.

4.2.2 Sample Characterization

Size Exclusion Chromatography. The size exclusion chromatography was performed with either a HiLoad 16/600 Superdex 200 PG column or a Superdex 200 Increase 10/300 GL column (GE Healthcare) depending on the volume of the sample and concentration for optimum separation. Experiments using either column were performed at room temperature. The elution buffer consisted of 25 mM Tris, 100 mM NaCl and 0.5 mM EDTA. The TX-100 containing purification buffer had an additional 3 mM TX-100 and was at pH 6, whereas the nanodisc purification buffer was pH 7.5 and did not contain detergent. Sample elution was monitored at both 280 nm absorption for the protein absorption peak, and at 560 nm absorption for the bR characteristic absorption.

Circular Dichroism Spectroscopy. The circular dichroism (CD) spectra were recorded with a model No. J-815 spectrometer (JASCO), averaged for 1.2 s at 1 nm intervals between 700 and 400 nm at 28 °C. The path length of the cuvette was 1 mm.

Steady State Absorption Spectroscopy. The steady state UV-Vis absorption spectra were recorded with a model No. USB4000-UV-VIS spectrometer (Ocean Optics) at room temperature. The path length of the cuvette used for steady state spectroscopy was 1 cm.

Time-Resolved Absorption Spectroscopy. The transient absorption spectroscopy was performed at 28 °C using a temperature monitor to avoid the transient temperature of DMPG at 23 °C. The concentration of sample was maintained at 20 μ M prior to the laser excitation. An appropriate excitation repetition rate was

optimized to be 0.1 Hz for HmbRID94N in TX-100 micelle, and 0.5 Hz for HmbRID94N embedded in nanodisc. For HmbRID94N in TX-100, temporal profiles of 300 laser excitations were averaged, as were 1000 laser excitations for HmbRID94N embedded nanodisc. The samples of HmbRID94N embedded in nanodisc were exchanged in buffer consisting of 25 mM Tris-HCl, 100 mM NaCl, 0.5 mM EDTA at pH 6.

Solution State NMR. The sample for solution state NMR was exchanged into a buffer containing 50 mM NaPi, 100 mM NaCl and 0.61% *c*7-DHPC (w/v) at pH 6 with 5.72% D₂O (w/w). The ¹H–¹⁵N HSQC experiment was performed on Bruker Avance III 850 MHz NMR spectrometer.

4.3 Results and Discussion

HmbRID94N was purified using DDM or Triton X-100. The purified protein in detergent micelle was characterized using SDS-PAGE for purity checking and circular dichroism for determination of oligomeric state. Monomeric HmbRID94N in Triton X-100 was then taken to perform time-resolved difference spectra for characterization of photocycle.

Monomeric HmbRID94N was incorporated into nanodisc composed of DMPG, using either MSP1D1 or MSP1D1ΔH5 as MSP. The nanodisc assembly was purified using Ni-NTA to separate the empty and the HmbRID94N embedded nanodisc. The sample then underwent size exclusion chromatography, before exchanging into buffer with 25 mM Tris-HCl, 100 mM NaCl, 0.5 mM EDTA at pH 6. The HmbRID94N embedded nanodisc was characterized with circular dichroism and steady state absorption spectroscopy, before the photocycle kinetics were characterized using time-resolve difference spectra.

4.3.1 *HmbRID94N Purification Using Trion X-100*

The purification of HmbRID94N using DDM as a solubilization agent has been previous established, providing sufficient amount and pure HmbRID94N as seen on SDS PAGE [5]. However, due to the mild nature of DDM as a detergent, the resulting purified HmbRID94N appears to be partially trimeric thus complicating further characterizations or incorporation into nanodisc. Since monomeric HsbR, used previously in lipid composition studies in Chap. 3 was solubilized in Triton X-100, HmbRID94N was believed to be compatible with Triton X-100. Composition of purification buffer containing Triton X-100 is shown in Table 4.1.

In the purification buffers of HmbRID94N with DDM, a high amount of NaCl was used to preserve and protect the protein during lysis and solubilization. However, high concentration of NaCl and Triton X-100 causes severe phase separation, which further complicates the purification procedure. Hence the

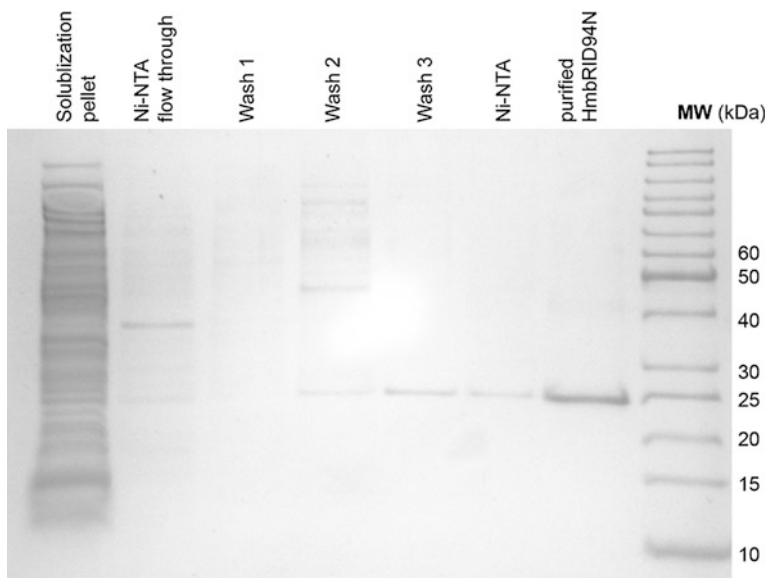


Fig. 4.2 SDS PAGE of HmbRID94N Triton X-100 purification

concentration of NaCl was reduced from 2 to 0.5 M. As a consequence of decreasing the concentration of NaCl and Triton X-100 being a detergent that is slightly stronger compared to DDM, during the purification process the avoidance of illumination was crucial and the duration of the solubilization was reduced to prevent denaturing of protein. To increase the stability of HmbRID94N during the long solubilization process, the pH of solubilization buffer was reduced from pH 8 to pH 6. The solubilization mixture was diluted with binding buffer at pH 8 at 1:1 ratio moments before binding to Ni-NTA to increase affinity. Moreover, the imidazole concentration had to be modified from the purification procedure using DDM, as Triton X-100 appeared to weaken the interaction between the histidine tags and Ni-NTA. Shown in Fig. 4.2 is the SDS PAGE of HmbRID94N purification procedure using Triton X-100.

After the purified protein was eluted from Ni-NTA using elution buffer containing high concentration of imidazole, the sample was moderately condensed before the imidazole was removed through dialysis. After dialysis HmbRID94N was purified further using size exclusion chromatography to remove high molecular weight impurities that Ni-NTA could not successfully remove. Shown in Fig. 4.3, the size exclusion chromatography profile of HmbRID94N purification with elution buffer containing Triton X-100. As indicated by the absorption at 552 nm, the HmbRID94N containing fraction can be separated from high molecular weight impurities.

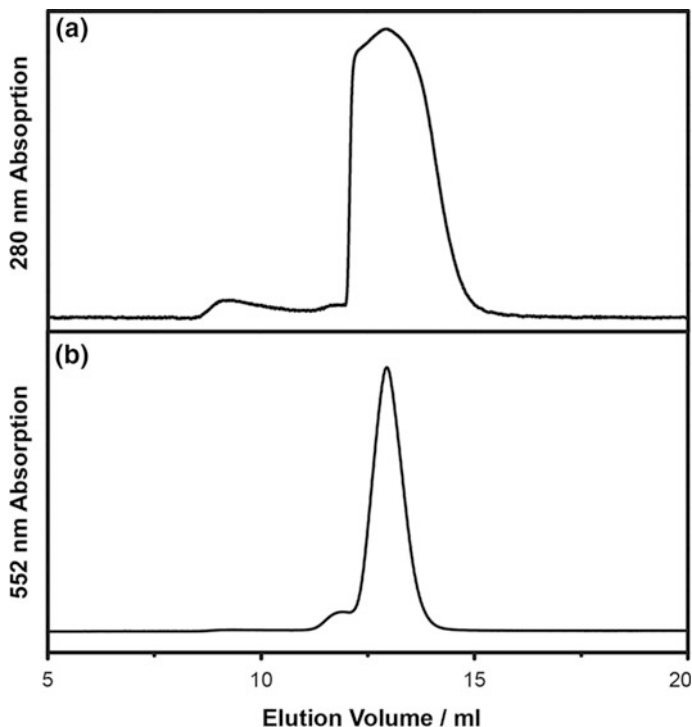


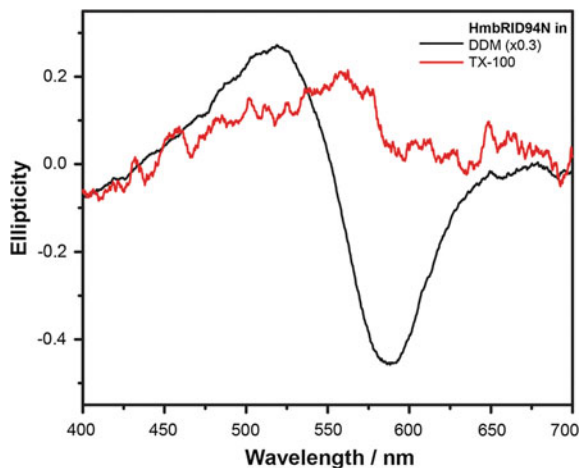
Fig. 4.3 Size exclusion chromatography profiles of HmbRID94N in Triton X-100, monitoring at **a** 280 nm and **b** 552 nm

4.3.2 *HmbRID94N* Characterization in Triton X-100

HmbRID94N purified in detergent micelle was characterized first using visible wavelength circular dichroism. Shown in Fig. 4.4 the circular dichroism spectra of HmbRID94N in DDM and in Triton X-100 micelle. The concentrations of HmbRID94N in DDM and in Triton X-100 are 160 μM and 53 μM , respectively, and spectrum of HmbRID94N in DDM was reduced 70% in order to compare the two spectra. HmbRID94N in DDM displayed clear biphasic feature, illustrating the presence of HmbRID94N trimer in the sample. However, in the results of HmbRID94N purified in Triton X-100 the spectrum indicated a clear monophasic peak, characteristics of monomeric species. The results shown in Fig. 4.4 suggests that HmbRID94N purified using Triton X-100 produced mainly monomeric conformation rather than partially trimeric.

Monomeric HmbRID94N in Triton X-100 was taken to perform transient absorption spectroscopy to reveal its photocycle kinetics. Shown in Fig. 4.5 are the time resolved difference spectra monitoring at different wavelengths for different intermediate states. The amino acid mutation at aspartic acid 94 is a key residue in the retinal pocket during proton translocation, therefore by mutating aspartic acid

Fig. 4.4 Circular dichroism spectra of HmbRID94N purified using DDM as solubilization agent (black) and Triton X-100 as solubilization agent (red), both performed at 20 °C. The concentrations of HmbRID94N in DDM and in Triton X-100 are 160 μM and 53 μM , respectively. The circular dichroism intensity for HmbRID94N solubilized in DDM is reduced to 30% for figure comparison



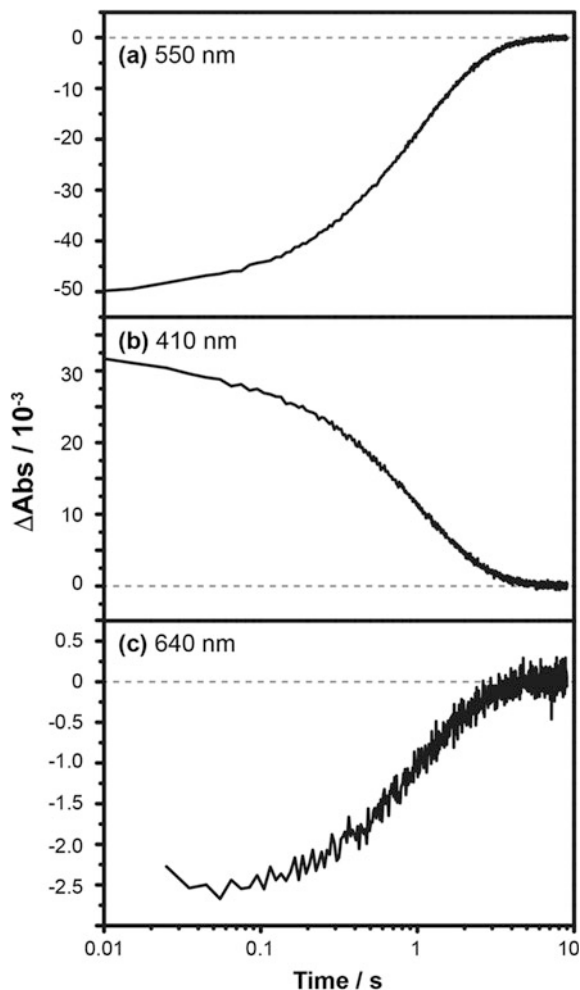
94 into an uncharged amino acid asparagine, the rate of proton pumping was hypothesized to decrease in comparison to the wild type HmbRI [6]. In Fig. 4.5a, the recovery of the parent ground state of HmbRID94N in Triton X-100 in pH 6 was shown to be around 6 s, and the M intermediate lifetime appeared to directly reflect the parent state recovery rate, while O intermediate state behaved differently.

Referring to Tsai et al., wild type HmbRI in DDM at pH 5.8 has a photocycle completed in less than 1 s while observing a minor population of intermediate O state at 640 nm [6]. Due to the proximity of 640–552 nm and the intensity of the parent state depletion, the difference absorption spectrum at 640 nm often includes a minor signal from the parent state depletion which overlaps with the O intermediate state population. In Fig. 4.6, the temporal profiles Fig. 4.5a and c were normalized to elucidate the signals from O intermediate state. However, shown in Fig. 4.6 the normalized time resolved difference spectra monitoring 550 and at 640 nm appear to overlap, indicating either no or only very weak O intermediate. This could suggest the photocycle kinetics of HmbRID94N has been significantly altered with the single amino acid mutation.

4.3.3 HmbRID94N in C7-DHPC

HmbRID94N purified from *E. coli* using Triton X-100 as a solubilization agent is not suitable to be studied using solution state NMR due to poor resolution. Therefore in order to prepare monomeric HmbRID94N for solution NMR, the sample was exchanged into a different detergent, C7-DHPC. Although DDM was demonstrated to show compatibility with HmbRID94N, the membrane protein appeared to contain some trimeric population, shown in Fig. 4.4, which would significantly decrease the spectral resolution of NMR experiment. DHPC has been

Fig. 4.5 Time resolved difference spectra of monomeric HmbRID94N in Triton X-100, monitoring **a** parent state recovery at 550 nm, **b** intermediate M state at 410 nm and **c** intermediate O state at 640 nm



previously used to solubilize membrane protein for structural determination and was reported to improve the NMR spectral quality and resolution [7]. HmbRID94N was exchanged into C7-DHPC from Triton X-100 using Ni-NTA. After the HmbRID94N was eluted from the Ni-NTA into buffer containing C7-DHPC, the sample was purified using size exclusion to separate undesirable oligomeric states, as well as exchanging into NMR appropriate buffer.

Figure 4.7a shows the size exclusion chromatography profile of HmbRID94N exchanged into C7-DHPC. The characteristic HmbRID94N absorption at 552 nm indicated that the sample contained a major smaller species and a minor bigger aggregate, with their sizes estimated at 70 and 156 kDa, respectively. Judging from the molecular weight differences the aggregate is likely to be the minor trimeric HmbRID94N, which can be separated from the monomeric form in detergent. The

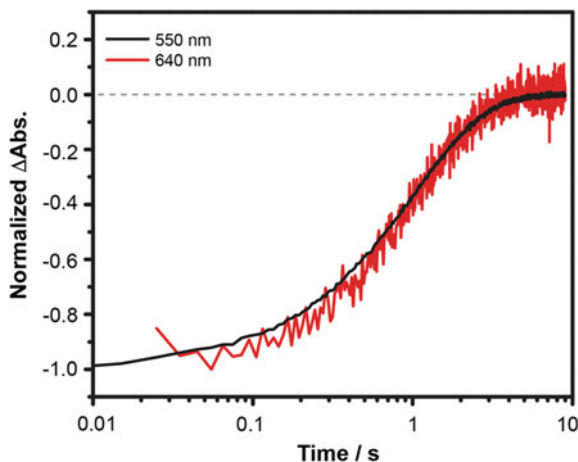


Fig. 4.6 Normalized time-resolved difference spectra of monomeric HmbrID94N in Triton X-100 monitoring the parent state recovery at 550 nm (black) and 640 nm (red)

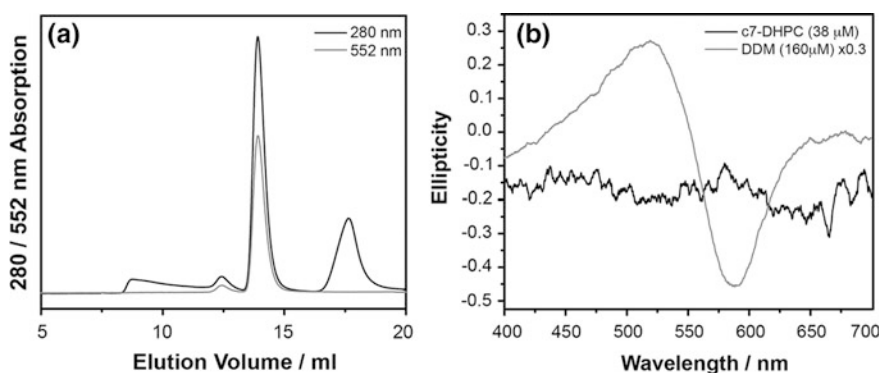


Fig. 4.7 **a** Size exclusion chromatography profiles of HmbrID94N in C7-DHPC, monitoring at 280 nm (black) and 552 nm (gray). **b** Visible wavelength circular dichroism spectra of HmbrID94N in C7-DHPC (black) and HmbrID94N in DDM (gray). The trimeric HmbrID94N in DDM was scaled down to 30% to aid comparison

monomeric HmbrID94N in C7-DHPC detergent micelle was collected, condensed and verified with visible wavelength circular dichroism, shown in Fig. 4.7b. By comparing the spectrum obtained for C7-DHPC to the trimeric HmbrID94N in DDM previously recorded, it can be concluded that, by the lack of biphasic feature, HmbrID94N in C7-DHPC exists in monomeric form. The monomeric, isotopically labeled HmbrID94N in C7-DHPC was then condensed further in preparation of solution state NMR experiment.

Fig. 4.8 ^1H - ^{15}N HSQC NMR spectrum of HmbRID94N in C7-DHPC detergent micelle recorded at 37 °C

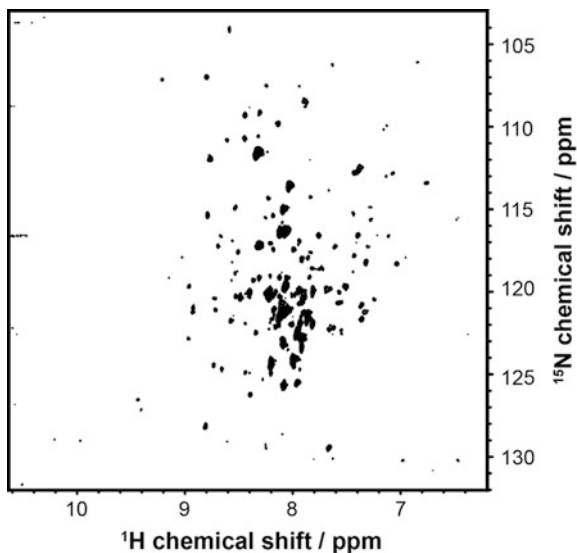


Figure 4.8 shows the ^1H - ^{15}N HSQC spectrum of HmbRID94N embedded in C7-DHPC micelle, recorded at 37 °C. The resolution of spectrum is less than desirable due to possible formation aggregating HmbRID94N during condensing and acquisition period. However, the spectrum was well dispersed, suggesting the protein is folded in the detergent micelle. With an optimized detergent buffer condition, it would be possible to achieve chemical shift assignment. The result showed promise for further characterization of HmbRID94N using solution state NMR to explore structural information.

4.3.4 *HmbRID94N* in Nanodisc

The ability of incorporating monomeric HsbR purified from *H. salinarum* into nanodisc of different lipid compositions was demonstrated in Chap. 3. However, since HsbR was purified directly from the purple membrane of *H. salinarum* it was unclear how much, if any, native lipid from PM was still present in the solubilized monomeric HsbR in detergent. Those lipids might transfer to the nanodisc during nanodisc assembly. It was shown that the lipid composition has a significant effect on the photocycle, so if the native purple membrane lipids were present in the nanodisc surrounding the protein, it would have an influence over the photocycle. In the studies described in Chap. 3, the size of the nanodisc was fixed while the lipid composition was altered. If monomeric bR in detergent micelle carried any native lipid molecules, the amount of native lipid molecules incorporated into the nanodisc would not vary significantly. However, in the study of the effect of different nanodisc sizes, it would be difficult to determine how much of the native lipid was incorporated into the

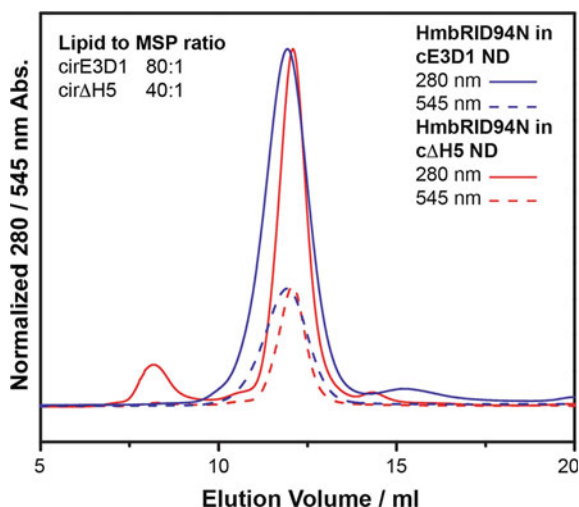
nanodisc of different sizes, and if that amount was the same with different sized nanodisc.

HmbRID94N was expressed using *E. coli* and purified using polyhistidine tags, eliminating the possibility of residual native lipids present in the sample. Similar to HsbR, HmbRID94N is an integral protein with seven transmembrane α helices. HmbRID94N was hypothesized to enter the nanodisc lipid bilayer in a similar fashion as HsbR. Demonstrated in the size exclusion chromatography profile Fig. 4.9, HmbRID94N was successfully incorporated into lipid nanodisc of two difference sizes, with 545 nm being the characteristic HmbRID94N absorption in nanodisc. Both samples were previously treated using a Ni-NTA purification column to separate the empty and the HmbRID94N embedded nanodisc, as only HmbRID94N contained the polyhistidine tags to bind to Ni-NTA.

The bigger nanodisc consisted of cE3D1 and the smaller nanodisc consisted of cir Δ H5, both composed of DMPG lipid bilayer. The difference sizes could be seen on the size exclusion chromatography profiles, as well as their optimized lipid to MSP ratio. Although the difference in elution volumes between the two different sizes of nanodisc seemed small, the elution volume of size exclusion is often only suitable for estimation. While size exclusion can separate sample based on the size of the particle, nanodisc is not an ideal spherical object. As different sizes of nanodisc have different radius on the lipid surface, the ratio between the width of the disc and the height of the hydrophobic face changes. Therefore it is only appropriate to use the size exclusion chromatography profile in Fig. 4.9 to conclude that nanodisc consisted of cE3D1 is indeed bigger than the nanodisc made from cir Δ H5.

The nanodisc samples were collected, condensed and characterized using spectroscopic methods. Figure 4.10 shows the steady state absorption spectra of HmbRID94N embedded in two different sizes of nanodisc, in comparison to HmbRID94N in detergent micelle. All the samples were light adapted for more than 30 min. On the steady state spectrum, HmbRID94N embedded in nanodisc displayed a significant blue shift compared to HmbRID94N in detergent micelle. Once

Fig. 4.9 Size exclusion chromatography profiles of HmbRID94N incorporated in nanodisc composed of DMPG, with ether cE3D1 (blue) or cir Δ H5 (red) as membrane scaffold protein. Elution was monitored using 280 nm (solid line) and 545 nm (dashed line) absorption



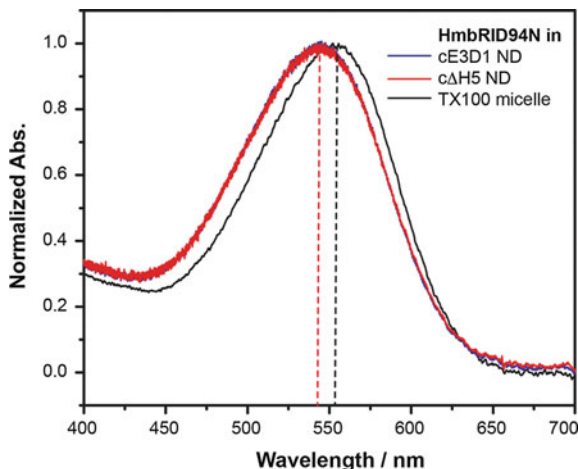


Fig. 4.10 Steady state absorption spectra of monomeric HmbRID94N in Triton X-100 detergent micelle (black), embedded in nanodisc composed of cE3D1 and DMPG (blue) or embedded in nanodisc composed of cΔH5 and DMPG (red). The vertical dashed lines indicate the absorption maxima of HmbRID94N in detergent micelle at 552 nm (black) and HmbRID94N in nanodisc at 545 nm (red)

incorporated into nanodisc, the absorption maximum HmbRID94N shifts from 552 nm to 545 nm. This blue shift is independent of the size of the nanodisc, which can indicate it is caused by the changes in surrounding lipid environment.

Figure 4.11 shows the visible wavelength circular dichroism of HmbRID94N embedded in DMPG nanodisc of different sizes. The experiments were performed

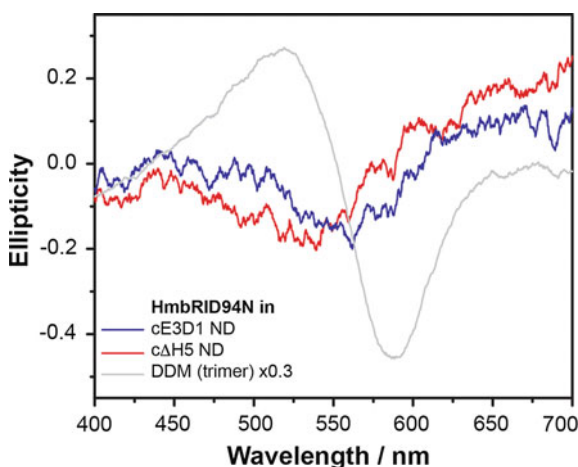


Fig. 4.11 Visible range circular dichroism spectra of HmbRID94N embedded in nanodisc consisted of cE3D1 (blue) cΔH5 (red) recorded at 26 °C, in comparison to trimeric HmbRID94N in DDM (black). The ellipticity of trimeric HmbRID94N in DDM was reduced to 30% to showcase the biphasic feature in the similar scale

at 26 °C to avoid the phase transition temperature of DMPG at 23 °C. With the clear absence of biphasic features within the visible wavelength range, such as the spectrum displayed by HmbrID95N in DDM micelle, it can be concluded that HmbrID94N embedded in nanodisc is no trimeric.

The photocycle kinetics of HmbrID94N embedded in nanodisc were characterized using transient absorption spectroscopy. The repetition rate optimization is shown in Fig. 4.12. During the repetition rate optimization experiment, both samples showed similar recovery rates. Figure 4.13 showed the time resolved difference spectra of HmbrID94N embedded in nanodisc of different sizes, recorded using laser pulse repetition rate of 0.2 Hz. The time resolved difference experiment was recorded observing the ground state recovery at 545 nm and the M intermediate state at 410 nm. The weighted spectra using absorption at 532 nm showed HmbrID94N in different size nanodisc have similar intensities, thus a similar photo-active population. The time resolved difference spectra observing the ground state recovery of HmbrID94N showed that not only does HmbrID94N embedded in different sizes of nanodisc have similar spectroscopic intensities, but also similar photocycle life time and recovery rate. On the other hand, while observing the population of M intermediate state, HmbrID94N embedded in nanodisc of different sizes displayed minor differences in the decay of M intermediate. HmbrID94N embedded in the smaller nanodisc consisting of c Δ H5 showed a slightly longer M intermediate state lifetime in comparison to the bigger nanodisc consisting of cE3D1, despite such difference not being observed in the ground state recovery profiles. However, this difference in the lifetime of intermediate M observed is not significant in comparison to the difference of bR incorporated in nanodisc with different lipid composition, discussed in Chap. 3.

The intensities of the time resolved difference spectra of HmbrID94N embedded in nanodisc is significantly lower in comparison to the time resolved difference spectrum recorded for HmbrID94N in Triton X-100 micelle, shown in Fig. 4.14.

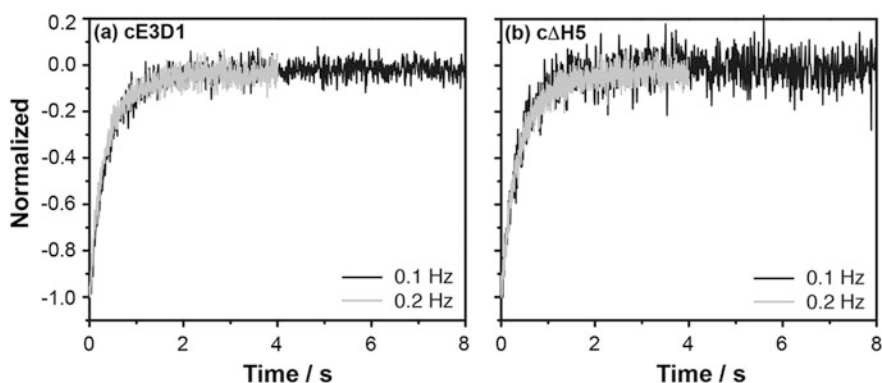


Fig. 4.12 Normalized time resolved difference spectra of HmbrID94N embedded in nanodisc consisted of **a** cE3D1 and **b** c Δ H5, for repetition optimization of the recovery of HmbrID94N at 545 nm upon 532 nm excitation pulses. The repetition rates of the laser pulses are 0.1 Hz (black) and 0.2 Hz (gray)

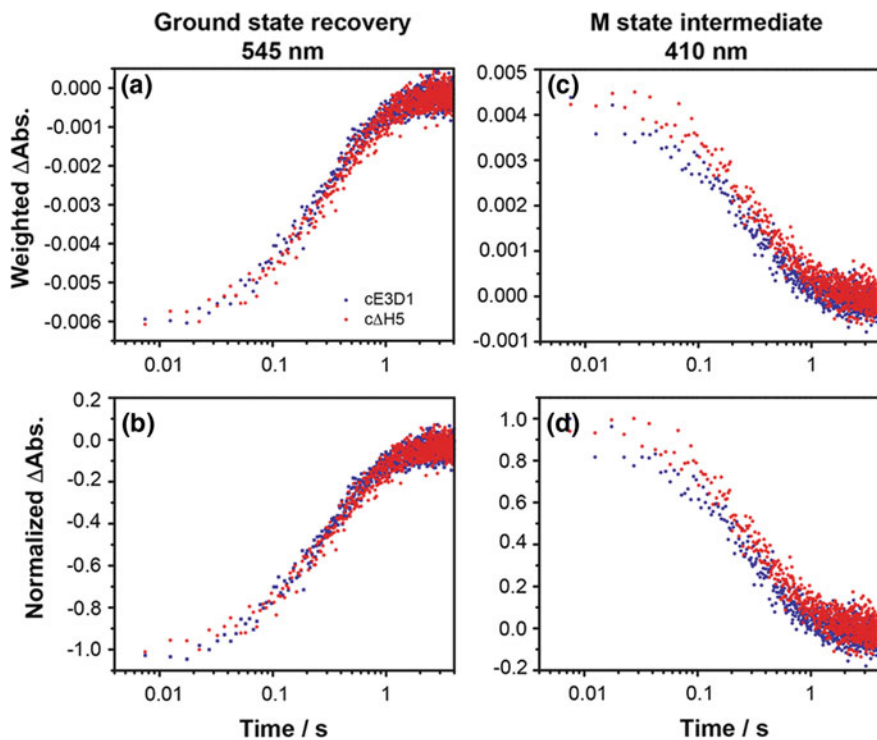
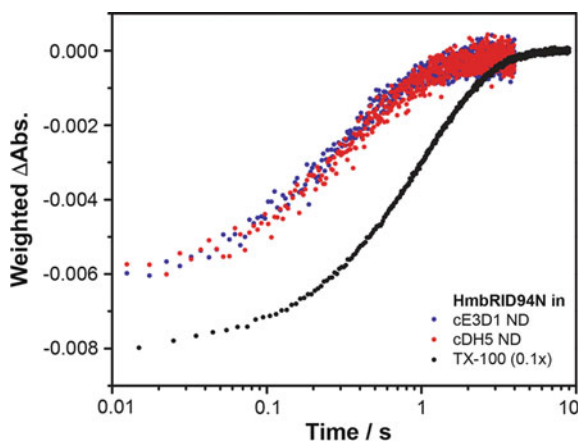


Fig. 4.13 **a, c** Weighted using absorption at 532 nm and **b, d** normalized time resolved difference spectra of HmbRID94N embedded in nanodisc of cE3D1 (blue) or cΔH5 (red), monitoring **a, b** parent state recovery at 545 nm and **b** M intermediate at 410 nm

Fig. 4.14 Weighted time resolved difference spectra of HmbRID94N in nanodisc consisting of cE3D1 (blue) and cΔH5 (red), and HmbRID94N in Triton X-100 micelle (black). The spectra recorded for HmbRID94N in detergent micelle has been scaled down to 10% of its original intensity for ease of comparison



HmbRID94N in Triton X-100 micelle was recorded at pH 6, when HmbRID94N in nanodisc was recorded at pH 5.8. While pH is a major factor in the kinetics of photocycle of bacteriorhodopsin [6], the similarities in the range of pH should allow an estimated comparison to be made between the different sets of samples. The decrease in intensities in the time resolved difference spectra can be explained by the shift observed in the steady state spectra shown in Fig. 4.10, where HmbRID94N embedded in nanodisc has a blue shift in the absorption contours. The blue shift could be caused by a change in retinal conformation, specifically a decrease in the photocycle active *all trans* retinal population. With a decrease in the photocycle active retinal, a decrease in number of photocycles initiated is expected. Since the blue shift in steady state absorption contour and the decrease in intensities of transient absorption spectra are both observed for HmbRID94N embedded in nanodisc of different sizes, and in a similar scale, it is therefore reasonable to conclude that the phenomenon is related to the structure of the surrounding lipid environment. A consequence of a decrease in the intensities of time-resolved difference spectra is the study of other intermediate states, for example intermediate O at 640 nm, becomes increasingly difficult as the intensities of O intermediate state is expected to be an order of magnitude lower than the intensities of M intermediate state.

As well as a decrease in photocycle intensities, a significant increase in the photocycle recovery was observed for HmbRID94N embedded in nanodisc at pH 5.8, in comparison to HmbRID94N in Triton X-100 micelle at pH 6. While an increase of photocycle lifetime can be expected at an elevated pH, the length of photocycle lifetime of HmbRID94N in Triton X-100 is still significant longer.

The long photocycle lifetime indicates a slower motion of the protein during the proton pumping process. This could suggest the confinement of the surrounding lipid bilayer has a smaller effect on the function of HmbRID94N, as the dynamic of the membrane protein is not drastic during the photocycle therefore the difference between the smaller and the bigger membrane bilayer might be much smaller, if significant. The longer photocycle of HmbRID94N in comparison to wild type HmbRI or HsbR arose from the mutation at a key amino acid involved in the proton translocation process. The preliminary results from the study of size of nanodisc using monomeric HsbR in DMPC nanodisc consisted of cE3D1 or cirΔH5 and DMPC, are shown in Appendix I, and showed a greater difference in photocycle recovery rate. The monomeric HsbR was previously treated with CHAPSO to remove native lipids and was purified using size exclusion before the incorporation into nanodisc. HsbR embedded in smaller nanodisc consisting of cirΔH5 was found to have a shorter recovery rate in comparison to HsbR embedded in the bigger nanodisc, suggesting that the size of nanodisc can have an effect on the function of membrane protein incorporated. However, the effect of size of nanodisc appeared to be less significant in comparison the effect due to the different lipid composition.

4.4 Conclusion

Nanodisc has provided significant benefits in the study of membrane protein, particularly in structural or functional studies using solution state NMR. Due to the properties of solution state NMR, the resolution of the NMR spectrum is strongly correlated to the size of the subject of interest. Since the sizes of the nanodisc are determined by the membrane scaffold proteins that wrap around the lipid bilayer core, smaller nanodisc have been achieved by reducing the size of the membrane scaffold protein. This strategy has been demonstrated to successfully enhance resolution of NMR spectrum. However, the reduction complex size implies a decrease in the lipid bilayer area.

However, demonstrated using *E. coli* expressed bacteriorhodopsin HmbRID94N, the function of HmbRID94N does not experience significant change when embedded in different sizes of nanodisc.

HmbRID9N was first purified in conditions containing Triton X-100 to obtain monomeric HmbRID94N, and the oligomeric state was verified using visible wavelength circular dichroism. Isotopically labeled HmbRID94N was exchanged from Triton X-100 micelle into C7-DHPC micelle, which is more suitable for solution state NMR study. While the spectral resolution was not desirable, the method showed a promising potential for chemical shift assignment as the spectral quality can be improved with an optimized buffer and experimental condition.

The HmbRID94N embedded nanodisc of different sizes, one composed of cE3D1 and smaller nanodisc composed of cΔH5 were produced. The assembly mixture was purified with Ni-NTA to separate the empty and the HmbRID94N embedded nanodisc, and the nanodisc assembled using different MSP showed a difference in sizes on size exclusion chromatography. The oligomeric state of HmbRID94N embedded nanodisc was characterized using visible wavelength circular dichroism where the spectra displayed a clear lack of biphasic feature, suggesting HmbRID94N incorporates into nanodisc as monomers. The photocycle kinetics of HmbRID94N embedded in nanodisc was studied using transient absorption spectroscopy. The time resolved difference spectra showed that the ground state recovery of HmbRID94N embedded in different sizes of nanodisc behave similarly. On the other hand, the M intermediate state has a slightly slower decay in the smaller nanodisc consisting of cΔH5, in comparison to the nanodisc consisting of cE3D1. However, the difference observed in the M intermediate lifetime is not significant, particularly when compared to the differences observed in the case of different lipid composition. By comparing the weighted spectra, the quantum yield of HmbRID94N in different environments can be compared, as well as the photocycle rate. HmbRID94N embedded in nanodisc has a lower quantum yield compared to HmbRID94N in TX-100 micelle. The phenomenon can be explained by the blue shift observed in the maximum absorption using steady state absorption spectroscopy. This suggests that the membrane bilayer environment affected the photocycle kinetics of HmbRID94N and the status of retinal that is involved in the proton translocation process.

While there was no significant difference observed in the function of HmbRID94N observed in different sizes of nanodisc, the lack of difference may be due to the long photocycle duration of HmbRID94N, as it contained a mutation on the key amino acid involved in the proton translocation process. The long photocycle lifetime suggests a slower motion exhibited by HmbRID94N during the proton translocation process, suggesting that the confinement from the surrounding lipid bilayer would have a smaller effect on the dynamics of HmbRID94N. The effect of size using HsbR with native lipids removed, embedded into nanodisc showed a greater difference between the difference sizes in the preliminary results. This suggests that the size of the nanodisc may still have an effect on the function of membrane protein. However, the effect of the sizes of nanodisc on membrane protein appears to be less significant than the effect of changing lipid composition.

Acknowledgements The plasmid of wild type HmbRI and HmbRII, as well as *E. coli* C43 (DE3) used for expressing HmbRID94N was generously provided by Professor Chii-Shen Yang, from the Department of Biochemical Science and Technology, National Taiwan University.

References

1. Bayburt TH, Grinkova YV, Sligar SG (2002) Self-assembly of discoidal phospholipid bilayer nanoparticles with membrane scaffold proteins. *Nano Lett* 2:853–856. <https://doi.org/10.1021/nl025623k>
2. Denisov IG, Grinkova YV, Lazarides AA, Sligar SG (2004) Directed self-assembly of monodisperse phospholipid bilayer nanodiscs with controlled size. *J Am Chem Soc* 126:3477–3487. <https://doi.org/10.1021/ja0393574>
3. Bayburt TH, Sligar SG (2010) Membrane protein assembly into nanodiscs. *FEBS Lett* 584:1721–1727. <https://doi.org/10.1016/j.febslet.2009.10.024>
4. Hagn F, Eitzkorn M, Raschle T, Wagner G (2013) Optimized phospholipid bilayer nanodiscs facilitate high-resolution structure determination of membrane proteins. *J Am Chem Soc* 135:1919–1925. <https://doi.org/10.1021/ja310901f>
5. Hsu M-F, Yu T-F, Chou C-C et al (2013) Using Haloarcula marismortui bacteriorhodopsin as a fusion tag for enhancing and visible expression of integral membrane proteins in Escherichia coli. *PLoS ONE* 8:e56363. <https://doi.org/10.1371/journal.pone.0056363>
6. Tsai F-K, Fu H-Y, Yang C-S, Chu L-K (2014) Photochemistry of a dual-bacteriorhodopsin system in *Haloarcula marismortui*: HmbRI and HmbRII. *J Phys Chem B* 118:7290–7301. <https://doi.org/10.1021/jp503629v>
7. Gautier A, Mott HR, Bostock MJ et al (2010) Structure determination of the seven-helix transmembrane receptor sensory rhodopsin II by solution NMR spectroscopy. *Nat Struct Mol Biol* 17:768–774. <https://doi.org/10.1038/nsmb.1807>

Chapter 5

Native Membrane Nanodisc



5.1 Introduction

Despite nanodisc's ability to provide native-like lipid bilayer to facilitate membrane protein, how native the environment that nanodisc produces is still uncertain. Discussed in Chaps. 3 and 4, both the lipid composition and the size of the nanodisc can have a significant effect on the function of the proton pumping membrane protein bacteriorhodopsin. In Chap. 3 it was shown that the photocycle kinetics of bR embedded in nanodisc is significantly altered by the change in lipid composition. As the negative lipid PG content increases, the faster the photocycle duration and it undergoes the traditional photocycle pathway, which shows a greater similarity to the behavior of bR in native environment. This suggests that compared to neutral lipid PC environment, the negatively charged lipid bilayer is closer to the native environment of bR. Surveying the native lipids found on PM, the negative lipids including PGP-Me, PG and PGS are about 40% of the lipid composition. This observation shows agreement to the experimental data of bR embedding in nanodisc composed of synthetic lipids. However, it is clear that the charge of the hydrophilic lipid head is not the only influence on the photocycle kinetics of bR, and that despite the charge similarities, monomeric bR embedded in nanodisc of synthetic lipid is still far from the native environment.

In traditional nanodisc assembly, both the synthetic lipid and the target protein are solubilized using detergent. With an emphasis on the desire to study membrane protein in its native environment, it is clear that the lipid composition of the lipid bilayer plays an important role. The ideal conditions include membrane protein preserved in the native conformation surrounded by native lipid in a manner that allows biophysical characterization. This idea served as an inspiration to extract membrane protein, along with the surrounding native lipids, directly from the native membrane and incorporate it into nanodisc for structural and functional characterization (Fig. 5.1).

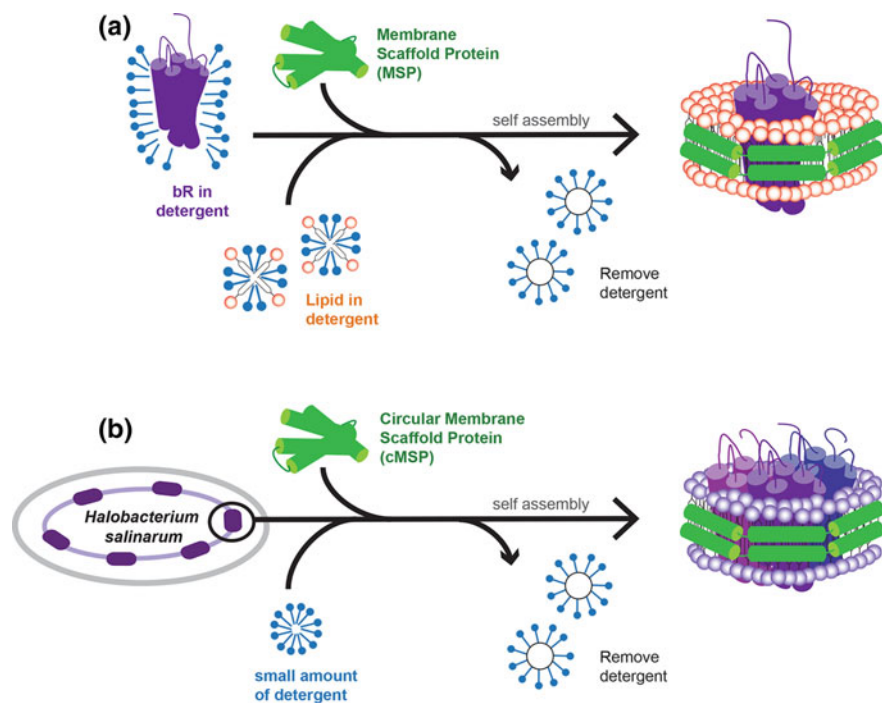


Fig. 5.1 Schematics of **a** traditional nanodisc assembly, where the target membrane protein and additional lipid molecules are solubilized in detergent prior to the assembly, and **b** one-step extraction of membrane protein from native membrane, directly incorporated into native membrane nanodisc. Reproduced with permission from Ref. [24], from Nature Publishing Group

bR is found on the purple membrane of *Halobacterium salinarum*. To demonstrate the concept of one step extraction and incorporation of membrane protein without addition of extra lipid molecules, bR was an ideal candidate due to it being the only protein found on PM, as well as its abundance on the membrane. Bacteriorhodopsin adopts a trimeric conformation on the PM, forming a hexagonal unit. While in Chap. 3 bR was incorporated into nanodisc with synthetic lipids as exclusively monomers, previous studies have shown that bR has the ability to form trimers or monomers, when reconstituted into lipid vesicle or DMPC nanodisc with different temperatures [1, 2] or with different bR to lipid ratio [3–5]. It was reported that incorporation of trimeric bR can be monitored by adjusting the concentration of NaCl [6, 7] and the addition of PM polar lipids [8, 9]. Since the purpose of this work is to extract and incorporate bR into nanodisc directly from the purple membrane, no extra lipid molecules were added into the reaction mixture and only the NaCl concentration was adjusted.

Using a modified MSP where the N and the C termini were chemically linked together [10, 11], we demonstrated that trimeric bacteriorhodopsin with native lipids can be extracted and incorporated into nanodisc in one reaction assembly,

directly from the native purple membrane under optimized conditions. The final product was verified using size exclusion chromatography, showing a narrow symmetrical peak of the size homogenous nanodisc. The nanodisc was further characterized using Zernike phase TEM image, to show the circular disk-like feature of native purple membrane nanodisc (PMND). The oligomeric state of bacteriorhodopsin on PMND was established using circular dichroism, while the lipid composition was characterized using ^{31}P NMR. Finally, single wavelength transient absorption spectroscopy was performed to verify the preservation of the functions of bR.

5.2 Experimental Details

5.2.1 Sample Preparation

5.2.1.1 Preparation of PM

Purple membrane was grown and extracted from *H. salinarum* as described in Sect. 2.7. After purification using sucrose gradient, the sample was dissolved with 4 M NaCl in preparation for high salt concentration native purple membrane assembly.

5.2.1.2 PMND Assembly

PMND assembly differed from conventional nanodisc assembly in two ways. First, the target proteins were still in its native purple membrane instead of being solubilized in detergent micelle. Secondly PMND did not require additional synthetic lipid and therefore the detergent was added separately. Table 5.1 lists the components for PMND assembly, where the ratio between PM to cE3D1 and detergent concentration was later optimized. The assembly buffer contained 25 mM Tris-HCl, NaCl ranging between 100 mM and 5 M depending on the optimized conditions, and 0.5 mM EDTA at pH 7.5.

Table 5.1 PMND assembly and individual components

	Concentration in assembly
DTT	1 mM
Protease inhibitor	1x
Phosphatase inhibitor	1x
cE3D1	20–33 μM
Triton X-100	5–20 mM
Assembly buffer	Topping up assembly
PM	25 μM

Each component was added into the assembly mixture, with PM being the last to avoid high local detergent concentration thus increasing the preservation of the native conformation. After assembly the sample was placed in 4 °C with gentle agitation for a period of time, before BioBeads were added to remove the detergent. After the addition of BioBeads PMND followed the conventional nanodisc assembly procedure previously described in Sect. 2.6 and was purified using size exclusion chromatography.

5.2.2 Sample Characterization

Size Exclusion Chromatography. The PMND sample was purified using size exclusion chromatography, performed with either a HiLoad 16/600 Superdex 200 PG column or a Superdex 200 Increase 10/300 GL column (GE Healthcare) depending on the volume of the sample and concentration for optimum separation. Experiments using either column were performed at room temperature. The elution buffer consisted of 25 mM Tris, 100 mM NaCl and 0.5 mM EDTA at pH 7.5. Sample elution was monitored at both 280 nm absorption for the protein absorption peak, and at 560 nm absorption for the bR characteristic absorption.

Matrix Assisted Laser Desorption Ionization Time of Flight (MALDI-TOF) Mass Spectroscopy. Nanodisc sample was collected and combined after purification using size exclusion chromatography. The salt buffer in the sample was removed by exchanging the sample into distilled water using Centrifugal Concentrator (Vivaspin), before addition of organic solvent mixture of acetone and methanol at a ratio of 7–1, respectively. The sample mixture containing organic solvent was rested on ice for 1.5 h. Protein precipitate was obtained after fast centrifuge, and was dissolved using trifluoroacetic acid (TFA). The dissolved sample was then mixed with DHB matrix mixture before the mass spectroscopy experiment.

Steady state Absorption Spectroscopy. PMND sample was light adapted for more than 30 min prior to the steady state absorption spectroscopy. The steady state UV-Vis absorption spectra were recorded with a model No. USB4000-UV-VIS spectrometer (Ocean Optics) at room temperature. The path length of the cuvette was 1 cm.

Circular Dichroism Spectroscopy. The circular dichroism (CD) spectra were recorded with a model No. J-815 spectrometer (JASCO), averaged for 1.2 s at 1 nm intervals between 700 and 400 nm at 20 °C. The path length of the cuvette was 1 mm.

Zernik Phase Transmission Electron Microscopy. The samples on grids were air dried without staining. Phase TEM images were taken in in-focus condition at 200 kV using an JEM2100 TEM (JEOL) equipped with a LaB6 filament equipped with an Zernike phase plate with a ~700 nm central hole, and a direct detector DE-12 (Direct Electron). The images of unstained sample shown here were recorded at nominal microscope magnifications of $\times 100,000$ and $\times 200,000$.

Lipid Extraction. The lipid of PM and PMND was extracted using organic solvent. 200 μl of protein in aqueous solution was mixed with chloroform and methanol at 0.8:2:1. The sample was vigorously shaken and centrifuged to achieve clear phase separation, and afterwards the upper water phase was discarded. 250 μl of chloroform and water each were added to the lower organic solvent phase to obtain a two-phase system. After another centrifugation to achieve phase separation, the chloroform phase was dried using N_2 gas.

Solution State NMR Spectroscopy. The ^{31}P NMR sample was prepared using methanol reagent containing D_2O and dissolved Cs-EDTA. The cesium salt EDTA was used due to poor solubility of sodium salt EDTA in organic solvents. Cesium salt of EDTA was prepared by titrating EDTA free acid in distilled water with solid CsOH to pH 6, when the EDTA dissolved. The solution was then dried using lyophilization then dissolved D_2O to a concentration of 0.2 M. The methanol reagent was prepared by adding D_2O -Cs-EDTA to methanol with the ratio of 1 to 4, respectively. For the ^{31}P NMR sample, dried extract lipids were dissolved in 400 μl of deuterated chloroform and mixed with 200 μl of methanol reagent containing Cs-EDTA. The sample was placed in the NMR tube where the two phases could be observed: a major chloroform phase and a smaller water phase. The ^{31}P spectra were recorded using a Bruker Avance III 500 MHz NMR spectrometer equipped with a 5 mm CryoProbe Prodigy probehead.

Lipid Chromatography Mass Spectrometry. LC-ESI was performed with LTQ Orbitrap XL ETD mass spectrometer equipped with Waters Acquity UPLC, using a ZIC-HILIC column. The gradient employed contained 98% buffer B at 2 min to 60% buffer B at 45 min, with a flow rate of 50 $\mu\text{l}/\text{min}$. Buffer A consisted of 0.1% formic acid in water, whereas buffer B consisted of 0.1% formic acid in acetonitrile. The mass spectrometry experiment detected mass-to-charge range of 320–2000, with resolution 30,000 at m/z 400. The electrospray voltage was maintained at 4 kV, and the capillary temperature was set at 275 $^\circ\text{C}$.

Transient Absorption Spectroscopy. The concentration of PMND was monitored at 10 μM . The buffer of the sample was the same as the size exclusion chromatography buffer described previously, with 25 mM Tris, 100 mM NaCl and 0.5 mM EDTA at pH 7.5.

5.3 Results and Discussion

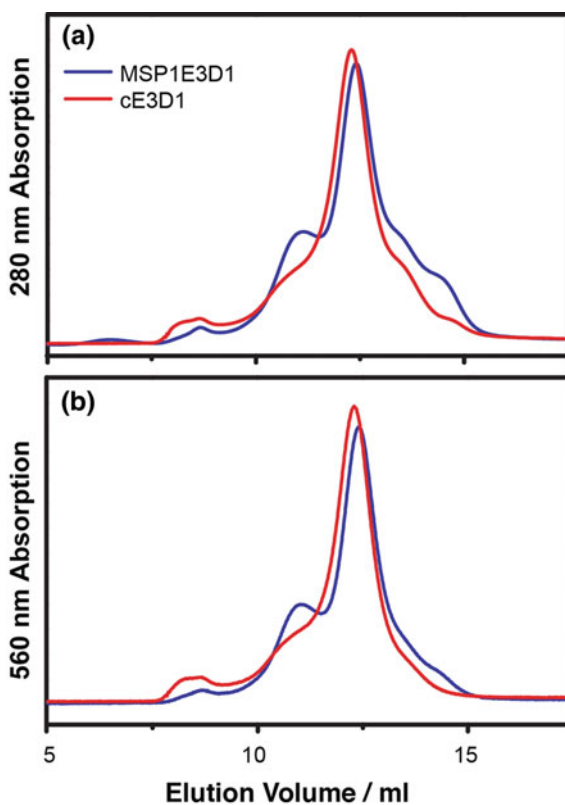
5.3.1 PMND Assembly and Optimization

The procedure of extraction and incorporation of bR from the native purple membrane directly into nanodisc required several steps of optimization, since it is a one-step direct assembly and also due to the homogenous nature of PM. The decision to use the largest available membrane scaffold protein, MSP1E3D1 and its modified version, cE3D1 for the assembly of the native purple membrane nanodisc

was based on the reported size of the trimeric bR determined using X-ray crystallography to be 60.8 Å [12]. The reported sizes of nanodiscs with ΔH5, MSP1D1 and MSP1E3D1 are 8.5 nm [13], 9 nm [14] and 13 nm [15] in diameter, respectively. The diameter of the lipid bilayer area was estimated to be at 7.5 and 10.6 nm for nanodisc with MSP1D1 and MSP1E3D1, respectively [15]. To incorporate trimeric bR in MSP1D1 nanodisc risked protein-protein interaction between MSP1D1 and bR, as well as eliminating space for the extract native lipids. Therefore, the bigger nanodisc of MSP1E3D1 and its modified version cE3D1 were employed for this study.

Figure 5.2 compares PMND assembled with the same conditions such as final salt concentration, but using different forms of MSP and their optimized PM to MSP ratios. Both the linear MSP1E3D1 and circularized MSP1E3D1 (cE3D1) can produce a nanodisc peak that contains bR, as both samples had strong 560 nm absorption. However, under the same conditions the peak produced by cE3D1 is more symmetrical, whereas the peaks of PMND assembled using linear MSP1E3D1 are asymmetric with large amount of aggregates. It is therefore reasonable to conclude that cE3D1 can achieve a higher homogeneity of native purple membrane nanodisc compared to the conventional linear MSP1E3D1.

Fig. 5.2 Size exclusion chromatography profiles for comparison of PMND assembled using convention linear MSP1E3D1 (blue) and circularized cE3D1 (red), monitored at **a** 280 nm and **b** 560 nm absorption. Samples were assembled under the same conditions other than the type of MSP and the respective concentration, with 10 mM Triton X-100, 3.45 M NaCl and incubated for 10 min before detergent is removed. The concentration of MSP1E3D1 and cE3D1 are 29.2 and 25.0 μM, respectively. Reproduced with permission from Ref. [24], from Nature Publishing Group



The type of MSP is not the only factor determining the success of PMND assembly. Demonstrated in Figs. 5.3, 5.4, 5.5 and 5.6 are optimizations of different components in the PMND assembly, including the ratios of PM to cE3D1, incubation duration before detergent was removed, the detergent concentration and the final NaCl concentration in the assembly, respectively.

The ratio between PM and cE3D1 is crucial. In conventional nanodisc assembly the ratio of lipid to MSP is important in the homogeneity of the nanodisc sample, demonstrated in Chap. 2. Since the extraction and the incorporation of bBR from PM into the native purple membrane nanodisc is one single step, the ratio between PM and MSP represents the both the ratios of lipid to MSP and also bBR to MSP. Shown in Fig. 5.3, the ratio between PM and cE3D1 can affect the homogeneity of PMND. When the ratio was not optimized and the amount of PM was too high, the assembly resulted in high molecular weight aggregates. However, when there was too much cE3D1, the excess MSP would form a smaller aggregate close to the size of PMND, becoming difficult to separate and purify from the desire PMND product. It is also important to note that the ratio can vary between different batches of PM and cE3D1, mostly due to the difficulties to accurately determine the concentration of PM.

Fig. 5.3 Size exclusion chromatography profiles for comparison of PMND assembled with different ratios of 3–2 (green), 3–3 (red) and 3–4 (blue), PM to cE3D1, respectively, monitoring **a** 280 nm and **b** 560 nm absorption. Samples were assembled under the same conditions other than the concentration of cE3D1, with 10 mM Triton X-100, 3.63 M NaCl and incubated for 10 min before detergent is removed. Reproduced with permission from Ref. [24], from Nature Publishing Group

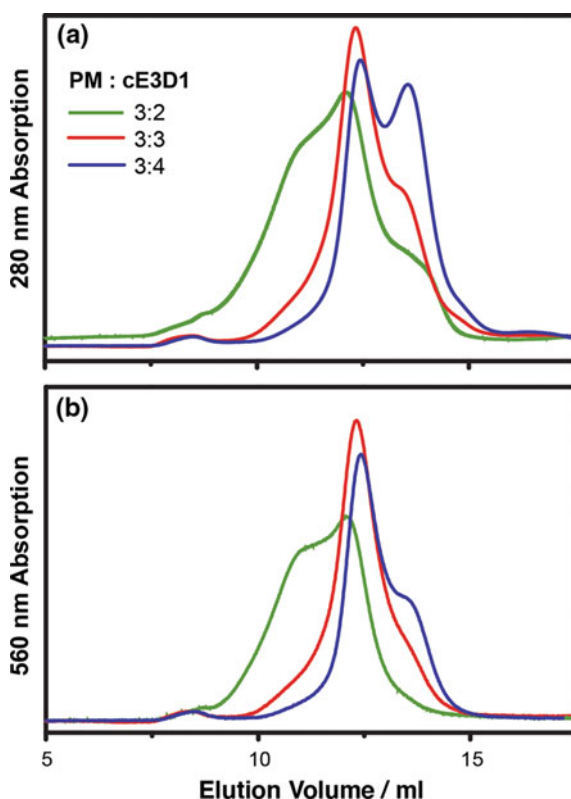
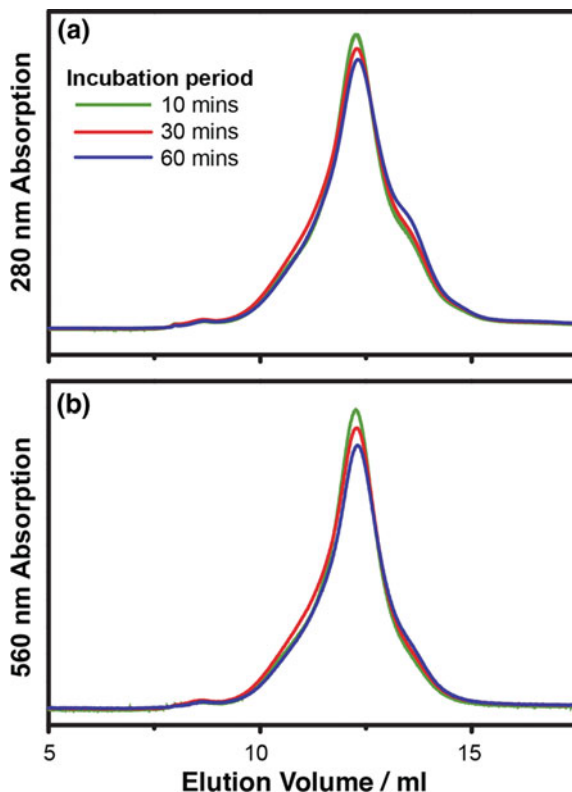


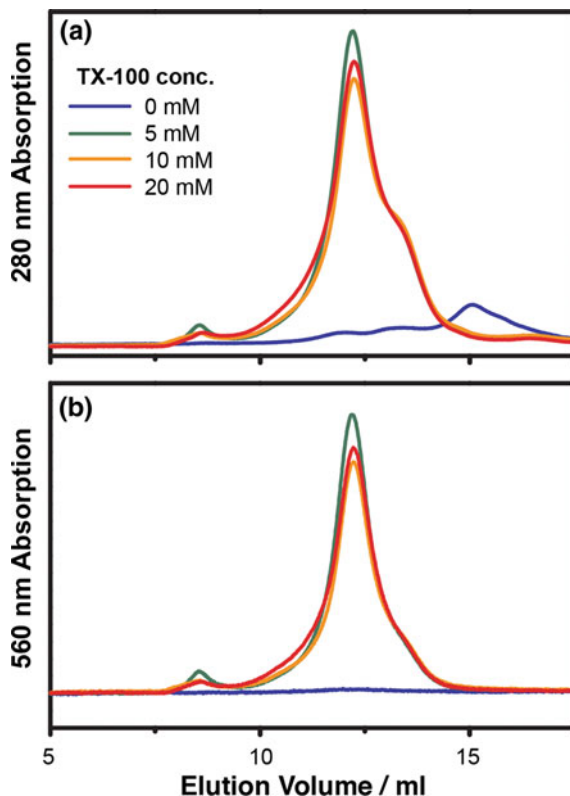
Fig. 5.4 Size exclusion chromatography profiles for comparison of PMND assembled with different incubation period prior to the removal of detergent of 10 min (green), 30 min (red) and 60 min (blue), monitoring at **a** 280 nm and **b** 560 nm absorption. Samples were assembled under the same conditions other than the incubation period before detergent is removed, with 10 mM of Triton X-100, 25 μ M of cE3D1, and 3.84 M NaCl. Reproduced with permission from Ref. [24], from Nature Publishing Group



A small amount of detergent was added to the assembly to perturb the intertrimer interaction and disrupt the PM aggregate in order to assemble isolated trimer bR in individual nanodisc. Figure 5.4 shows the optimization of the incubation period after the assembly and before the detergent was removed. From the comparison it can be seen that the incubation period before the removal of detergent has a small effect on the yield of the PMND assembly and the small aggregate. Shown in Fig. 5.5, the concentration of detergent in the assembly mixture can also have a small influence over the yield of PMND produced. The increased amount of detergent appears to decrease the yield of PMND, however the small aggregate around 13 ml elution volume remained the same absorption intensity. Also shown in Fig. 5.5, successful PMND requires only a small amount of detergent but if in the absence of detergent, shown in blue with Triton X-100 at 0 mM, cE3D1 alone is insufficient to extract bR from PM and thus no PMND can be assembled.

Of the parameters optimized, the salt concentration of the assembly had the greatest impact on the success and the yield of PMND. Shown in Fig. 5.6, the comparison of the size exclusion chromatography of PMND assembled using different final NaCl concentrations. The final NaCl concentration was calculated by the amount of NaCl dissolved in various components used in the PMND assembly.

Fig. 5.5 Size exclusion chromatography profiles for comparison of PMND assembled with different final concentration of TX-100 of 0 mM (blue), 5 mM (green), 10 mM (orange) and 20 mM (red), monitoring at **a** 280 nm and **b** 560 nm absorption. Samples were assembled under the same conditions other than the concentration of Triton X-100, with 30.8 μM of cE3D1, 3.62 M NaCl and incubated for 10 min before detergent is removed. Reproduced with permission from Ref. [24], from Nature Publishing Group



When the concentration of NaCl in the final assembly is decreased, the intensity of the products in size exclusion chromatography profiles are decreased, with the sizes shifted towards smaller nanodiscs and MSP aggregates. The smaller nanodisc peak showed absorption at 560 nm suggesting the fraction contained bR, it is therefore reasonable to assume the smaller nanodisc is in fact PMND with monomeric bR. As the NaCl concentration increases, the intensity of the peak increases significantly and the size of the product slightly increases. The peak of PMND also became more symmetrical as the salt concentration increases providing a higher production yield.

The size exclusion profile of purified PMND assembly is shown in Fig. 5.7, assembled using 10 mM Triton X-100, 25 μM cE3D1, 3.84 M NaCl, and incubated for 10 min before BioBeads were added to the mixture to remove the detergent. The transfer yield from PM to PMND assembly was found to be up to 38%. The high production is ideal to provide sufficient sample for biophysical characterizations. Estimating using the extinction coefficient of PM at 280 and 568 nm, and extinction coefficient of cE3D1 at 280 nm, the ratio of absorption at 560 and 280 nm of the peak of PMND from the SEC profile in Fig. 5.7 contained about 61% of bR embedded nanodisc.

Fig. 5.6 Size exclusion chromatography profiles for comparison of PMND assembled with different final concentration of NaCl of 0.07 M (red), 1.22 M (orange), 2.35 M (green) and 3.84 M (blue), monitoring at **a** 280 nm and **b** 560 nm absorption. Samples were assembled under the same conditions other than the concentration of NaCl, with 10 mM Triton X-100, 25 μ M of cE3D1, and incubated for 10 min before detergent is removed. Reproduced with permission from Ref. [24], from Nature Publishing Group

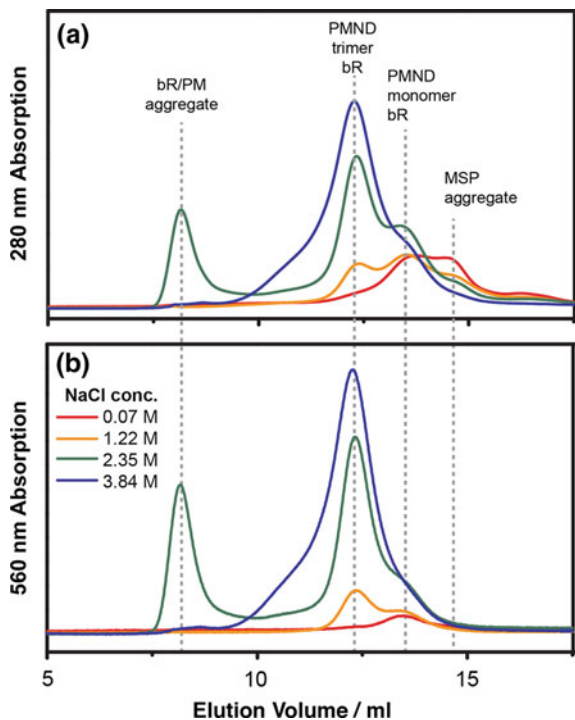
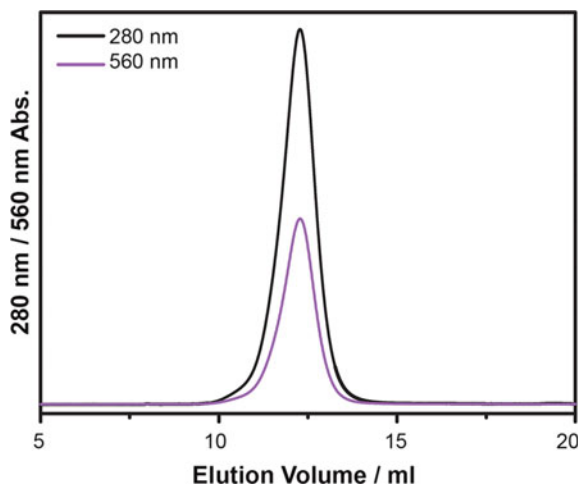


Fig. 5.7 Size exclusion chromatography profile of purified PMND assembled using 10 mM Triton X-100, 25 μ M of cE3D1, and 3.84 M NaCl, incubated for 10 min before detergent is removed. Reproduced with permission from Ref. [24], from Nature Publishing Group



5.3.2 PMND Characterization

The size of PMND is estimated to be 150 ± 25 kDa using size exclusion chromatography calibrations. The sample of PMND was taken to perform anionic exchange chromatography and compared to the monomeric bR embedded nanodisc made of synthetic lipids, discussed in Chap. 3. Using the same conditions as Fig. 3.6, the surface charge of PMND was compared with the surface charge of monomeric bR embedded nanodisc composed of linear MSP1E3D1 and different ratios of DOPG/DOPC content. The anionic exchange chromatography profile shown in Fig. 5.8 revealed that PMND has a negative surface charge slightly more than that of bR embedded in DOPG/DOPC nanodisc, but not as negative as the bR embedded in pure DOPG nanodisc. Considering the major native lipid of PM is about 40% PG, and from Fig. 3.5 it was concluded that bR contributes a slightly negative surface charge, the result in Fig. 5.8 showed agreement to the previous observations.

The protein extracted from PMND using organic solvents was taken to perform MALDI-TOF to verify the content, and the mass spectrum shown in Fig. 5.9 shows two distinct signals belonging to bR and to cE3D1, confirming the size exclusion chromatography profile of nanodisc with bR embedded inside. Figure 5.10 shows the steady state absorption spectra of PMND compared to bR in other environments, such monomeric bR in detergent micelles, in lipid nanodisc composed of DMPG/DMPC 50/50 and trimeric bR in PM. The peak around 660 nm is a known artifact attributed to the UV-Vis light source. From the steady state spectra it can be seen that PMND exhibits a maximum absorption at 563 nm. As discussed in

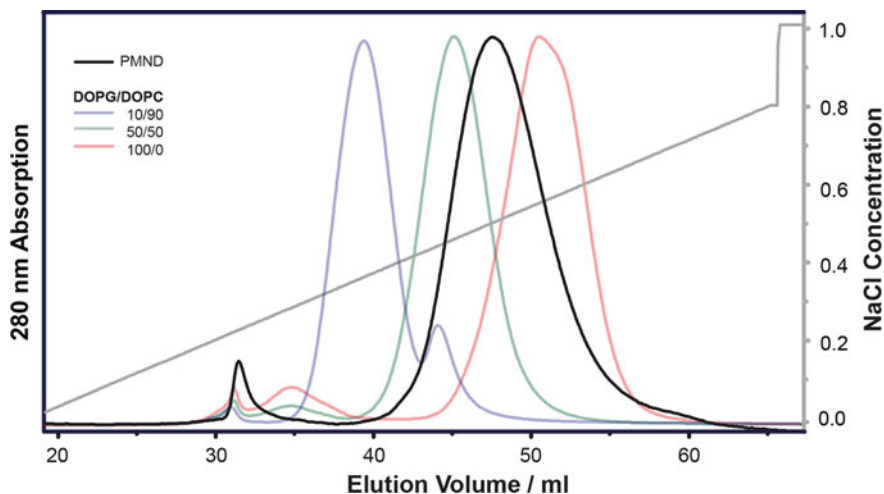


Fig. 5.8 Anionic exchange chromatography of PMND (black) compared with monomeric bR embedded in nanodisc composed of synthetic lipids previously shown in Fig. 3.6, with DOPG/DOPC ratios of 10/90 (blue), 50/50 (green), 100/0 (red)

Fig. 5.9 MALDI-TOF mass spectrum of PMND protein extracts

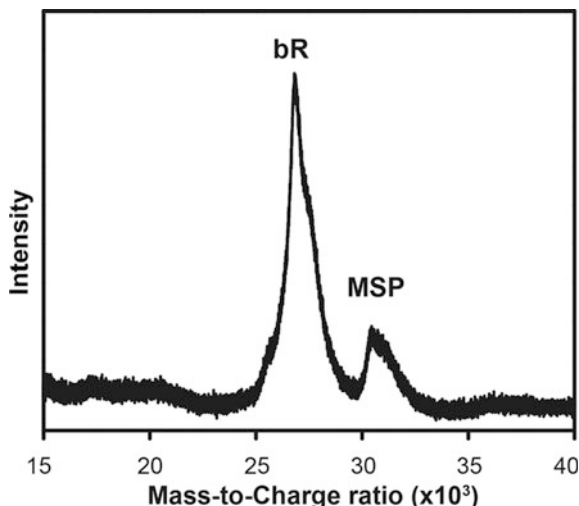
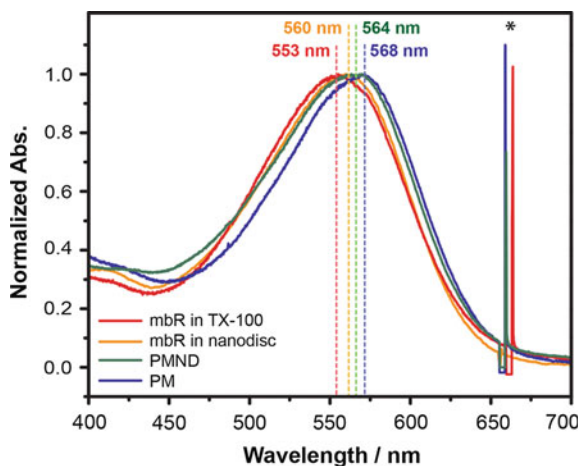


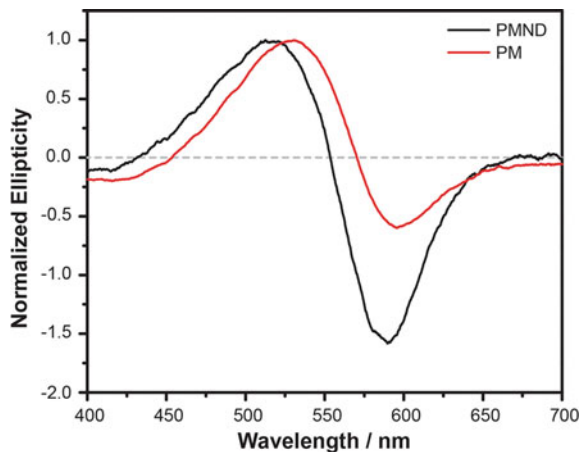
Fig. 5.10 Steady state spectra of monomeric bR in detergent micelle (red), monomeric bR in nanodisc composed of DMPG/DMPC 50/50 (orange), PMND (green) and trimeric bR in PM (blue). The maximum absorption wavelengths of each sample are listed with the respective color. The (*) indicates artifact from light source of experimental set up



Chap. 3, monomeric bR embedded in nanodisc with different compositions of synthetic lipids did not show significant differences in absorption peaks, with the peak located around 560 nm. Comparing PMND to monomeric bR embedded in nanodisc of synthetic lipid, the absorption of PMND at 563 nm is closer to the 568 nm absorption maximum of bR in native purple membrane. This suggests the retinal pocket of bR in PMND has a greater similarity to those found in PM than monomeric bR in nanodisc composed of synthetic lipids.

Visible range circular dichroism was used to determine the oligomeric state of bR in PMND. Shown in Fig. 5.11, The CD spectrum of PMND showed clear biphasic features, suggesting the bR is at least mostly in trimeric conformation. The homogeneity of the trimeric conformation cannot be verified using circular

Fig. 5.11 Normalized circular dichroism spectra recorded at the visible wavelength range of PMND (black) and PM (red) performed at 20 °C



dichroism due to the drastic difference in intensities of monomeric and trimeric features. Comparing the CD spectrum of PMND to PM, although the biphasic features are clear, the CD spectrum of PMND experiences a significant shift in the zero interception wavelength. The direction of the shift agrees with the shifts observed in steady state absorption spectra, however shown in Fig. 5.10, the differences in maxima of PMND and PM are only 5 nm. In CD spectra, the difference in the zero intercept wavelengths is 17 nm, which is much greater than ones observed in the steady state absorption experiment. Moreover, the spectra were normalized based on the positive, shorter wavelength peak. By normalizing the spectra it can be seen that the ratio between the positive and the negative peaks are different with PM and PMND, despite both displaying biphasic features. Referring back to Sect. 2.2, the theoretical calculation suggested that biphasic features arise from coupling and intratrimer interaction, the ratio between the positive and the negative peaks could be influenced by the intertrimer interaction [16]. The difference in the CD spectra between PM and PMND could be attributed to the difference in intertrimeric interactions, as PMND would likely be present as isolated trimers and thus lack the trimer-trimer interaction.

As mentioned previously, PMND assembled in high NaCl concentration yielded primarily trimeric bR embedded on the nanodisc, however some nanodisc containing monomeric species still existed in the sample. By using visible wavelength circular dichroism spectroscopy, it was shown that size exclusion is capable of separating the nanodisc with trimeric bR and monomeric bR. Figure 5.12a showed the size exclusion profile of PMND and the positions of the fractions collected during the chromatography experiment. Each individual fraction was condensed separately and investigated using visible wavelength circular dichroism. Each circular dichroism spectrum shown in Fig. 5.12b was normalized with the absorbance of steady state absorption contour maximum around the bR characteristic absorption wavelength. In other words, the circular dichroism spectra were normalized by the concentration of bR. Figure 5.12b shows that trimeric bR characteristic was

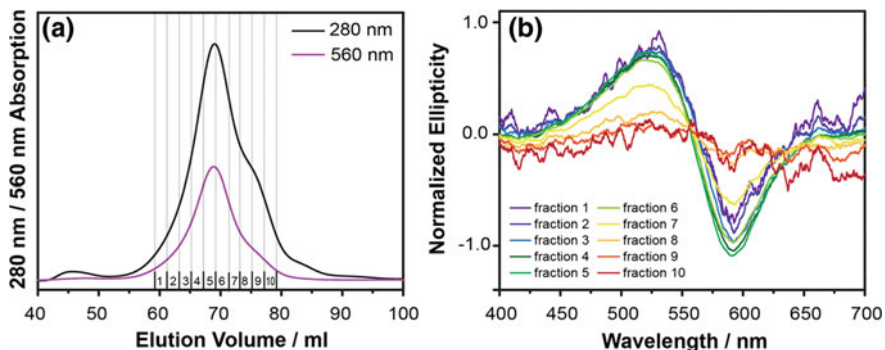


Fig. 5.12 **a** Size exclusion chromatography profile of PMND using HiLoad Superdex 200, monitoring the elution at both 280 nm and 560 nm absorption. The positions of individual fractions were indicated in numeric order. **b** Visible wavelength circular dichroism spectra of individual fractions indicated in **a**. The spectra were normalized by the maximum absorbance in steady state absorption experiment of respective fraction. Reproduced with permission from Ref. [24], from Nature Publishing Group

clearly observed in the earlier fractions and was consistent in normalized intensity. However, starting from fraction 7, the signal intensity of the trimeric bR characteristic began to rapidly decrease, where eventually the biphasic feature is no longer clear. Since in the later fractions, particularly 8 through 10, the size exclusion profile indicated clear absorption of 560 nm suggesting the presence of bR in the sample, one can conclude that the bR existed in monomeric form. The result showed that size exclusion chromatography is capable of separating PMND containing different oligomeric states of bR. Therefore for the following section, only trimeric bR in PMND would be collected to perform characterization.

Figure 5.13 shows Zernike phase TEM [17, 18] images of PMND. The images of unstained sample allowed improvement of resolution and preservation of the integrity of the sample. The technique revealed high-resolution images of PMND, particularly distinguishing between the MSP and the lipid components. The images clearly show disc shaped units with cE3D1 wrapping around the lipid core in a circular manner, providing evidence of a successful PMND assembly.

While spectroscopic and imaging methods revealed the successful extraction and incorporation of bR from PM into nanodisc, the transfer of native lipid from PM to PMND is of particular interest. Discussed in detail and demonstrated in Chap. 3, the lipid composition of nanodisc has a significant influence over the function of bR. The native PM lipid has been previously analyzed using solution state ^{31}P NMR spectroscopy [19, 20], as most lipid molecules are phospholipids, as well as using LC-MS for the none phospholipid S-TGD-1. The lipid molecules of PM and PMND were extracted using organic solvents. For ^{31}P NMR, The extracted lipid was dried and redissolved in deuterated chloroform and methanol reagents. The ^{31}P NMR spectra of lipid extracted from PM and PMND are shown in Fig. 5.14. The chemical shift assignment of PM was according to the values reported by Corcelli et al. [20] and is shown in Table 5.2. The ^{31}P spectrum of PM shown in

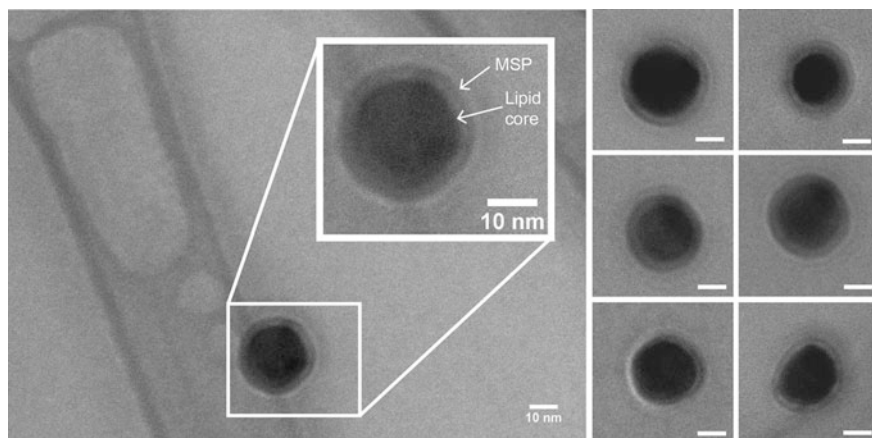


Fig. 5.13 Zernike phase TEM images of PMND. All the scale bars are 10 nm. Reproduced with permission from Ref. [24], from Nature Publishing Group

Fig. 5.14a shows agreement to the reported values, which is to be expected despite a small difference in lipid extraction methods. The ^{31}P spectrum of PMND in Fig. 5.14b contains the peaks with chemical shifts consistent with the lipids found in PM. This suggests that during the process of PMND assembly the native lipids are extracted and most of the phospholipids are present. However, as shown by the difference in relative peak intensities, the relative amount of individual lipid was not retained. Not all of major lipids found in PM are phospholipids, therefore to further analyze the lipid content, LC-ESI-MS was performed with the lipid extract redissolved in methanol, shown in Fig. 5.14c and d. Figure 5.14c shows the LC-MS spectrum of lipid extracted from PM, which showed good agreement to the molecular weight reported by Corcelli et al. [20]. Two phospholipids, BPG and GlyC were not observed in the LC-MS spectra but were seen in ^{31}P NMR. This could be due to the sensitivity and the ionization efficiency of the lipid types. The LC-ESI-MS spectrum of PMND lipid extract in Fig. 5.14d showed that two lipids previously found in PM, PGS and S-TGD-1, are absent. The extra signals recorded for PMND lipid extracts likely arose from protein fragments, as PMND contained additional protein in comparison to PM. Since S-TGD-1 cannot be observed in ^{31}P NMR experiment and PGS has a very similar ^{31}P chemical shift to BPG, the results from two methods showed agreement to each other. It was previously reported that PGP-Me is crucial and essential in maintaining the photocycle activity of bR [7, 21]. The result of lipid analysis showed that PGP-Me was successfully transferred from PM into PMND, thus the function and photocycle activity are expected to be preserved in PMND.

Transient absorption spectroscopy was performed to investigate the preservation of bR function, since the proton pumping process can be monitored through the progression of intermediate states and photocycle. Figure 5.15 shows the time resolved difference spectra of PMND monitoring at different wavelengths to

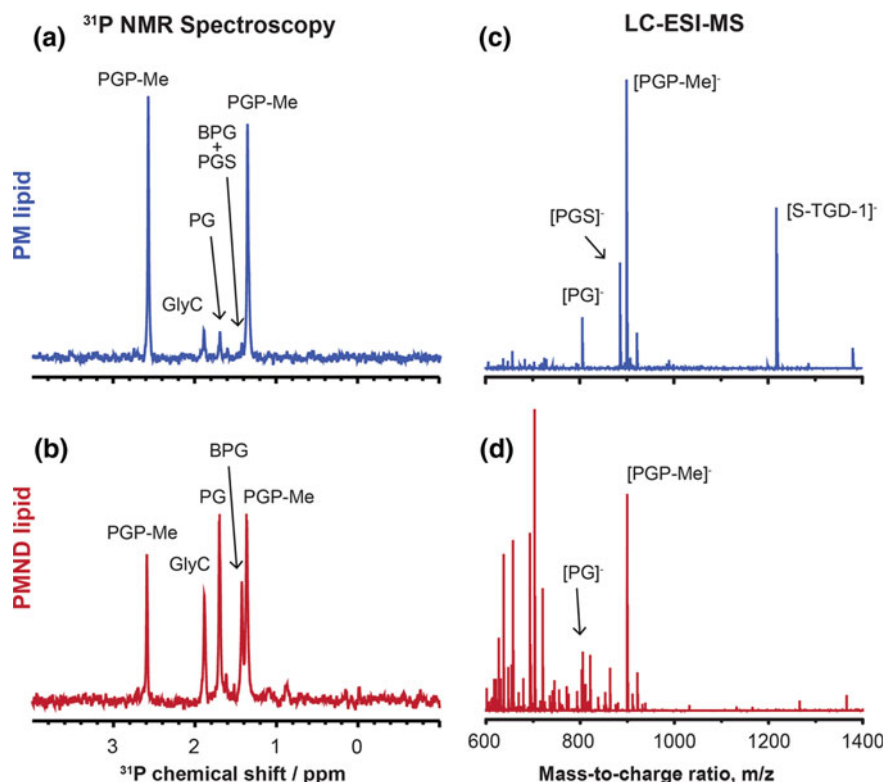


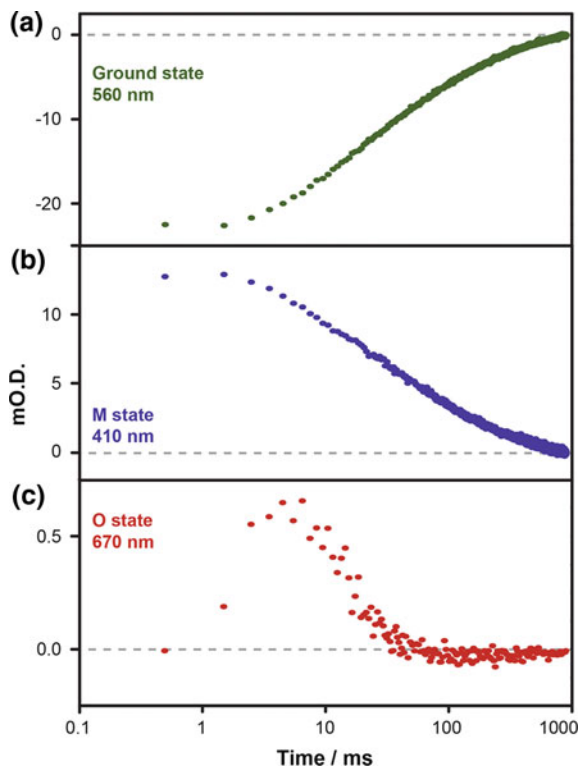
Fig. 5.14 **a, b** ^{31}P NMR spectra and **c, d** LC-ESI-MS spectra of lipid extracted from **(a, c)** PM and **(b, d)** PMND. The assignments of each spectrum are based on the ^{31}P NMR chemical shift values and molecular weights reported in Ref. [20]. Reproduced with permission from Ref. [24], from Nature Publishing Group

Table 5.2 ^{31}P chemical shift of the individual PM phospholipids reported by Corcelli et al. [20]

Lipid	$\delta(^{31}\text{P})/\text{ppm}$
GlyC	1.964
PGS	1.374
PGP-Me	1.357 and 2.594
PG	1.725
BPG	1.401

observe the formation of key intermediate states. The M intermediate state corresponds to the deprotonation of the retinal Schiff base, and hence represents the translocation of the proton towards the extracellular side, while the O intermediate state is related to the relaxation of the retinal molecule and indicates the traditional PM photocycle pathway. The time-resolved difference spectra show a clear

Fig. 5.15 Temporal profiles of **a** bR parent state recovery at 560 nm, **b** M state intermediate at 410 nm and **c** O state intermediate at 670 nm. Reproduced with permission from Ref. [24], from Nature Publishing Group



formation of both the M and the O intermediate state, suggesting the bR function was preserved in PMND and the photocycle undergoes the pathway similar to PM.

While we demonstrated membrane scaffold protein has the ability to extract membrane protein and the surrounding native lipid from the biological membrane, it has been reported that SMA co-polymer, introduced in Sect. 1.2.5, can achieve similar results. However, one particular limitation of using SMA co-polymer and SMALPs is that the solubility of SMA co-polymer strongly depends on pH. As pH falls below 6.5, the carboxyl group of malic acid will be fully protonated and the polymer would begin to aggregate, eventually precipitating out of the solution. This property can limit the conditions in which the incorporated membrane protein can be studied. Figure 5.16 shows size exclusion chromatography of PMND assembled at different pH conditions. While pH appears to influence both the size homogeneity of PMND as well as the assembly efficiency, with acidic conditions better than the alkali conditions, the size exclusion profiles suggest that PMND can assemble even in low pH conditions. This implies that MSP solubilized biological membrane has a greater flexibility over not only the experimental conditions, but also solubilizing nanodisc assembly conditions. The flexibility over pH is important in the study of membrane protein, as the function of membrane protein can change with different pH [22, 23].

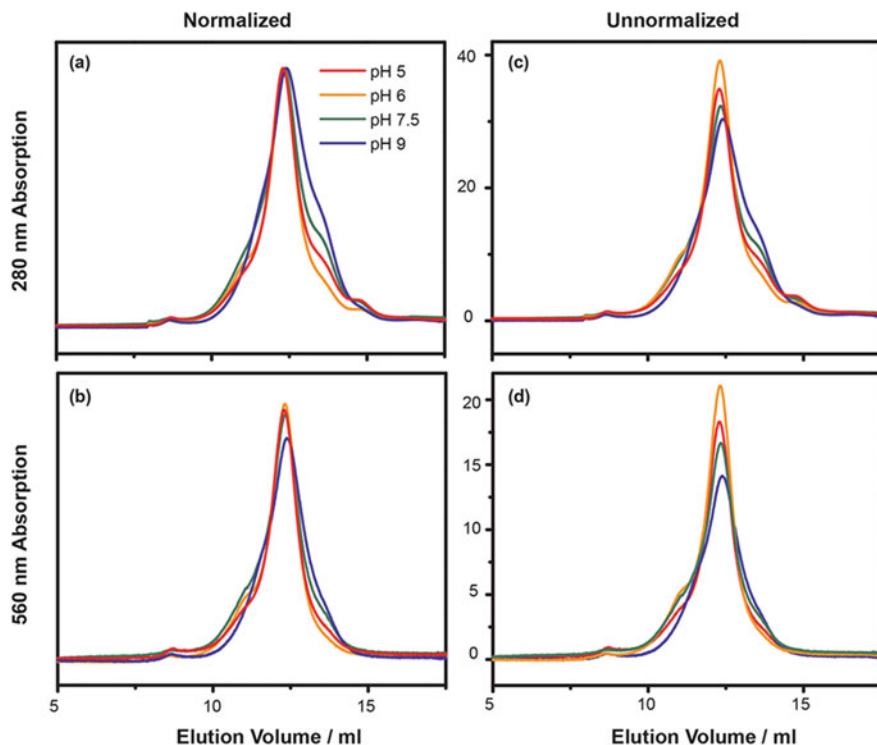


Fig. 5.16 **a, b** Normalized and **c, d** unnormalized size exclusion chromatography profiles of PMND assembled at pH 5 (red), pH 6 (orange), pH 7.5 (green) and pH 9 (blue), monitoring at (**a, c**) 280 nm and (**b, d**) 560 nm. The normalized spectra were normalized based on the corresponding 280 nm absorbance. Reproduced with permission from Ref. [24], from Nature Publishing Group

5.4 Conclusion

For the study of membrane protein, it is often ideal for the target membrane protein to be in its native environment. However, with the nature of the native biological membrane it is usually difficult to achieve, whether the difficulties lie with sample preparation or on experimental limitations. Nanodisc can provide a small lipid bilayer that is homogenous in size and is stable in aqueous solution, but the use of synthetic lipids disrupts and deviates from the native environment. We demonstrated a highly efficient method of extracting membrane protein and its native lipids and incorporating them into nanodisc in one step, directly from the natural biological environment. By using a modified MSP, we were able to extract and incorporate bacteriorhodopsin with the native PM lipids into size homogenous nanodisc with a sufficiently high yield of 35%, directly from the PM purified from *Halobacterium salinarum*. The condition of the native purple membrane nanodisc (PMND) was optimized carefully and monitored using size exclusion

chromatography. Modified circular MSP with the N and C termini chemically linked together (cMSP) was shown to produce PMND with higher homogeneity, compared to the PMND assembled using traditional linear MSP. Detergent concentration, assembly duration and PM to cMSP ratio was optimized to provide the highest yield. NaCl concentration of PMND assembly was found to be the dominant factor in the effectiveness of PMND formation, governing both the success and the yield of PMND production.

PMND was characterized using various spectroscopic methods. The formation of PMND was confirmed with MALDI-TOF mass spectroscopy, where two distinct signals were observed and were identified to be bR and cMSP. The retinal state of bR was characterized using steady state absorption spectroscopy. PMND showed only a minor blue shift from the absorption maximum of PM, suggesting the retinal states in PMND have a greater similarity to PM, in comparison to monomeric bR embedded in nanodisc composed of synthetic lipid. The oligomeric state of PMND was verified using visible wavelength circular dichroism, where a clear biphasic feature was observed indicating the preservation of trimeric conformation of bR. When compared to the spectrum recorded for PM, a difference in the ratio of the oppositely signed peak was observed. The difference can be attributed to difference in intertrimer interactions, in particular the formation of PMND suggests isolated trimers with a lack of interaction to the neighbouring trimer unit. Zernike Phase TEM of unstained sample provided a high resolution image showing the circular feature of PMND, where the MSP was shown to wrap around a disc-shape core, verifying the formation of PMND. The lipid molecules of PM and PMND were extracted and identified using ^{31}P NMR spectroscopy and LC-ESI-MS. ^{31}P NMR spectra and LC-ESI-MS showed most native phospholipids, in particular PGP-Me, were successfully extracted and incorporated in PMND. Finally, single wavelength transient absorption spectroscopy was performed to demonstrate the function of bR in PMND was preserved. The intermediate state M was clearly observed in the time resolved difference spectrum, as was intermediate state O, suggesting the photocycle of PMND undergoes the conventional pathway similar to PM.

With the main limitations in membrane protein research being the difficult sample preparation, this method of extraction of both membrane protein and native lipids from the biological membrane to form nanodisc for biophysical characterization has the ability to improve the quality of samples. While SMA copolymer has been demonstrated to have a similar ability of extracting membrane protein from membrane, the native nanodisc consisted of MSP showed a greater flexibility over the pH of both assembly condition and characterization environment.

Acknowledgements The Zernike phase TEM image was taken by Pai-Chia Kuo from the Institute of Physics of Academia Sinica, Taipei, Taiwan. Dr. Shing-Jong Huang from the Instrumentation Center of National Taiwan University, Taipei, Taiwan, performed the ^{31}P NMR experiment. LC-ESI-MS experiment was operated by Dr. Chien-Hung Chen of Core Facilities in Genomic Research Centre, Academia Sinica, Taipei, Taiwan. Transient absorption spectroscopy was performed at National Tsing Hua University, Hsinchu, Taiwan, with the help of Tsung-Yen Lee.

References

1. Cherry RJ, Müller U, Henderson R, Heyn MP (1978) Temperature-dependent aggregation of bacteriorhodopsin in dipalmitoyl- and dimyristoylphosphatidylcholine vesicles. *J Mol Biol* 121:283–298. [https://doi.org/10.1016/S0022-2836\(78\)80010-2](https://doi.org/10.1016/S0022-2836(78)80010-2)
2. Heyn MP, Cherry RJ, Dencher NA (1981) Lipid-protein interactions in bacteriorhodopsin-dimyristoylphosphatidylcholine vesicles. *Biochemistry (Mosc)* 20:840–849. <https://doi.org/10.1021/bi00507a029>
3. Gulik-Krzywicki T, Seigneuret M, Rigaud JL (1987) Monomer-oligomer equilibrium of bacteriorhodopsin in reconstituted proteoliposomes: a freeze-fracture electron microscope study. *J Biol Chem* 262:15580–15588
4. Grzesiek S, Dencher NA (1988) Monomeric and aggregated bacteriorhodopsin: single-turnover proton transport stoichiometry and photochemistry. *Proc Natl Acad Sci U S A* 85:9509–9513
5. Bayburt TH, Grinkova YV, Sligar SG (2006) Assembly of single bacteriorhodopsin trimers in bilayer nanodiscs. *Arch Biochem Biophys* 450:215–222. <https://doi.org/10.1016/j.abb.2006.03.013>
6. Dong YQ, Ramos RG, Li D, Barrett SE (2008) Controlling coherence using the internal structure of hard pi pulses. *Phys Rev Lett* 100:4. <https://doi.org/10.1103/PhysRevLett.100.247601>
7. Joshi MK, Dracheva S, Mukhopadhyay AK et al (1998) Importance of specific native lipids in controlling the photocycle of bacteriorhodopsin. *Biochemistry (Mosc)* 37:14463–14470. <https://doi.org/10.1021/bi980965j>
8. Sternberg B, L'Hostis C, Whiteway CA, Watts A (1992) The essential role of specific *Halobacterium halobium* polar lipids in 2D-array formation of bacteriorhodopsin. *Biochim Biophys Acta BBA—Biomembr* 1108:21–30. [https://doi.org/10.1016/0005-2736\(92\)90110-8](https://doi.org/10.1016/0005-2736(92)90110-8)
9. Orwick-Rydmark M, Lovett JE, Graziadei A et al (2012) Detergent-free incorporation of a seven-transmembrane receptor protein into nanosized bilayer lipid particles for functional and biophysical studies. *Nano Lett* 12:4687–4692. <https://doi.org/10.1021/nl3020395>
10. Nasr ML, Baptista D, Strauss M et al (2017) Covalently circularized nanodiscs for studying membrane proteins and viral entry. *Nat Methods* 14:49–52. <https://doi.org/10.1038/nmeth.4079>
11. Yusuf Y, Massiot J, Chang Y-T et al (2018) Optimization of the production of covalently circularized nanodiscs and their characterization in physiological conditions. *Langmuir* 34:3525–3532. <https://doi.org/10.1021/acs.langmuir.8b00025>
12. Baudry J, Tajkhorshid E, Molnar F et al (2001) Molecular dynamics study of bacteriorhodopsin and the purple membrane. *J Phys Chem B* 105:905–918. <https://doi.org/10.1021/jp000898e>
13. Hagn F, Etzkorn M, Raschle T, Wagner G (2013) Optimized phospholipid bilayer nanodiscs facilitate high-resolution structure determination of membrane proteins. *J Am Chem Soc* 135:1919–1925. <https://doi.org/10.1021/ja310901f>
14. Denisov IG, Grinkova YV, Lazarides AA, Sligar SG (2004) Directed self-assembly of monodisperse phospholipid bilayer nanodiscs with controlled size. *J Am Chem Soc* 126:3477–3487. <https://doi.org/10.1021/ja0393574>
15. Bayburt TH, Sligar SG (2010) Membrane protein assembly into Nanodiscs. *FEBS Lett* 584:1721–1727. <https://doi.org/10.1016/j.febslet.2009.10.024>
16. Pescitelli G, Woody RW (2012) The exciton origin of the visible circular dichroism spectrum of bacteriorhodopsin. *J Phys Chem B* 116:6751–6763. <https://doi.org/10.1021/jp212166k>
17. Dai W, Fu C, Raytcheva D et al (2013) Visualizing virus assembly intermediates inside marine cyanobacteria. *Nature* 502:707–710. <https://doi.org/10.1038/nature12604>
18. Kuo P-C, Chen I-H, Chen C-T et al (2013) On-chip thin film zernike phase plate for in-focus transmission electron microscopy imaging of organic materials. *ACS Nano* 7:465–470. <https://doi.org/10.1021/nn304511p>

19. Renner C (2005) Lipid composition of integral purple membrane by ¹H and ³¹P NMR. *J Lipid Res* 46:1755–1764. <https://doi.org/10.1194/jlr.M500138-JLR200>
20. Corcelli A, Lattanzio VMT, Mascolo G et al (2002) Lipid-protein stoichiometries in a crystalline biological membrane: NMR quantitative analysis of the lipid extract of the purple membrane. *J Lipid Res* 43:132–140
21. Cui J, Kawatake S, Umegawa Y et al (2015) Stereoselective synthesis of the head group of archaeal phospholipid PGP-Me to investigate bacteriorhodopsin–lipid interactions. *Org Biomol Chem* 13:10279–10284. <https://doi.org/10.1039/C5OB01252J>
22. Chizhov I, Schmies G, Seidel R et al (1998) The photophobic receptor from *Natronobacterium pharaonis*: temperature and pH dependencies of the photocycle of sensory rhodopsin II. *Biophys J* 75:999–1009
23. Chu L-K, Yen C-W, El-Sayed MA (2010) Bacteriorhodopsin-based photo-electrochemical cell. *Biosens Bioelectron* 26:620–626. <https://doi.org/10.1016/j.bios.2010.07.013>
24. Yeh V, Lee T-Y, Chen C-W et al (2018) Highly efficient transfer of 7TM membrane protein from native membrane to covalently circularized nanodisc. *Scientific Reports* 8(1)

Chapter 6

Conclusions and Outlook



The nature of membrane protein, such as solubility and the dependency on the membrane environment, has given rise to formidable challenges to study and investigate. Membrane mimics have been extensively employed to provide a platform to allow biophysical characterization. Lipid nanodisc, a small lipid bilayer wrapped by two copies of α helical amphipathic proteins, has been designed to incorporate membrane protein in a way that is suitable for spectroscopic studies. While many membrane proteins have been studied with the use of lipid nanodisc, both functional and structural, the properties of the nanodisc and their effects on the target membrane protein have not been thoroughly discussed. By using bacteriorhodopsin as the target membrane protein, this study investigates the feasibility of using different lipid composition and different sizes of nanodiscs to manually tune the function of membrane protein embedded in the nanodiscs. Furthermore, we developed a novel method to extract membrane protein and the native lipid molecules directly from the biological membrane, and incorporate them into nanodisc.

In Chap. 3, we successfully incorporated monomeric bacteriorhodopsin into nanodisc consisting of lipids with different charges of hydrophilic head and different structures of hydrophobic tails. The bR embedded nanodisc with different lipid composition was characterized using ionic exchange chromatography and showed the surface charge of the nanodisc becomes more negative with increasing PG content. Steady state spectroscopy revealed that bR embedded in nanodisc experiences a minor blue shift in comparison to the native purple membrane, and the shift is almost independent of the lipid composition. The photocycle kinetics of bR embedded in nanodisc was characterized using transient absorption spectroscopy, and showed that the lipid composition of nanodisc has a significant influence over the function of bR. The recovery rate of bR parent state drastically decreases as the negatively charged lipid content decreases, while the population of intermediate O decreases. This suggests the duration of the photocycle changes significantly with the change in lipid composition, which also alters the photocycle pathway. This effect is dominated by the charges of the hydrophilic head, with a

small contribution from the different hydrophobic tails. Further analysis with transient photocurrent measurement showed that while negatively charged lipid heads trap the proton released by the protein, the neutral and positively charged hydrophilic head assists and repulses the proton into the bulk solution. The study suggests that the lipid plays an important role in the function of some membrane protein, and that the lipid composition of nanodisc can be tuned to manually alter the function of the membrane protein.

The size of nanodisc and its effect on the membrane protein was investigated in Chap. 4. By using *E. coli* expressed bacteriorhodopsin we could eliminate uncertainty in the contribution of native lipids, as it is unknown whether different amount of native lipids would be transferred to different sizes of nanodisc. The bacteriorhodopsin HmbRID94N was successfully expressed using *E. coli* and purified with nonionic detergent Triton X-100, and demonstrated to be monomeric using visible wavelength circular dichroism. Isotopically labeled HmbRID94N was exchanged into solution state NMR suitable detergent, C7-DHPC, and preliminary results suggest promising use of solution state NMR to probe structural details of HmbRID94N. HmbRID94N in Triton X-100 micelle was then compared to HmbRID94N embedded in DMPG nanodisc and showed that the photocycle kinetics was significantly altered by the different environment structure. The lifetime of HmbRID94N photocycle and quantum yield is shown to decrease drastically in the lipid bilayer of nanodisc compared to detergent micelle. However, HmbRID94N incorporated into different sizes of nanodisc was demonstrated to have similar photocycle lifetimes, suggesting that function of HmbRID94N is not influenced by the size of the nanodisc. While the photocycle lifetimes of HmbRID94N in different sizes of nanodisc were the same, the lifetime of intermediate M state was shown to be slightly longer in smaller nanodisc. However, the difference observed is not significant. The lack of difference in photocycle, which can contribute to the long photocycle duration, arose from the mutation of key amino acids involved in the proton translocation, as preliminary results from the study of nanodisc size effect using HsbR, with native lipids removed, showed different photocycle duration between the different sizes of nanodisc. The difference in photocycle kinetics observed for bR embedded in different sizes of nanodisc is not as significant when compared to the effect of lipid composition, suggesting the lipid composition is the dominant factor.

While Chaps. 3 and 4 discussed the effect of artificial properties of nanodisc on the function of membrane protein, Chap. 5 discusses the possibility of preserving the biological state of membrane protein in a way that allows biophysical characterizations. Since the lipid composition of nanodisc is demonstrated to have a significant effect on the photocycle kinetics of bacteriorhodopsin, we developed a method to extract bR and its native lipids directly from the purple membrane and incorporate them into nanodisc in one reaction mixture. Using modified MSP where the N and C termini are chemically linked by sortase catalytic reaction, the process of assembling native purple membrane nanodisc (PMND) was systematically optimized. In particular, NaCl concentration was demonstrated to be a major factor in both the success and the yield of PMND production. Under optimized conditions

the yield of PMND is up 38% from the origin PM, providing high production ideal for biophysical characterization. PMND was demonstrated to preserve the trimeric conformation of bR, while a Zernike phase TEM image of unstained sample shows the circular disk appearance of PMND. The lipid composition was analyzed with ^{31}P NMR and LC-ESI-MS, where most types of phospholipid, in particular the essential lipid PGP-Me, which was reported to be crucial in maintaining of bR, were present. bR in PMND was revealed to maintain the photocycle activity and underwent conventional PM photocycle pathway, suggesting that the function of bR was preserved during the extraction and incorporation into PMND. The novel technique provides significant advantage in the study of membrane protein, where membrane protein can be well characterized while preserved in the biological conformation surrounded by native lipid molecules. The membrane protein of interest can be overexpressed on the organism with the biological membrane and extracted using small amount of detergent and modified MSP, allowing the native conformation and structure to be studied.

The use of nanodisc as a platform to study membrane protein and their functions has become increasingly popular, particularly using solution state NMR and other spectroscopic methods. This study aimed to investigate the properties of nanodisc and their effects on the membrane protein to gain insights into the biological status of nanodisc. It serves as an example that the lipid composition of nanodisc can be employed to tune the function of embedded membrane protein for the particular experimental designs, while the sizes of nanodisc have a less significant influence on the function of membrane in comparison to the lipid composition. On the other hand, size and lipid composition of nanodisc should be carefully considered, particularly in functional studies, when biological relevancy is being emphasized. The ability to assemble nanodisc using native lipid, preserving the protein function and conformation on the biological membrane provides possible solutions to the use of synthetic lipid.

Appendix

I—Preliminary Results of HsbR in DMPC Nanodisc of Different Sizes

See Fig. A.1.

Fig A.1 Preliminary results of HsbR with native lipid previously removed, embedded in nanodisc composed of DMPC at pH 7. The time resolved difference spectra of HsbR embedded in nanodisc consisted of either (black) cE3D1 or (red) c Δ H5, observing the recovery of parent state at 568 nm (upper) and M intermediate at 410 nm (lower)

